AN EXAMINATION OF HYDROGRAPHY AND SEA LEVEL VARIABILITY IN THE GULF OF ALASKA

By

James Bruce Kelly

RECOMMENDED:

Dr. Zygmunt Kowalik

Dr. Harper Simmons

Dr. Thomas Weingartner
Advisory Committee Chair

Dr. Katrin Iken
Chair, Graduate Program in Marine Sciences and Limnology

APPROVED:

Dr. Joan Braddock
Interim Dean, School of Fisheries and Ocean Sciences

Dr. John Eichelberger
Dean of the Graduate School

28 April 2015
Date

AN EXAMINATION OF HYDROGRAPHY AND SEA LEVEL VARIABILITY IN THE GULF OF ALASKA

A

THESIS

Presented to the Faculty

of the University of Alaska Fairbanks

in Partial Fulfillment of the Requirements

for the Degree of

MASTER OF SCIENCE

By

James Bruce Kelly, B.S.

Fairbanks, Alaska

May 2015

Abstract

This thesis summarizes a detailed analysis of Seward sea level (SSL) in the Gulf of Alaska (GOA) and hydrography at oceanographic station GAK1 along the oceanographic monitoring line outside of Resurrection Bay, Alaska. SSL variability was examined with respect to forcing by tides, sea level pressure (SLP), wind, the steric contribution due to water column variations in temperature and salinity, and several climatic indices. In addition, multi-decadal trends in sea level and hydrography were also examined. The period of analysis spans 1970 -2010. Tidal motion (periods $\leq$ 1day), account for ~97% of the total sea level (SL) variance while SLP variations, induced by the inverted barometer effect, account for ~2% of the total variance. After removing these influences, along-shore wind stress and sea level are highly coherent for the 2 - 60 day subtidal period range and account for ~40 – 50% of the SSL variance over these timescales. The steric contribution, based on the geopotential height referenced to 200 m (GH200), is also coherent with SSL, but it only accounts for ~10% of the SSL variance at these timescales. The along-shore wind stress-SSL coherence varies seasonally and is greatest in winter when winds are strongest and smaller in summer when wind variability is reduced. The annual cycle in SSL is coherent and in-phase with GH200. The latter is primarily controlled by the annual cycle in GOA coastal freshwater discharge and its effect on coastal salinities. SSL variations are also significantly correlated with the Pacific Decadal Oscillation (PDO) and the Southern Oscillation Index (SOI). Over the 40-year record examined here SSL shows a decreasing trend due to continental rebound. There are also statistically significant linear long-term trends in temperature and salinity as measured at GAK1. These trends indicate that the upper 100 m is warming at ~0.20 ^{o}C decade^{-1} and at 0.15 ^{o}C decade^{-1} between 100 - 200 m. Surface salinities are decreasing at 0.15 decade^{-1}, while salinities between 100 and 200 m are increasing by 0.025 decade^{-1}. The surface salinity trends are consistent with an increase in coastal freshwater discharge due to increased glacial ablation and increased precipitation. In aggregate, these trends indicate that the GOA shelf has become more stratified over the past 40 years.

Table of Contents

Page

List of Figures

List of Tables

Acknowledgements

The completion of a master degree requires great effort on the part of the producer. The thesis and other requirements would be orders of magnitude more difficult without the help from others. Others provide funding, advisement, discussions, and personal support. At the university, my advisor Dr. Thomas Weingartner gets the biggest thanks for his advisement and continuous financial support, this support extended throughout my time as a graduate research assistant. In life, my wife Jennifer Kelly gets the biggest thanks for her everyday support. She paid the majority of everyday bills while I worked 20 hrs per week for the majority of my time at the university. Thanks to Seth Danielson for teaching me how to program in Matlab and for help with analysis. Thanks to Hank Statscewich for trusting me and giving me the opportunity to have responsibility on projects that were many miles from home. My committee members Harper Simmons and Zygmunt Kowalik strived to ensure my thesis was quality. The comprehensive exam was one of the most challenging steps during this education process. I failed at my first attempt of this exam; however, I came away with a much greater understanding of the earth system by doing so. These faculty need recognition for spending their time to prepare me for its successful completion: Kenny Coyle, Jennifer Reynolds, Mark Johnson, Thomas Weingartner, Russell Hopcroft and Ana Aguilar-Islas. Thanks to my foreign slaves Dimitri Braznikov and Yin-Chi Fang who provided muscle when I needed help with personal projects at home, and for providing some of the most chaotic entertainment that I have ever experienced. Thanks to my babies Bode (5) and Carlie (3) who provided many joyful distractions while I worked from home.

1 Introduction

Sea level data are rich in hidden signals. Understanding those signals can improve understanding the relationship between ocean-atmosphere coupling, which varies spatially and temporally. These signals arise due to a variety of effects, which on time scales ranging from the hourly to the decadal include tidal, atmospheric pressure fluctuations, winds, and the seasonal cycles of heating, cooling, precipitation and evaporation. There is, in addition, atmospheric-oceanic coupling in regions remote from the location of interest that can affect sea-level variations and hydrography. At longer time scales sea level may fluctuate due to tectonic processes.

The nature and causes of sea level fluctuations have long been of interest to society, particularly with respect to safe navigation and engineering concerns. Climate change and the threat to coastal regions due to an increase in sea level have further spurred research into sea-level variability. In order to understand long term changes in sea level and to predict future changes in sea level, we must understand the natural fluctuations, both their magnitude and their causes. In addition, the occurrence of rapid climate change demands a basic understanding of the variability of these physical parameters, which will be important for understanding their future changes. There has been considerable research done on understanding sea level variability at mid- and low-latitudes; however, less attention has been paid at higher latitudes, including the Gulf of Alaska (GOA; Figure 1), which is the focus of this study.

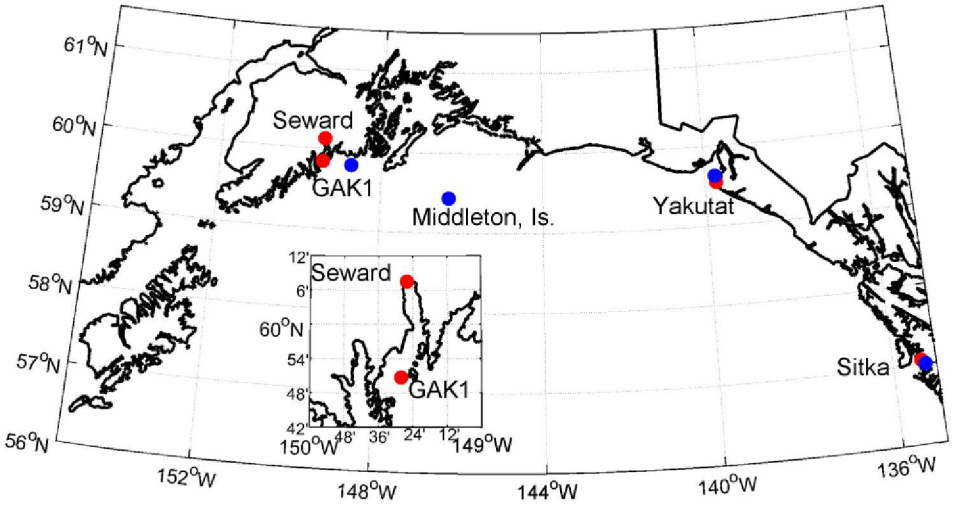

Figure 1. The study region of Gulf of Alaska. Red dots indicate locations of origin sea level or hydrography data, while blue dots indicate locations of wind data.

Spatial atmospheric pressure differences create winds that alter the state of the ocean, which includes the generation of ocean currents and changes in sea level and hydrographic properties, such as temperature, salinity, and density. The oceanic sea level spectrum is red, meaning that it has large variability at long periods. In contrast, the atmospheric spectrum is nearly white with variability nearly uniform across the spectrum (Chelton and Davis, 1982). Roden (1966) suggests that disturbances in the ocean take longer to decay than in the atmosphere.

The Northeast Pacific and the Gulf of Alaska (GOA) are influenced by two semi-permanent atmospheric pressure centers: the Aleutian Low (AL) and the North Pacific High (NPH). Between these centers, sea level pressure (SLP), wind and ocean variability are markedly different. The

boundary between these pressure systems in the Northeast Pacific lies, on average, between 40-45°N (Lisitzin and Pattullo, 1961; Roden, 1966; Enfield and Allen, 1980; Chelton and Davis, 1982). At lower latitudes in the Northeast Pacific, the NPH dominates, whereas the AL dominates north of this boundary.

The AL pressure patterns are not static, but rather are manifested in the persistent reoccurrence of North Pacific cyclones, which makes the AL a statistical definition. Low pressure systems tend to create conditions that favor higher wind speeds, higher precipitation and increased cloud cover. The strength and presence of the AL is variable on both annual and decadal time scales. The seasonal alternation of atmospheric pressure systems in GOA changes with the equator/pole temperature gradient. In winter, the AL is dominant and has an average SLP of 1002 mb. In summer, the AL frequently moves north to be replaced by the NPH that has an average SLP of 1024 mb (Wilson and Overland, 1986). Winds in the GOA are generally characterized by strong downwelling in winter, and mostly downwelling with occasional upwelling in summer, although this varies spatially (Stabeno et al. 2004; Royer, 2005). Wind stress curl over the GOA increases by an order of magnitude from summer to winter (Reed and Schumacher, 1981).

From the average positioning of the AL and NPH, the variance of wind varies with latitude. The variance of wind stress decreases monotonically from Yakutat, AK to Neah Bay, WA, and the wind stress variance is uniform farther south (Enfield and Allen, 1980). The integral time scale of wind stress decreases poleward; at the equator it is 3 months, at 23 °N it is 2.3 months, and in the GOA it is less than two weeks (Enfield and Allen, 1980; Livingstone and Royer, 1980).

Although North Pacific cyclones can form in the GOA, they typically originate east of Japan and travel into central and southeast Alaska. The storm track is to the northeast, and generally follows the mid-tropospheric level of 500 hPa. The Kuroshio Current plays an important role in replenishing storm activity in winter (Rodionov et al., 2007). GOA is the graveyard for these storms because the coastal mountains act as a barrier for propagation into the continent.

The highest storm frequency in the GOA occurs in the months of October to April. These storms can stall for days, but on average, one storm occurs every four to five days.

As storms move near land the coastal mountains force warm moist air to high elevations, which cause condensation and lead to high levels of precipitation and cloud cover (Wilson and Overland, 1986; Weingartner, 2007). For a large part of the year in GOA cloud cover inhibits solar radiation; for example, Yakutat has 278 cloudy days per year (Western Regional Climate Center-WRCC).

The cyclonic influence of the AL forces the cyclonic circulation of the Alaska gyre to center over the GOA basin. The counterclockwise circulation of the gyre is also mirrored over the shelf, or coastal circulation. The GOA basin is largely affected by latitudinal wind stress curl, while the coastal region is largely affected by coastal winds and freshwater runoff (see below). Basin circulation is most intense during the first half of the year and weakest in November and December (Wyrtki, 1975), while the coastal flow becomes high in late fall through winter (Schumacher and Reed, 1980; Weingartner et al., 2005). The coastal circulation is the Alaska Coastal Current (ACC) (Royer, 1981; Reed and Schumacher, 1986) that flows along the entire coast from British Columbia to the Aleutian Islands.

The arcuate shape of GOA is bounded on the north and east by a mountainous coastline over the approximate region of 134-150 ^{o}W and 56-61 ^{o}N. The ocean and atmosphere in this region are highly variable because of: high latitude, tectonics, coastal mountains, glaciers, and the AL. Physical properties in GOA undergo large seasonal fluctuations due to the high latitude setting.

The coastal mountains, which extend from northern Washington to the Aleutians, are a result of convergence and strike-slip plate boundary interactions between the Pacific and North American plate, and the Yakutat microplate (Eberhart-Phillips et al., 2006). These interactions continue today with the Pacific plate colliding with the North American plate at an average of 5-7 cm yr^{-1} (Sheaf et al., 2003; Gulick et al., 2007). The Yakutat microplate lies between these

plates and further complicates the tectonic interactions because of its anomalous thickness (Freymueller et al., 2007). Coastal GOA has some of earth's highest coastal mountains and greatest topographic relief in the western hemisphere. Coastal elevations range from 3 to 6 km (Sheaf et al., 2003; Gulick et al., 2007), and extend more than 60 km inland (Wang et al., 2004). The regional topography and bathymetry are continuously reshaped by tectonics and frequent earthquakes. This complicates the assessment of long-term sea level trends in GOA (Larsen et al., 2003).

The mountains surrounding GOA support 13 % of the mountain glaciers on earth (Arendt et al., 2002). Glaciers cover around 18 % of the GOA drainage basin and account for around 47 % of freshwater discharge (Neal et al., 2010). Neal et al. (2010) indicates that around 90 % of the annual glacier volume loss for glaciers in Alaska and Canada discharge into the GOA basin rather than into the interior (of Alaska), which flows into the Bering Sea or Arctic Ocean. Much of the GOA discharge occurs in the central and southeast regions, which comprise 50 % of the drainage area but 66 % of the total freshwater discharge (Neal et al., 2010). Via the ACC, the GOA discharges into the Bering and Chukchi Seas, and effectively shunts low salinity water into the Arctic Ocean (Weingartner et al., 2005; Woodgate et al., 2006; Carmack, 2007). In addition to its influence on salinity (and hence ocean density), the GOA discharge is an important source of dissolved and suspended materials to higher latitudes.

The coastal mountains and the AL together promote high precipitation in GOA. Average annual precipitation rates of 2-8 m yr^{-1} are common at coastal stations in the GOA (Wilson and Overland, 1986). The 2.5 m precipitation contour runs along the coast from Alaska to Washington (Royer, 1982). Estimating GOA discharge is challenging, and most discharge models underestimate coastal runoff (Royer, 1982; Wang et al., 2004). The orographic control of mountainous airflow causes higher rates of precipitation at higher elevations than at low elevations, and measurements at high elevations are not easily made and, therefore, are sparse. The majority of discharge comes from small rivers, streams and creeks, most of which are unmonitored and the flow unquantified. Wang et al. (2004) and Neal et al. (2010) estimate

that between 74 and 78 % of discharge in GOA is attributed to these unmonitored sources. The extreme runoff rates into the GOA basin can be brought into perspective by considering that the specific runoff (runoff per drainage basin area) of GOA is approximately two to six-fold greater than the Amazon and Congo Rivers (Neal et al., 2010). This high specific discharge of GOA is primarily due to high levels of precipitation, relatively low levels of evapotranspiration, and the abundance of relatively short and steep topography (Royer, 1982).

Air temperature determines the timing and magnitude of freezing and thawing, which controls the timing and magnitude of coastal discharge, regional hydrography, and sea level. Precipitation (data from Seward) is highest around September and October just before freezing sets in. Freezing usually begins in October and November while thaw occurs in March and April. Most discharge occurs during the months of May to December as above freezing temperatures melt snow, ice, and glaciers. Maximum coastal discharge occurs in October due to high glacial melt and increased precipitation during this time (Royer, 1979; Royer, 2005). The rapid drop of discharge in October occurs as air temperatures fall below the freezing point; however, substantial discharge occurs throughout the year (Royer, 1982). This coastal discharge lowers salinity near shore, and contributes to the circulation of the ACC. Because of the substantial discharge throughout the year, the ACC is a continuous feature of GOA oceanic circulation.

Coastal freshwater discharge has a major seasonal influence on near shore oceanic circulation and has been identified as the first order driving mechanism for the coastal flow in GOA (Royer, 1981; Reed and Schumacher, 1981; Royer, 1982). The ACC is forced by freshwater and wind. The cross-shore steric height difference is caused by coastal freshwater and downwelling winds that are subject to the Coriolis force, which trap the ACC tightly against the coast. Greater freshwater discharge and/or downwelling winds increase ACC transport. Transport of the ACC is greatest when the forcing by freshwater and downwelling winds coincide. In general, this occurs between September and January when freshwater discharge (or accumulation on the shelf) is high and downwelling wind event frequencies and speeds are increasing. Conversely, ACC transport is lowest when the forcing of these variables is weakest (Stabeno et al., 2004).

The width of the ACC is highly variable but typically extends 10 to 40 km offshore (Weingartner et al., 2005). Long-term hydrography for the GOA shelf has been monitored at oceanographic station GAK1 since 1970. GAK1 is positioned at the mouth of Resurrection Bay, south of Seward, which sits at the head of the bay approximately 32 km north of the mouth. With a relatively short data record (~7 yrs) from GAK1, Royer (1979) concluded that the primary forcing mechanism on the upper 100 m of the water column was controlled by freshwater, while the lower water column was forced by winds.

Sea level responds simultaneously to oceanic and atmospheric processes on all time scales; however, the influence of the atmosphere increases with latitude. The principal driving mechanism of sea level at low latitudes is from steric changes, while at high latitudes SLP is dominant (Pattullo, et al, 1955; Roden, 1960). The adjustment for atmospheric pressure is of little significance to sea level stations in the tropics, because pressure fluctuations are small. For example, SLP accounts for only 6 % of total variance in the Bermuda sea level record (Wunsch, 1972).

At low latitudes, sub-annual variations of sea level are largely affected by temperature changes originating from wind-driven Ekman transport. At the annual cycle, the phase of heating and cooling are in-phase with the annual cycle of sea level. For periods greater than the annual cycle, equatorial wave signals are prominent in the sea level record (Wyrtki, 1975; Chelton and Davis, 1982). At high latitudes, sub-annual variations of sea level are largely affected by salinity changes originating from coastal runoff and wind-driven Ekman transport (Royer, 1982). At the annual cycle, the steric component and sea level are out of phase and become in better agreement when the influence of SLP is removed (Reid and Mantyla, 1976).

Sea level (and wind) at stations south (north) of the Subarctic Front and the bifurcation of the North Pacific Current are most coherent with stations to the south (north), while coherence is low or insignificant between adjacent stations across this boundary. On timescales greater than monthly, sea level is coherent over long spatial scales. It is most coherent over distances of a

few hundred kilometers and is not affected by SLP as SLP is also coherent over these spatial scales. At spatial scales on the order of 1000 km sea level coherence is still significant but decreases when corrected for SLP. Sea levels south of the bifurcation are in phase over distances of 1200 km (Roden, 1966), likely due to propagating waves of equatorial origin (Enfield and Allen, 1980; Chelton and Davis, 1982). Equatorial signals dissipate with increasing latitude and generally become noisy north of San Francisco (Enfield and Allen, 1980; Chelton and Davis, 1982); this is most likely due to the increase in coherence between the atmosphere and sea level, which works to mask these signals at high latitudes (Melsom et al., 2003).

Sea level in the global ocean is rising from the melting of stored snow and ice, and from volume expansion (originating from an increase in freshening or heat). Melting of ice adds to the volume of the ocean, while expansion simply increases the volume that is already present. Arendt et al. (2002) estimates that glacial melt around GOA contributes around 0.14 $mmyr^{-1}$ toward global sea level rise. According to Gardner et al. (2013), glacial melt contributes ~ 1.5 $mm\ yr^{-1}$ to global sea level rise, which accounts for around 60 % of the total sea level increase. In some regions in the world, including the GOA, sea level is actually falling due to continental rebound. As the mass of frozen water on land has diminished over thousands of years due to natural climatic cycles, the earth's surface slowly rises in response. Continental rebound is spatially variable across GOA. Roden (1966) cautioned against assuming long-term sea level trends originate from climatic forcing. He speculated long-term changes are likely the differential in land motion, pointing out that trends at nearby stations can be different. Long-term sea level change in the ocean is a superposition of each of these three mechanisms described, that is, melting of stored snow and ice, volume expansion and continental rebound.

The long-term changes of physical parameters in GOA are related to large-scale climate change on earth, some of which include: atmospheric and oceanic temperatures, the hydrologic cycle, and climate related extremes (IPCC, 2014). According to Durack et al. (2012), ocean salinity changes over the past 50 years indicate intensification of the global water cycle. In regions where annual precipitation (P) is less than evaporation (E), such as the subtropical North Pacific,

the oceans are becoming saltier. In regions where P>E, such as the GOA, the oceans are becoming fresher. Because of the Clasius-Clapeyron relationship, atmospheric moisture content increases as air temperatures increase. Indeed, a 1 ^{o}C increase in lower troposphere temperatures should lead to a 7% increase in atmospheric moisture content. Durack et al. (2012) estimate that moisture content has already increased by 4 % over the past 50 years due to the observed 0.5 ^{o}C warming of the earth's surface. These mechanisms are occurring in the GOA. The GOA region (and British Columbia) has some of the highest glacier volume loss rates on earth (Neal et al., 2010; Gardner et al., 2013). Of the Alaskan and Canadian glaciers examined over a 50 yr period, 95 % of these have thinned (Arendt et al., 2002). They also found that from 1995 to 2001 glacial thinning at twice the rate measured from the 1950 to 1990.

Many oceanic and atmospheric states (or conditions) are either controlled or correlated to other climatic phenomena; for example, El Nino Southern Oscillation (ESNO or El Nino), Pacific Decadal Oscillation (PDO) and the AL have all been shown to be related in some way. Rodionov et al. (2007) describes how PDO regime shifts correspond to shifts in the strength of the AL. The PDO is the leading empirical orthogonal function of sea surface temperature in the North Pacific Ocean. It is not a dynamic mode but rather it arises from the superposition of the forcing of El Nino, AL, and the Kuroshio-Oyashio extension and a function of time scales (Schneider and Cornuelle, 2005). Positive (negative) PDO is associated with enhanced (diminished) precipitation and runoff in GOA (Royer, 2005). Weingartner et al. (2005) found high correlations between discharge and SLP differences between Seward and Ketchikan; they hypothesized that enhanced runoff occurs when anomalous winds from the southwest bring warm and moist air onto the coastal mountains. The influence of EL Nino on PDO was described by Mantua et al. (1997). Rodionov et al. (2007) described the relationship between ENSO and the AL. These authors note that since 1977, six of the ten strongest years (from 1950) for the AL occurred during El Nino years. It is reasonable to assume that GOA parameters are forced by each of these mechanisms, each operating on different time scales. The ability to distinguish the influence of individual climatic forcing mechanisms on GOA parameters is difficult since they

force and interact simultaneously, either cancelling or accentuating their effect on GOA climate (Papineau, 2014).

In this study I quantify several aspects of temporal variability in Seward sea level (SSL). These are generally presented in order of highest to lowest variability, and include SSL's response to: tides, meteorological forcing (atmospheric pressure and wind), and steric influences. The relationship of several climatic indices to GOA sea level, hydrography and discharge are also examined. I also examine long-term trends in discharge, hydrography and sea level at Seward, Yakutat and Sitka (hereafter referred to as GOA sea level). The principal focus is on sea level at Seward because of the abundance of hydrographic data from oceanographic station GAK1. To a lesser extent, I also examine sea level variations at Yakutat and Sitka (Figure 1).

2 Datasets and Methods

The physical parameters under examination include the hydrographic properties of the water column at GAK1, sea level at Seward, Yakutat and Sitka, atmospheric pressure and winds, freshwater discharge and climate indices believed to be relevant to the GOA. The period of interest is 1970 to 2011, corresponding to when the hydrographic data began to be collected. The annual cycle is of interest in our examination and, therefore, was not removed from the data records, unless otherwise specified. Due to the high latitude and physical setting of GOA, there is a strong seasonal difference in the variability of physical parameters in GOA. Seasonal examinations are made using spectral analysis.

2.1 Data

2.1.1 Discharge

Discharge data come from Royer's (1982) discharge model and I use the time series corresponding to Seward discharge; these data are found at http://www.ims.uaf.edu/gak1/.

2.1.2 Atmospheric

Atmospheric data (SLP and wind) were acquired from the National Center for Environmental Prediction (NCEP) and North American Regional Reanalysis (NARR). Atmospheric data obtained from NCEP were used for analysis of data before 1980 at the locations of Seward (60 ^{o}N, 150 ^{o}W), Yakutat (60 ^{o}N, 140 ^{o}W) and Sitka (57.5 ^{o}N, 137.5 ^{o}W). NARR atmospheric data were used for analysis after 1980, taken from the locations of Seward (59.8125 ^{o}N, 148.75 ^{o}W), Middleton (59.4375 ^{o}N, 146.3125 ^{o}W), Yakutat (59.625 ^{o}N, 139.75 ^{o}W) and Sitka (57 ^{o}N, 135.25 ^{o}W).

Wind data from these sources come in zonal (U-wind) and meridional (V-wind) components, and wind stress was computed according to Large and Pond (1981). Along-shore wind stress (ASWS, τ^{a}) was constructed by rotating the U and V-wind components to an appropriate along-shore direction that depended on coastal orientation, cross shore wind stress (CSWS, τ^{c}) was computed similarly for the cross-shore direction. I adopted the sign convention where negative

ASWS (CSWS) is to the west, or counterclockwise around the arcuate GOA coastline (offshore). I symbolized the ASWS as τ^a_{Sew} , τ^a_{MI} , τ^a_{Yak} and τ^a_{Sit} , which represent ASWS near Seward, Middleton Island (Middleton), Yakutat and Sitka. CSWS was denoted similarly.

2.1.3 Sea Level

Sea level data from Seward (SSL), Yakutat (YakSL) and Sitka (SitSL) were obtained from the University of Hawaii Sea Level Center. Hourly data were used to analyze the tides. The sea level data were subsequently subsampled to three hourly intervals after filtering with a low-pass 38 hr 8^{th} order Butterworth filter to remove tides. There were gaps in these data and monthly averages were computed regardless of the amount of data missing in each month. From 1970-2010, SSL, YakSL, and SitSL time series data were missing 55, 17 and 0 months out of 492 months respectively. SSL has nearly 5 years of missing data from 1974-1979. In 1973 and 1976, YakSL has about 6 months missing in each year.

2.1.4 Hydrography

I examined the temperature, salinity and geopotential height (GH) at hydrographic station GAK1 (59.845 ^{o}N, 149.467 ^{o}W) positioned at the mouth of Resurrection Bay at a depth of about 261 m. There have been two separate data collection methods at GAK1, hydrographic casts and moorings. Hydrographic casts began in December 1970 and continued to the present, and Figure 2 shows the number of months, in each year since 1970, when data were obtained from hydrographic casts. Over the first 20 years of GAK1 sampling, ships of opportunity irregularly collected data throughout the year. From 1990 to present, the station has been sampled approximately monthly (Royer, 2005). There are ~470 total hydrographic samples collected from 1970-2010. After monthly averages were computed there are ~285 months in which samples were collected, this is the sum of the number of observations in Figure 2.

Of all the data sets used in this study, the GAK1 hydrographic casts from 1970 – 2010 had the most missing data, and monthly anomalies were created by using all available data. To eliminate missing data markers (NaN), and to eliminate signals at periods < 1 year, the monthly

anomalies were smoothed with a 13 month running average. Though crude, this procedure allowed me to make long-term comparisons using the water column data. Smoothed monthly anomalies were used for climatic comparisons, while monthly anomalies, without smoothing, were used for long-term trend analysis.

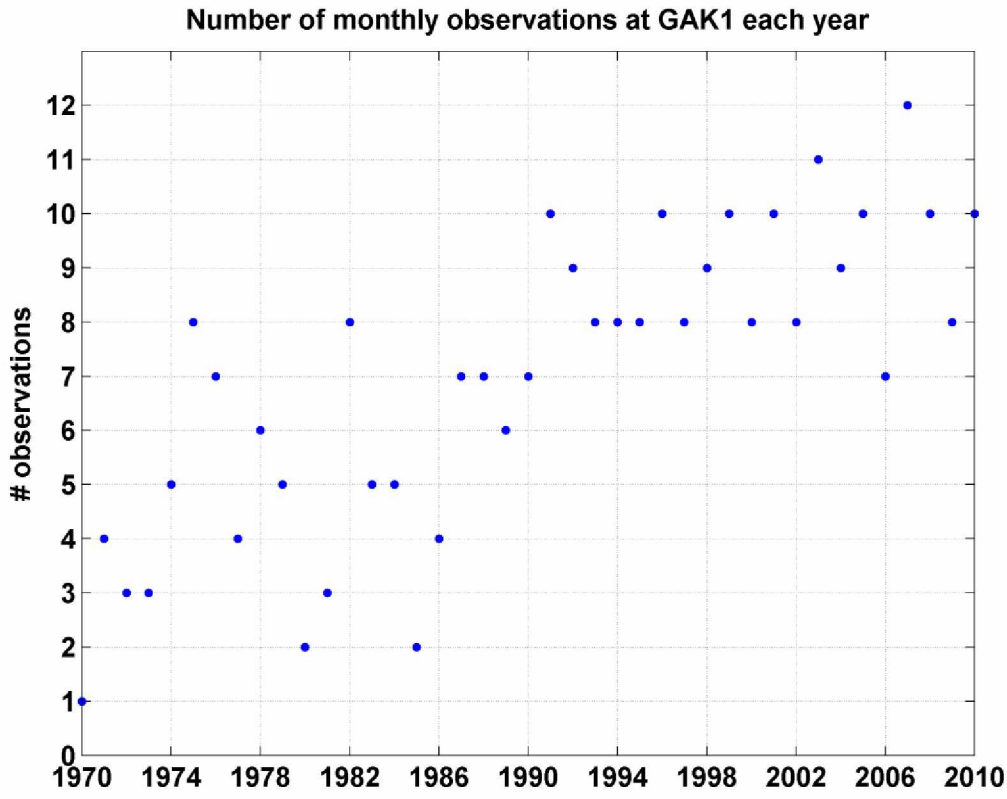

Figure 2. The number of monthly observations in each year from which hydrographic casts have been collected at GAK1 for the period 1970 - 2010.

Moorings have been deployed at the GAK1 location since 1998 (Figure 3), although data are missing for the majority of 1999, 2002, all of 2003, and part of 2004. Missing data after 2004 occur between annual instrument exchanges, which range between 0 and 26 days. Most mooring instruments collected data at 15 min intervals. In most years the GAK1 mooring was equipped with seven CTD instruments placed near 20, 30, 60, 100, 150, 200 and 250 m. In order

to create a time series of GH referenced to 200 m (hereafter GH200) I needed to estimate a continuous density profile over the upper 200 m using data from discrete depths. Since values of temperature and salinity at the surface (0 m) were not available, they had to be estimated. I did so by computing the slope as a function of depth for temperature and salinity from the upper two instruments and then used this slope via extrapolation to infer surface temperature and salinity.

Once the surface values were determined, linear interpolation was used to create temperature, salinity and density profiles at 1 meter intervals. Using Equation 1, geopotential height (GH) is expressed in units of meters (Pond and Pickard, 1983) with the variables g, S, T and P being gravity, the in situ salinity, temperature, and pressure.

$$GH = \frac{1}{g}\int_0^z \alpha(S,T,P) - \alpha(35,0,P)dz \qquad (1)$$

Other GH time series computed at different depths of integration were created in a similar fashion, as well as the computation of GH from hydrographic casts. These data were subsampled into hourly intervals for tidal analysis, and for subtidal analysis I applied a low-pass 38 hr 8^{th} order Butterworth filter followed by subsampling to three hourly intervals. The continuous time series of GH200 during the period of 2004 to 2011 (7.09 yrs) was used for spectral and coherence analysis. Figure 3 shows the GH200 time series derived from the moorings.

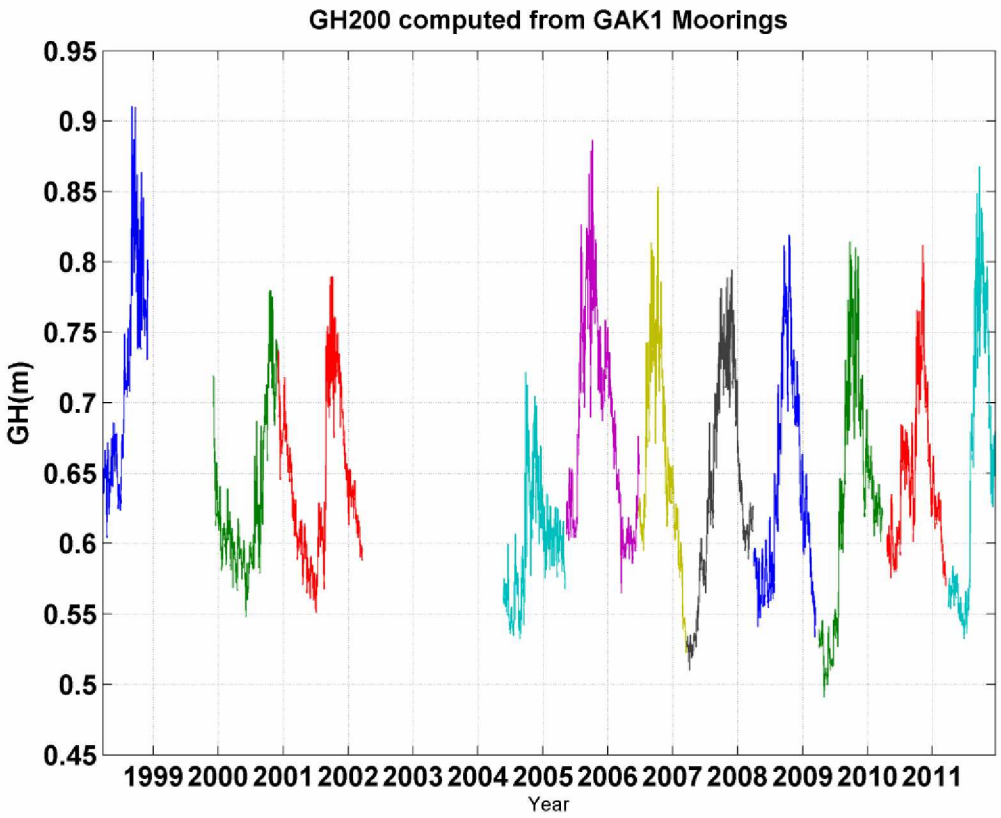

Figure 3. The mooring derived time series of geopotential height (GH) from 1998 to 2012. Each mooring deployment has a distinct color.

Various errors occur when GH is calculated from mooring data; however, these errors are small, and I have identify three sources, 1) missing data, 2) seasonal differences in hydrography, and 3) the number of instruments used to create the temperature and salinity profile (and eventually GH).

About 2.9 % of the data were missing for the period of 2004 to 2011 due to gaps associated with mooring turn-around. These gaps were filled by linear interpolation. The error associated with linear interpolation is small because GH changes slowly throughout most of the year. However, in the summer months rapid changes in GH can occur in a short time span and interpolation could be problematic, but mooring exchanges do not occur during this time.

To quantify how seasonal differences in hydrography and the number of instruments affect the estimation of GH from mooring data, I correlated (using r^2) the estimated GH to that of GH calculated from data collected from hydrographic casts. Hydrography varies seasonally, primarily from freshwater discharge. In the summer months the near-surface water column can exhibit strong vertical temperature and salinity gradients, while the winter months have a lesser gradient. Because of this, GH estimated in the winter months are nearly 100 % correlated to the hydrographic casts, while the summer months are ~98 % correlated. Also, independent of season, density gradients are strongest at the ocean surface; this results in lower correlations between GH estimated from mooring data and hydrographic casts in the upper water column compared with the lower water column.

The number of mooring instruments also affect GH estimation from mooring data. In all years except 2001, five or more instruments provided data for estimating GH. In 2001 there were only four instruments located at 25, 60, 190 and 250 m. Using these four instruments to compute GH200, the correlation of estimated GH to hydrographic casts was ~99 %. To combine these influences to find the maximum error that could occur, I isolated the summer months in 2001 when four instruments were used, and the overall correlation between estimated GH to GH computed from casts was ~98 %. From this, I concluded that four instruments can reliably estimate GH, but more instruments do improve this estimation. However, more than seven instruments (the maximum number deployed at GAK1) do not significantly improve GH estimations.

2.1.5 Climatic Indices

I explored the relationship of GOA parameters to the following climate indices: North Pacific Gyre Oscillation (NPGO), Pacific Decadal Oscillation (PDO), El Nino Southern Oscillation Index (SOI) for the period from 1971 to 2010. NPGO data was downloaded at http://www.o3d.org/npgo/npgo.php. The NPGO is defined as the second principal component of sea surface temperature in the Northeast Pacific (Di Lorenzo et al., 2008). PDO data were

downloaded at http://jisao.washington.edu/pdo/PDO.latest. The PDO is defined as the first principal component of sea surface temperature in the Northeast Pacific (Mantua et al., 1997). The SOI is a measure of the atmospheric pressure difference across the Equatorial Pacific Ocean, between Taihiti and Darwin, Australia. SOI data were downloaded from http://www.bom.gov.au/climate/current/soihtm1.shtml. In order to eliminate signals at periods < 1 year, all climatic comparisons were made with monthly anomalies that were smoothed with a 13 month running average.

2.2 Methods of Analysis

I employed various methods for data analysis, in both the time and frequency domain. In the time domain I used linear and sinusoidal regression, auto and cross correlations, and linear correlations. The term correlation, used throughout, refers to the coefficient of determination $\left(r^2\right)$, which expresses the percent of the variance accounted for by the correlation. Confidence limits on means were computed using Student's t-distribution. Linear regressions of monthly anomalies were used for long term analysis (from 1970-2010). Cross correlations of data ranged over the time period of 1971 – 2010, except for Seward sea level, which ranged from 1979 - 2010 due to missing data in the years from 1974 to 1978; this analysis used monthly anomalies smoothed with a 13 month running average.

In the frequency domain I used spectral, frequency response function (FRF) and coherence analysis techniques, each of which is based on linear mean square estimations. A complete description of these methods is described in section 2.2.1. (see below). Here, I simply highlight the methods used during the computation of spectral and coherence analysis.

Prior to performing all spectral analysis I removed the mean and a linear trend from the time series. In all cases I block averaged each transformed (the square of the Fourier transform of the time series) time series segment and in most cases the highest frequencies are further averaged to reduce noise. The number of data segments used in spectral averaging were denoted as nfft. Data segments are 50 % overlapped and tapered with the Hann taper.

However, seasonal spectral estimates did not employ overlapping, but instead block averaged each transformed 90 day segment when data were available. Each 90 day segment was taken from the winter (nfft = 30) and summer months (nfft = 29). Summer months included June, July and August; winter months included December, January and February. Spectral energy plots are presented in variance preserving power spectral density (VPSD) (Emery and Thompson, 2000). Coherence squared (γ^2) expresses the percent of variance explained by the relationship of the two time series in the frequency domain; herein, the term coherence implies coherence square. Confidence limits for the FRF and phase were computed from joint-confidence intervals based on F-distribution.

Continuous data, depending upon length and application, were isolated for spectral analysis. When data were mutually coherent multiple and partial coherence analysis was employed. Except for tidal analysis, only sub tidal periods of greater than 2 days were resolved. All computations considered significant meet or exceed the 95% confidence level.

2.2.1 Methods of Spectral and Coherence Analysis

2.2.1.1 Introduction

Spectral analysis is a powerful tool for understanding how the variance is distributed as a function of time scales for processes (or variables) that vary periodically or even episodically (Von Storch and Zwiers, 1999). This variance is expressed through the use of power spectral density (PSD), which can simply be thought of as the variance contained in each frequency. PSD can be estimated through the use of the Discrete Fourier Transform (DFT), probably the most widely applied signal analysis method in use. The DFT is used in numerous fields including oceanography (Park and Watts, 2005), neurology (Rosenberg et al., 1989), aviation (Piersol, 1967), and the stock market (McCullough, 1995), for example. Methods similar to PSD have been used to identify hidden periodicities in geophysical data for over one hundred years (Schuster, 1898).

Present data analysis techniques have two main advantages over those of the past, 1) the use of the computer which provides easy, precise, rapid computation of data, and 2) the possession of relatively long geophysical data records allows an increase in statistical reliability. Mathematical programs aid in the processing of this data. For example, Matlab (used throughout this thesis) is a popular software package used in the geosciences that has the capacity to handle most data sets, and its built-in functions can simplify complicated algorithms and tedious calculations. Throughout this thesis I will present the Matlab functions used where applicable.

In this section I outline the spectral estimation techniques used in this thesis. These methods include PSD, frequency response function (FRF), single and multiple input coherence, and the approaches used to estimate errors on the spectral estimates. I also explicitly define equations for two and three input multiple and conditioned coherence analysis with their associated errors. Derivations can be found in standard spectral analysis texts (Bendat and Piersol, 1970, 1980, 2000; Hannan, 1970; Koopmans, 1974; Otnes and Enochson, 1978; Von Storch and Zwiers, 1999; Emery and Thompson, 2000). The key to ensuring proper application of the methods presented in this section is to test them on fabricated sinusoidal signals of known amplitude and phase.

2.2.1.2 The Frequency Domain

Time series records $x(t)$ and $y(t)$ can be transformed from the time domain into the frequency domain using the DFT, or the Fast Fourier transform (FFT) algorithm. Geophysical data records are often composed of many superimposed signals with different frequencies that form a single time series record. The idea behind the Fourier transform is to decompose a time series record into a series of discrete frequencies that have associated amplitudes that are inherent to the time series record. The frequencies resolvable depend upon the length of the time series segment that is analyzed; longer time series segments produce greater frequency resolution than smaller segments. The longest period resolvable is the fundamental period (T_f), which is

equal to the time length of the segment used to compute the DFT. The DFT should be applied to continuous (e.g., gap-free) time series that contain regular sampling intervals.

Time series $x(t)$ that have been Fourier transformed are denoted as $X(f_k)$. The output of the DFT is a symmetric, or two sided function made of real and imaginary components, where $X(f_k) = X(f_k) + iX(f_k)$. I will exclude the details regarding the analytic computation of the DFT while referring the reader to standard texts (in Matlab, the DFT is computed from the *fft* function). Uhlen (2004) provides useful guidance on computing spectra from Matlab. For simplicity, I use half of the function since the function is even sided, and only half is unique. To preserve the total variance, a correction factor of two is then applied to the PSD functions. Earlier works (Cooley and Tukey, 1965; Bingham et al., 1967) suggest the length of the data that are to be transformed be a power of two in order to take advantage of the efficiency of the FFT algorithm. However, this is unnecessary for the analysis presented here, given the power of a personal computer.

2.2.1.3 Frequency

The segment length T determines the number of discrete frequencies that are resolvable in the analysis. The segment length is found by multiplying the sample rate (Δf_{sr}) of the data to the fundamental period T_f, or $T = \Delta f_{sr} \cdot T_f$. The fundamental period is determined by the user to be the longest resolvable period. For example, if I want to resolve a 60 day period from data that have a sample rate (Δf_{sr}) of 8 samples day^{-1}, then the segment length will be $T = 60 \cdot 8 = 480$ samples.

The discrete frequencies for the one sided spectrum are found from $f_k = \Delta f_{sr} \cdot \frac{k}{T}$, where $k = 0,1,2...\left(\frac{T}{2}\right)$ are integer values (where the size of f_k is half the segment length because only one side of the spectrum is of interest). The value of the DFT for $k = 0$ is the sum of the time series data over the time interval of interest, based on Perseval's theorem. The $k = 1$ value is

the fundamental frequency; the $k = \frac{T}{2}$ value is the Nyquist frequency. The $k = 0$ and $k = \frac{T}{2}$ values are generally ignored (Bendat and Piersol, 2000), leaving the spectrum to be examined at frequencies

$$f_k = \Delta f_{sr} \cdot \frac{k}{T} \tag{2}$$

where $k = 1,2,\ldots\left(\frac{T}{2} - 1\right)$. The period is simply $T_p(f_k) = \frac{1}{f_k}$.

2.2.1.4 Auto and Cross Spectrum

Perseval's theorem, the Fourier transform, and a doubling of the PSD, lead to the auto and cross-spectrum expressions that are the foundation of FRF and coherence analysis. The PSD represents an estimate of the variance of the time series, since the true variance is unknown. In the following, all estimates will be denoted by a caret (^) while * denotes the complex conjugate. The auto-spectral density functions are real valued and calculated from:

$$\hat{G}_{xx}(f_k) = \frac{2}{T} X_i(f_k)^* X_i(f_k) \text{ and } \hat{G}_{yy}(f_k) = \frac{2}{T} Y_i(f_k)^* Y_i(f_k). \tag{3, 4}$$

The cross-spectral density function is estimated as:

$$\hat{G}_{xy}(f_k) = \frac{2}{T} X_i(f_k)^* Y_i(f_k) = \hat{G}_{xy}(f_k) = C_{xy}(f_k) + iQ_{xy}(f_k) \tag{5}$$

where the expression on the right is written in complex form. The variable $C_{xy}(f_k)$ is the co-spectrum and $Q_{xy}(f_k)$ is the quad-spectrum and $i = \sqrt{-1}$. The cross spectrum $\hat{G}_{xy}$ is defined using $X(f_k)^* Y(f_k)$ not $X(f_k)Y(f_k)^*$ and follows the property that $\hat{G}^*_{xy}(f_k) = \hat{G}_{yx}(f_k)$ and $\hat{G}^*_{xy}(f_k)\hat{G}_{xy}(f_k) = \hat{G}_{yx}(f_k)\hat{G}_{xy}(f_k)$ (Bendat and Piersol, 1980). The cross-spectrum relates the variability between the input and output time series in the frequency domain, and can be computed between any two continuous data sets, provided the above procedures are followed.

The auto and cross-spectra are useful on their own but are often an intermediate step in computing the FRF and coherence. All spectral calculations are a function of frequency, but hereafter for simplicity, the frequency dependence will often be omitted but nevertheless implied.

The remaining analysis is built upon the above methods. I will now focus on methods that improve the statistical reliability of the spectral estimates. According to Bendat and Piersol (2000), "The basic computations for the FFT are straightforward, but there are various "grooming" operations that are often added to the computations to improve the quality of the resulting estimates." Accurate PSD estimates are essential in making reliable FRF and coherence estimates.

2.2.1.5 Grooming Operations

Various methods can be used to increase the reliability of spectral estimates; the most basic methods described are side lobe suppression and spectral averaging. Other grooming operations not used in this study are zero-padding and pre whitening. The latter two procedures are described by Emery and Thompson (2000); Uhlen (2004) utilizes zero-padding with Matlab.

2.2.1.5.1 Side-lobe Suppression and Spectral Windows

Side-lobe leakage occurs when power in one frequency undesirably leaks into nearby frequency bands creating noise (or bias) in those bands. Leakage can introduce significant anomalies far from the main signal lobe in the spectrum. This noise originates during analysis when input signals (as a function of frequency) are not integer values of the segment length, and also, if the data are sinusoidal or narrow band in character. Side-lobe leakage can be changed by changing the amplitude of the ends (beginning and end) of the data segment that is to be transformed.

In a rectangular data window the amplitude of the data is not changed; this window yields the narrowest main-lobe and is best for separating closely spaced peaks in the power spectrum.

The shortcoming of this window is that it produces the greatest side-lobe leakage of all spectral window types and introduces significant anomalies far from the main lobe. This undesired effect is easily seen by examining the coherence of fabricated data calculated with a rectangular window. In this case, the signals will be coherent at frequencies where there was no signal assigned because of side-lobe leakage.

The use of a tapered data window can reduce side-lobe leakage. Tapering the data reduces the amplitude at the ends of each time series segment that is to be transformed. There are many tapering options available and each taper has different properties, but in general, data tapers reduce side lobe leakage but at the cost of a reduction in signal power and a decrease in spectral resolution. The Hann window (the *Hann* function in Matlab) is believed to be the best compromise (Harris Semiconductor, 1997; Nuttall, 1971) between these tradeoffs. The Hann window tapers the data to zero at the ends of the time series segment.

Substantial signal power is lost when tapering; for example, the Hann window loses 5/8 of the total power compared to the rectangular window. To correct for this variance or power lost, a correction factor of $\sqrt{\frac{8}{3}}$ (Koopmans, 1974; Priestley, 1981) is multiplied in equations 3-5, or equation 6 if block averaging is utilized. The loss of signal variance can be overcome, to some extent, by overlapping tapered windows. Welch (1967) first described a procedure to estimate PSD by averaging 50 % overlapping windows; I will follow Nuttall's (1971) nomenclature by referring to Welch's methods as weighted overlap segmented averaging (WOSA). WOSA was popularized in the 1960's and is probably the most widely used spectral estimation procedure to date (Carter, 1987; Bendat and Piersol, 2000; Rabinovich and Stephenson, 2004; Park and Watts, 2005; Ryan and Noble, 2006). Hereafter, I use WOSA with the Hann taper. Other details regarding WOSA are given in later sections.

Tapering the data reduces side-lobe leakage but widens the main lobe of the signal peak, which effectively reduces the resolution power. The widening of the main lobe is equivalent to a slight averaging between adjacent frequencies and the Hann taper spreads the energy of each

frequency to the immediate adjacent frequencies $(f-1, f, f+1)$ with amplitudes of 0.25, 0.5, 0.25. This averaging is demonstrated by Uhlen (2004) and can be quantified by comparing normalized rectangular and Hann windows. There is more power in the signal computed from the Hann window (section 2.2.1.6 describes the procedure for normalizing VSPD). The loss of power and resolution is an acceptable tradeoff for suppression of leakage. If resolution power is critical to analysis then the record length must be increased. An increase in record length will increase frequency resolution but will decrease statistical confidence in the power estimation, as explained in section 2.2.1.7.3. Narrow band data are more sensitive to window choice than broad band data because spectral leakage affects broadband less than narrow band. Moreover, the need to resolve specific periodicities in broad band data is usually not of interest. What is of interest in broadband data is the range across the spectrum in which power is distributed.

2.2.1.5.2 Spectral Averaging

The statistical reliability of the PSD estimate is improved by increasing the number of averages used in estimating the spectrum. The term averaging is technically a misnomer. PSD yields the variance of the signal at each frequency. Calculating the total variance at each frequency is accomplished by summing the variance, at each frequency, of each segment, to compute one PSD estimate. Alternatively, averaging describes the number of segments used to compute the spectral estimate, while summing is the operation used to calculate the estimate. Averaging methods for spectra include block averaging, frequency averaging, or a combination of the two. Bendat and Piersol (2000) describe the various advantages and disadvantages of each averaging method. Block averaging is described first.

2.2.1.5.2.1 Block Averaging

Assuming the signals in the data are repetitious and exact copies of the original signal, it is possible to separate the time series into equally sized blocks (or segments), compute the DFT for each segment, then average the segments in order to increase the statistical reliability of the PSD estimate. The number of segments is a function of the total length of the data record and the segment length used in the DFT. The total number of points (T_{total}) used to estimate

the PSD from the time series is referred to as the effective record length. To determine the number of segments or blocks to be used, the segment length must be chosen to suit the available data. For segment averaging T_{total} is found by dividing the total record length of the time series by the segment length T, then rounding down to the nearest integer. This gives the number of disjoint segments n, which can then be multiplied by the segment length T to yield the effective record length, e.g., $T_{totol} = n \cdot T$.

The segment averaged auto-spectra for time series $x(t)$ is:

$$\hat{G}_{xx}(f_k) = \frac{2}{T_{tot}} \sum_{i=1}^{n} X_i(f_k)^* X_i(f_k) \tag{6}$$

(other auto and cross-spectra are calculated similarly). Block averaging can be accomplished using disjoint segments or overlapped segments. Disjoint sections are completely independent, while overlapping segments can be slightly correlated depending upon the spectral window used and the amount of overlap of the windows (discussed further in section 2.2.1.7.3.). The number of disjoint segments determine the number of overlapped segments ($nfft$) which is calculated from $nfft = (2 \cdot n) - 1$ (Welch, 1967) for 50% overlapping segments. Biltoft and Pardyjak (2009) and Miller and Sigvardt (1998) provide helpful guidance on how segment lengths affect the confidence and frequency resolution of the spectral estimate. Caution must be used, however, when comparing my notation to these references.

2.2.1.5.2.2 Frequency Averaging

Frequency averaging is often used in conjunction with block averaging to smooth spectral noise, usually at the higher end of frequency range. Frequency averaging is accomplished by averaging adjacent frequency bands and replacing those bands with a single averaged band so that each band is independent of adjacent bands. As discussed above, the use of a tapered window inherently averages adjacent frequencies, so to prevent overestimation of the number of resulting averages, the number of frequencies averaged ($freq$) are reduced by factor (l),

where $l = \frac{freq}{2}$ (Marlene Noble, personal communication) when $freq > 2$ and $l = 1$ when $freq <= 2$. Frequency averaging should only be used on adjacent frequencies that have similar phase (Marlene Noble, personal communication) and where coherence changes slowly with frequency (Thompson, 1979).

2.2.1.6 Viewing Power Spectral Density and Estimating Amplitudes of Signals

There are two ways to view the spectrum, one is to plot the PSD and the other is to plot the variance preserving power spectral density (VSPD). When examining PSD, the signal power varies greatly across the spectrum, and this is addressed by plotting with the logarithm of the PSD (y-axis) versus the logarithm of the frequency (x-axis). The PSD has units of variance/frequency, and the $\frac{1}{f}$ factor suggests that the lowest frequencies (longest periods) contain the highest energy.

The VSPD (often referred to as energy) eliminates this effect and displays the spectrum in units of variance as a function of frequency. The VPSD can be utilized for either the auto or cross-spectrum; for the auto-spectrum it is simply $f_k \cdot \hat{G}_{xx}(f_k)$. In this representation, the signal with the greatest energy (variance) will have the greatest area under the curve. VSPD should be plotted on the y-axis and log(f) on the x-axis. Although it is standard practice to plot the power against frequency, it can also be plotted against period to facilitate viewing and interpretation of the time scale of interest.

From the VPSD, one can estimate the amplitude of a signal, at a specific frequency, by taking the square root of the VPSD. However, this is not the preferred method of finding the amplitude of a signal, as it is likely that large errors will arise from low signal to noise ratio, spectral leakage, and inadequate resolving power of the exact frequency. If the amplitude of a signal is desired then harmonic analysis is suggested; however, harmonic analysis techniques

are most appropriate for narrow-band, periodic data (such as tides) rather than broad-band or episodic data.

Often the exact amplitude of the spectrum is less important than the relative amplitude across the spectrum. This is especially true for broadband data. To find the relative power at each frequency, the spectrum can be normalized by dividing by the total energy of the spectrum which is found by integrating over the spectrum. As a word of caution, normalized spectrum will not result in proper units when computing the FRF, unless one is interested in a relative FRF.

2.2.1.7 Spectral Methods for Single Input/Single Output Analysis

A functional relationship often exists between two time series that can be described analytically by single input/single output FRF and coherence analysis. Relationships between the data should have the following properties (Bendat and Piersol, 1970): 1) the system must not respond until an input has been applied, 2) the system must have constant parameters, meaning the response function is time invariant, and 3) the system must be stable. The last condition implies that a bounded input produces a bounded output. And finally, 4) the system must be linear where random inputs with Gaussian probability will produce outputs that also have Gaussian probability. This last property is the most likely to be violated in physical systems. In practice, most physical systems violate at least one of these criteria but unless the system is strongly nonlinear, this analysis can still yield meaningful results in terms of linear relationships. In the following, I omit the frequency dependence on expressions, although this is implied.

2.2.1.7.1 The Frequency Response Model

In this section I discuss the frequency response model and how periodic or episodic impulses of one system can induce a response in another. When comparing time series records each must be continuous, partitioned into equal length segments, and sampled at the same equally spaced time intervals.

The frequency response model describes how a sinusoidal input time series can modify, through the physical system, a sinusoidal output time series at the same frequency. The output signal is likely to respond with an amplitude modulation (either gain or attenuation) and phase shift different from the input signal. Amplitude modulation hereafter will be referred to as the frequency response factor (FRF) denoted by $\left|\hat{H}_{xy}\right|$. It is computed from the absolute value of the input/output cross spectrum relation, $\hat{H}_{xy} = \frac{\hat{G}_{xy}}{\hat{G}_{xx}}$, which contains gain and phase information. In comparison, the alternative, auto spectra relation, $\hat{H}^2_{xy} = \frac{\hat{G}_{yy}}{\hat{G}_{xx}}$ computes the FRF only and yields no phase information since the cross spectrum is not involved (Bendat and Piersol, 1980). The phase (presented in radians) between the input and output signal is calculated from $\hat{\phi}_{xy} = \tan^{-1}\left(-\frac{imag(\hat{H}_{xy})}{real(\hat{H}_{xy})}\right)$. In this phase convention a negative phase occurs if the output lags the input (and vice versa). The four quadrant arctan allows phase to be examined between $-180 \le \hat{\phi}_{xy} \le 180$ degrees using Matlabs's *atan2* function. Once the phase (in radians) is determined, time delay (τ) can be computed from $\tau = \frac{\hat{\phi}_{xy}}{2\pi f_k}$. The coincident-spectrum (co-spectrum), $real(\hat{H}_{xy})$, contains the in-phase information described as the correlation in oscillation between signals with no time lag. The quadrature-spectrum, $imag(\hat{H}_{xy})$, contains the out of phase information described as the correlation in oscillation between signals when the harmonics are delayed by a quarter period with respect to the output (Panofsky and Brier, 1958; Emery and Thompson, 2000). Expressed in polar notation, the FRF and phase form the frequency response function, $\hat{H}_{xy}(f) = \left|\hat{H}_{xy}(f)\right| e^{i\phi(f)}$. This expression is equivalent to the input/output cross-spectrum relation defined above.

2.2.1.7.2 Ordinary Coherence

Coherence squared $\gamma^2(f)$ is the fraction of the variance in the output function accounted for by the input data as a function of frequency, and is analogous to the coefficient of determination (r^2) in time series analysis. Coherence squared ranges between $0 \leq \gamma^2 \leq 1$, where 0 is no correlation and 1 is completely correlated. The terms coherence and coherence squared have been a source of confusion in spectral analysis for many years, as noted by Julian (1975); therefore, it is important to note that I use these terms interchangeably.

If coherence is calculated from one spectral estimate, then coherence will be unity at each frequency with no statistical significance. As n (number of averages) increases away from 1, $\gamma^2(f)$ estimates acquire greater statistical confidence and the noise level tends to depart from 1 enhancing the ability of true signals to be distinguished from noise. Coherence can be calculated by any of the following equivalent expressions.

$$\hat{\gamma}_{xy}^2 = \sum_{i=1}^{n} \frac{(X_i^* \cdot Y_i)^* \cdot (X_i^* \cdot Y_i)}{(X_i^* \cdot X_i) \cdot (Y_i^* \cdot Y_i)} = \frac{\hat{G}_{xy}{}^* \cdot \hat{G}_{xy}}{\hat{G}_{xx} \cdot \hat{G}_{yy}} = \frac{\left|\hat{G}_{xy}\right|^2}{\hat{G}_{xx} \cdot \hat{G}_{yy}} \tag{8}$$

2.2.1.7.3 Error Estimations for Spectral Methods

The two types of error that occur in spectral analysis are bias and random error. Bias errors deal with the frequency resolution of a spectrum while random error deals with the haphazard scatter of the randomness in data from one sample to the next. Decreasing bias and random error are antagonistic features for a fixed record length. Fewer and longer records decrease bias error while increasing random error, while shorter records decrease random error but increase the bias error. In bias error, narrow band signals are subject to a "smearing bias" if the resolution bandwidth is wider than the signal (Otnes and Enochsen, 1978) due to insufficient spectral resolution. Such smearing has a substantially greater effect on coherence than on the power spectrum (Otnes and Enochsen, 1978). These effects can be reduced by increasing the segment length until the frequency in question is resolved. Note however, that bias errors will

be less critical for wide-band data. Von Storch and Zwiers (1999) demonstrate how too few or too many averages lead to either excessive random error or excessive bias error that could result in a high noise floor, or low or false coherence in other frequencies. Their example implies that there must be a balance achieved between record length (i.e., the fundamental period) and number of averages. The availability of long continuous data (large T_{total}) records is ultimately the governing factor for reducing errors during analysis. Assuming that the bias error is small, I next focus on estimating the confidence intervals for random errors, which are reduced by increasing n.

There is no limitation on the maximum number averages of that can be used to estimate the PSD; however, the minimum to yield any meaningful estimate is $n = 2$. Confidence in the estimated variance increases with increasing n. Otnes and Enochsen (1978) indicate that $n = 12$ independent averages are the near minimum for reasonable spectral estimates. Thompson (1979) suggests that coherence estimates based on $n < 5$ is deceptive under most circumstances and $n > 10$ is a waste of resolution. A word of caution should be added to his comments, as they are based on the tendency for the significance levels to change with n. Change for small n tend to produce large changes in significance levels, and changes for large n tend to produce small changes in significance levels. Therefore, it is completely appropriate to use $n > 10$.

Finally, I address the fact that overlapped segments are not independent (e.g., are slightly correlated with one another) but that error statistics are analytically developed for independent segments (Carter, 1987). Although Biltoft and Pardyjak (2009) and Miller and Sigvardt (1998) argue that applying disjoint Hann windows is more appropriate than WOSA due to the non-independence. I conclude this is not good practice for three reasons. First, with WOSA there is 16 % correlation in variance of the data (Harris Semiconductor, 1997), but Nuttall (1971) explains that 92 % of maximum DOF can be achieved using WOSA. Second, recalling the Hann window reduces variance by 5/8, compared to a rectangular window, overlapping allows for the retrieval of part of the lost signal, especially for signals at longer

periods. Third, there is the potential that disjoint tapered windows may not detect certain signals if the signal occurs when the taper amplitude is zero in between the disjoint segments. (An example is found online at http://blog.prosig.com/2011/08/30/understanding-windowing-and-overlapping-analysis/).

Errors in random data are estimated using the appropriate statistical distribution to each spectral method, and these references provide background for estimating errors in random data. Townend (2002) and Bendat and Piersol (2000) provide an introduction to various statistical distributions and Von Storch and Zwiers (1999) provide an overview of various data and their distributions in geophysical studies. The error methods discussed below can be employed regardless of the method used to estimate the PSD (e.g., disjoint windows or WOSA), as long as the appropriate degrees of freedom (DOF) are used. Confidence intervals are used to estimate the uncertainty of variance in random data because the true variance in the spectral estimation is unknown. In geophysical data, confidence intervals of 95 % are typical, meaning that, there is a 5 % chance that random data will exceed or fall outside the range of the estimated variance. Significance levels of $\alpha = 0.05\,(0.01)$ correspond to a confidence interval of 95 % (99 %).

Following the guidelines summarized above, I first describe DOF. I then present and compare the various methods for computing confidence intervals for spectral methods. As there is no standard approach, commonly used texts present several options for computing confidence intervals for each of the spectral methods. Consequently, determining the appropriate method can be perplexing. I concluded that the number of averages used in PSD estimation serves as an aid in determining the appropriate method. If n is sufficiently large, one can use the random error formulas presented in Bendat and Piersol (1980) for each spectral method (i.e., PSD, FRF, phase, coherence). These methods make various simplifying assumptions that result in the narrowest confidence intervals amongst all error methods. Assuming the data are geophysical and the number of averages is not sufficiently large, then it is most appropriate to use the methods presented below.

2.2.1.7.3.1 Understanding Degrees of Freedom, Equivalent Degrees of Freedom, and Spectral Degrees of Freedom

In standard texts, DOF is often used interchangeably with spectral degrees of freedom (SDOF) but these are, in fact, different quantities. To add to this confusion, equivalent degrees of freedom (EDOF) are used when tapered spectral windows are employed as tapering inherently averages adjacent frequency bands. Rectangular windows put a fixed weight on each frequency component but tapered windows do not, they increase bandwidth and make DOF hard to determine (Von Storch and Zwiers, 1999). EDOF is an approach to infer the DOF by matching the asymptotic mean and variance of the tapered window with the mean and variance of a chi-square random variable. Koopmans (1974), Priestley (1981), and Von Storch and Zwiers (1999) provide details regarding EDOF for various tapered windows. However, because more than 90% of the stability can be achieved from using WOSA (Bendat and Piersol, 2000; Nuttall, 1971; Welch, 1967) I can approximate the DOF to be proportional to the number of averages (Shin and Hammond, 2008).

The estimation of variance depends upon the number of free components that go into its calculation, which is the number of independent observations minus 1. DOF is calculated from $DOF = (n-1)$. Because each spectral estimate is determined from $|X(f_k)|^2 = X(f_k)^2 + iX(f_k)^2$, SDOF is determined from $SDOF = 2 \cdot DOF = 2(n-1)$. This result arises because PSD is calculated from two independent squared Gaussian variables, the cosine and sine components (Bendat and Piersol, 1970). When block and frequency averaging methods are combined, DOF and SDOF are computed from $DOF = (n \cdot l) - 1$ and $SDOF = 2[(n \cdot l) - 1]$ (Otnes and Enochson, 1978).

2.2.1.7.3.2 Confidence Intervals for Power Spectral Density

The chi-squared (χ^2) distribution is used to estimate errors of squared quantities (such as variance) and, thus, is appropriate for PSD estimations. If $G_{xx}(f_k)$ is the true variance and

$\hat{G}_{xx}(f_k)$ is the estimated auto-spectrum variance, then the true variance lies in the interval $\frac{SDOF \cdot \hat{G}_{xx}(f_k)}{\chi^2_{sdof,\frac{\alpha}{2}}} \le G_{xx}(f_k) \le \frac{SDOF \cdot \hat{G}_{xx}(f_k)}{\chi^2_{sdof,1-\frac{\alpha}{2}}}$. With this method a confidence interval is computed for each frequency component and plotted with linear x-axis and log scale y-axis. A simpler approach would be to create a single confidence interval that applies to all frequencies, which must be plotted with log scale on both axes. The upper limit of the confidence interval is set by $\log(\hat{G}_{xx}) + \log\left(\frac{SDOF}{\chi^2_{sdof,\frac{\alpha}{2}}}\right)$ and the lower limit is set by $\log(\hat{G}_{xx}) + \log\left(\frac{SDOF}{\chi^2_{sdof,1-\frac{\alpha}{2}}}\right)$.

2.2.1.7.3.3 Confidence Intervals for the Frequency Response Factor and Phase Estimations

FRF error can be computed from the random error formulas mentioned above and from joint confidence intervals based on F-distributions, following Koopmans (1974) and Bendat and Piersol (1970). Errors on phase can be computed from these or by using the Student's t distribution (Koopmans, 1974).

I examined each of these methods for typical geophysical values of n (less than 30) with both fabricated (normal random data plus sinusoid with various signal to noise ratios) and observed data (along-shore wind stress and Seward Sea Level). For both cases, joint confidence intervals yield the widest intervals for both the FRF and phase. Random error methods for both FRF and phase, and Student's t for phase, depending on the signal to noise ratio, did not capture the true value of the fabricated signal, while joint confidence intervals did so quite consistently. Therefore, I employ joint confidence intervals for the FRF and phase.

The true FRF and phase lie in the interval of the estimate:

$$\left|\hat{H}(f)\right| - \hat{r}(f) \le \left|H(f)\right| \le \left|\hat{H}(f)\right| + \hat{r}(f)$$

$$\hat{\phi}(f) - \Delta\hat{\phi}(f) \le \phi(f) \le \hat{\phi}(f) + \Delta\hat{\phi}(f)$$

where $\hat{r}(f) = \sqrt{\frac{1}{SDOF} F_{n1,n2;\alpha} \left[1 - \hat{\gamma}_{xy}^2(f)\right] \frac{\hat{G}_{yy}(f)}{\hat{G}_{xx}(f)}}$

and $\Delta\hat{\phi}(f) = \sin^{-1}\left(\frac{\hat{r}(f)}{\left|\hat{H}(f)\right|}\right)$.

$F_{n1,n2,\alpha}$ is the F-distribution value found in the index of most standard texts, $n1 = 2$ is the number of DOF per spectral estimate, and $n2$ is $SDOF$.

2.2.1.7.3.4 Significance Test and Confidence Intervals for Ordinary Coherence

Coherence significance tests yield a level (between 0 and 1) above which coherence values are significant while those below this critical value are deemed insignificant. Coherence estimates below the significance level imply that estimates of the FRF and phase are meaningless.

2.2.1.7.3.5 Significance Test for Ordinary Coherence

Coherence significance levels $\left(\gamma_{1-\alpha}^2\right)$ are summarized by Thompson (1979) and computed from $\gamma_{1-\alpha}^2 = 1 - \alpha^{\frac{1}{DOF}} = 1 - \alpha^{\frac{2}{SDOF}}$. Biltoft and Pardyjak (2009) provide an example of an alternate method to calculate coherence significance levels based on F-distribution, and this method produces nearly identical results compared to Thompson's method; for $n \geq 6$ these methods are 99 % correlated.

2.2.1.7.3.6 Coherence Confidence Intervals

The Fisher "z"-transform as summarized by Koopmans (1974) and Bendat and Piersol (1970), yields the most accurate confidence intervals on coherence when $n > 20$ and $0.4 \leq \hat{\gamma}^2 \leq 0.95$. For $n \geq 20$ this method can also be used for $\hat{\gamma}^2 \leq 0.4$. Because confidence intervals become narrower, as n increases, the lower bound on the confidence interval should remain greater than zero coherence. Outside the intervals given above, this method can still be used but it is

less precise (Von Storch and Zwiers, 1999). The true coherence γ^2 lies within the intervals $\hat{\gamma}_l^2(f_k) \le \gamma^2(f_k) \le \hat{\gamma}_u^2(f_k)$. These intervals are computed as follows:

$$\hat{\gamma}_l^2(f_k) = \tanh\left(\frac{1}{2}\ln\left(\frac{1+\hat{\gamma}(f_k)}{1-\hat{\gamma}(f_k)}\right) - \frac{1}{SDOF} - \frac{Z_{\alpha/2}}{\sqrt{SDOF}}\right) \text{ and}$$

$$\hat{\gamma}_u^2(f_k) = \tanh\left(\frac{1}{2}\ln\left(\frac{1+\hat{\gamma}(f_k)}{1-\hat{\gamma}(f_k)}\right) - \frac{1}{SDOF} + \frac{Z_{\alpha/2}}{\sqrt{SDOF}}\right) \text{ where } Z_{\alpha/2} = 2.81 \text{ for } \alpha = 0.05.$$

Carter (1987) showed that these methods are valid for WOSA. He investigated if overlapping segments yielded different error approximations than those that were derived from non-overlapping segments and concluded that the confidence limits derived from overlapping segments agreed with the approximate results in Bendat and Piersol (1970), Brillinger (1975), and Otnes and Enochson (1978).

Other methods for estimating coherence confidence intervals for $\hat{\gamma}^2 \le 0.4$ may be more appropriate when $n < 20$. Zoubir (2005) did a comprehensive study for $n = 20$ and compared his bootstrap method to exact confidence intervals (Wang and Tang, 2004) and to the "z"-transform presented above. His main conclusion was that, all methods yielded similar results for high coherence, but with low coherence ($\hat{\gamma}^2 \le 0.4$) the "z"-transform broke down (lower interval below zero coherence) while the bootstrap and exact interval approach yielded similar results. Bootstrap seems to be the preferred method as it can adequately deal with very low coherence values ($\hat{\gamma}^2$ = 0.2) when $n = 20$ and is simpler to employ than Wang and Tang's (2004) method.

2.2.1.7.4 Time Series Reconstruction using the Inverse Fourier Transform

Time series data that have been transformed into frequency space using the DFT and WOSA can be transformed back into a time series using a combination of the inverse Fourier transform (IFT) and the overlap add method (OA). OA is required so there is no signal modification during

reconstruction due to the application of overlapping tapered windows during the initial spectral analysis. Considering an input and output time series that have significant coherence in frequency space, their frequency response function can be reconstructed into a time series using IFT and OA. Once the time series is reconstructed it can either stand alone to represent the relationship between the input and output or it can be subtracted from the original output time series to eliminate the contribution from the input. In Matlab, the inverse Fourier transform is accomplished through the (*ifft*) function. Allen (1977) and Allen and Rabiner (1977) describe the application of overlap-add reconstruction and an example of its use in Matlab is at http://www.coe.montana.edu/ee/rmaher/EELE477/eele477_fftlab_sp12.pdf.

2.2.1.8 Spectral Methods for Multiple Input/Single Output Analysis

It is not uncommon for a system in nature to have its signal composed of multiple sources or inputs (where the number of inputs is denoted by q). For example, sea level is simultaneously a function of tides, atmospheric pressure, winds, the annual cycle (Wunsch, 1972) and other large-scale forcing mechanisms such as the PDO (Mantua and Hare, 2002) and ENSO (Subbotina et al., 2001). The FRF, phase and coherence can also be examined in systems with multiple inputs $(q > 1)$ and a single output. The coherence between the output time series with multiple inputs can be examined by two methods, 1) each input individually, or, 2) with all inputs combined. When the inputs are examined individually the method is called partial or conditioned analysis. When the inputs are examined as a total the method is called multiple input analysis. The frequency response function for each input can be determined individually, while the frequency response function for multiple inputs is meaningless and not calculated.

When inputs are examined individually, the relationships between the inputs and output are examined when one (or more if there are more than two inputs) of the input variables are "turned off". The variable(s) that is "turned off" is removed by the equivalent of least squares techniques with the assumption that a linear relationship exists between the input and output time series. The degree to which it is turned off depends on the similarity of the other inputs signals and the signal to noise ratio between input and output data. Multiple coherence

analysis examines the contribution of all the inputs to the output time series, independent of the correlation between the inputs.

The majority of the equations presented below follow those of Bendat and Piersol (1980; 2000), though Hannan (1970) also describes multiple input methods. For many geophysical systems, the resulting signals depends on the contribution of only a few inputs; therefore, I present multiple input algorithms for $q = 2$ and $q = 3$. If more inputs are needed, the desired conditioned expression can be found by interchanging the various input and output expressions presented in the texts mentioned above. The two input/single output model is presented first and then the three input/single output method is presented. Frequency-dependence is implied for all the variables in the following equations

2.2.1.8.1 Two Input/Single Output

2.2.1.8.1.1 Two Input Frequency Response Factor and Phase

Extending the frequency response model to two inputs gives $\hat{G}_{1y} = \hat{H}_1\hat{G}_{11} + \hat{H}_2\hat{G}_{12}$ and $\hat{G}_{2y} = \hat{H}_1\hat{G}_{21} + \hat{H}_2\hat{G}_{22}$. Solving these equations for $\hat{H}_1$ and $\hat{H}_2$, yields $\hat{H}_1 = \frac{\left(\hat{G}_{1y}\hat{G}_{22} - \hat{G}_{12}\hat{G}_{21}\right)}{\left(\hat{G}_{11}\hat{G}_{22} - \hat{G}_{12}\hat{G}_{21}\right)}$ and $\hat{H}_2 = \frac{\left(\hat{G}_{11}\hat{G}_{2y} - \hat{G}_{1y}\hat{G}_{21}\right)}{\left(\hat{G}_{11}\hat{G}_{22} - \hat{G}_{12}\hat{G}_{21}\right)}$, where $\hat{H}_1$ is the FRF for input $x_1(t)$ and output $y(t)$, $\hat{H}_2$ is the FRF for input $x_2(t)$ and output $y(t)$. The phase shift between these inputs and output is given by $\hat{\phi}_1 = \tan^{-1}\left(-\frac{imag(\hat{H}_1)}{real(\hat{H}_1)}\right)$ and $\hat{\phi}_2 = \tan^{-1}\left(-\frac{imag(\hat{H}_2)}{real(\hat{H}_2)}\right)$.

2.2.1.8.1.2 Two Input Multiple Coherence

Depending on the number of inputs, the determinant $\hat{G}_{xx}$ takes the size (qxq), the determinant $\hat{G}_{y12}$ has size $(q+1xq+1)$, and $\hat{G}_{yy}$ is the auto-spectrum of the output. Two input multiple coherence is found by these expressions:

$\hat{G}_{xx}=\begin{bmatrix}\hat{G}_{11}\hat{G}_{12}\\ \hat{G}_{21}\hat{G}_{22}\end{bmatrix}$, $\hat{G}_{y12}=\begin{bmatrix}\hat{G}_{yy}\hat{G}_{y1}\hat{G}_{y2}\\ \hat{G}_{1y}\hat{G}_{11}\hat{G}_{12}\\ \hat{G}_{2y}\hat{G}_{21}\hat{G}_{22}\end{bmatrix}$, and $\hat{\gamma}^2_{y:x}=1-\left(\frac{\left|\hat{G}_{y12}\right|}{\hat{G}_{yy}\left|\hat{G}_{xx}\right|}\right)$, where $\hat{\gamma}^2_{y:x}$ is the multiple coherence between all the inputs and the output. These computations need to be made at each frequency.

2.2.1.8.1.3 Two Input Conditioned Coherence

The coherence between two input time series $x_1(t)$ and $x_2(t)$ is $\hat{\gamma}^2_{12}=\frac{\left|\hat{G}_{12}\right|^2}{\hat{G}_{11}\hat{G}_{22}}$, and the inputs are interchangeable and other coherence expressions can be found using this general expression. The coherence between $x_1(t)$ and $y(t)$ with the linear contribution of $x_2(t)$ removed from both is expressed using the notation $\hat{\gamma}^2_{1y\cdot 2}$, where $\hat{\gamma}^2_{1y\cdot 2}=\left(\frac{\left|\hat{G}_{1y\cdot 2}\right|^2}{\hat{G}_{11\cdot 2}\hat{G}_{yy\cdot 2}}\right)$, $\hat{G}_{1y\cdot 2}=\hat{G}_{1y}-\left(\frac{\hat{G}_{12}}{\hat{G}_{22}}\right)\hat{G}_{2y}$, $\hat{G}_{11\cdot 2}=\hat{G}_{11}\left(1-\hat{\gamma}^2_{12}\right)$ and $\hat{G}_{yy\cdot 2}=\hat{G}_{yy}\left(1-\hat{\gamma}^2_{y2}\right)$. Conversely, if I want to remove the contribution of input time series $x_1(t)$ from both $x_2(t)$ and $y(t)$, I use $\hat{\gamma}^2_{2y\cdot 1}=\left(\frac{\left|\hat{G}_{2y\cdot 1}\right|^2}{\hat{G}_{22\cdot 1}\hat{G}_{yy\cdot 1}}\right)$, where $\hat{G}_{2y\cdot 1}=\hat{G}_{2y}-\left(\frac{\hat{G}_{21}}{\hat{G}_{11}}\right)\hat{G}_{1y}$, $\hat{G}_{22\cdot 1}=\hat{G}_{22}\left(1-\hat{\gamma}^2_{12}\right)$ and $\hat{G}_{yy\cdot 1}=\hat{G}_{yy}\left(1-\hat{\gamma}^2_{y1}\right)$.

2.2.1.8.2 Three Input/Single Output

2.2.1.8.2.1 Three Input Frequency Response Factor and Phase

The FRF for each input is determined by solving $\hat{G}_{1y}=\hat{H}_1\hat{G}_{11}+\hat{H}_2\hat{G}_{12}+\hat{H}_3\hat{G}_{13}$, $\hat{G}_{2y}=\hat{H}_1\hat{G}_{21}+\hat{H}_2\hat{G}_{22}+\hat{H}_3\hat{G}_{23}$ and $\hat{G}_{3y}=\hat{H}_1\hat{G}_{31}+\hat{H}_2\hat{G}_{32}+\hat{H}_3\hat{G}_{33}$, for $\hat{H}_1$, $\hat{H}_2$ and $\hat{H}_3$ to yield,

$$\hat{H}_1 = \left(\frac{\hat{G}_{12}\hat{G}_{23}\hat{G}_{3y} - \hat{G}_{12}\hat{G}_{2y}\hat{G}_{33} - \hat{G}_{13}\hat{G}_{22}\hat{G}_{3y} + \hat{G}_{13}\hat{G}_{2y}\hat{G}_{32} + \hat{G}_{1y}\hat{G}_{22}\hat{G}_{33} - \hat{G}_{1y}\hat{G}_{23}\hat{G}_{32}}{\hat{G}_{11}\hat{G}_{22}\hat{G}_{33} - \hat{G}_{11}\hat{G}_{23}\hat{G}_{32} - \hat{G}_{12}\hat{G}_{21}\hat{G}_{33} + \hat{G}_{12}\hat{G}_{23}\hat{G}_{31} + \hat{G}_{13}\hat{G}_{21}\hat{G}_{32} - \hat{G}_{13}\hat{G}_{22}\hat{G}_{31}} \right),$$

$$\hat{H}_2 = \left(\frac{\hat{G}_{11}\hat{G}_{2y}\hat{G}_{33} - \hat{G}_{11}\hat{G}_{23}\hat{G}_{3y} + \hat{G}_{13}\hat{G}_{21}\hat{G}_{3y} - \hat{G}_{13}\hat{G}_{2y}\hat{G}_{31} - \hat{G}_{1y}\hat{G}_{21}\hat{G}_{33} + \hat{G}_{1y}\hat{G}_{23}\hat{G}_{31}}{\hat{G}_{11}\hat{G}_{22}\hat{G}_{33} - \hat{G}_{11}\hat{G}_{23}\hat{G}_{32} - \hat{G}_{12}\hat{G}_{21}\hat{G}_{33} + \hat{G}_{12}\hat{G}_{23}\hat{G}_{31} + \hat{G}_{13}\hat{G}_{21}\hat{G}_{32} - \hat{G}_{13}\hat{G}_{22}\hat{G}_{31}} \right), \text{ and}$$

$$\hat{H}_3 = \left(\frac{\hat{G}_{11}\hat{G}_{22}\hat{G}_{3y} - \hat{G}_{11}\hat{G}_{2y}\hat{G}_{32} - \hat{G}_{12}\hat{G}_{21}\hat{G}_{3y} + \hat{G}_{12}\hat{G}_{2y}\hat{G}_{31} + \hat{G}_{1y}\hat{G}_{21}\hat{G}_{32} - \hat{G}_{1y}\hat{G}_{22}\hat{G}_{31}}{\hat{G}_{11}\hat{G}_{22}\hat{G}_{33} - \hat{G}_{11}\hat{G}_{23}\hat{G}_{32} - \hat{G}_{12}\hat{G}_{21}\hat{G}_{33} + \hat{G}_{12}\hat{G}_{23}\hat{G}_{31} + \hat{G}_{13}\hat{G}_{21}\hat{G}_{32} - \hat{G}_{13}\hat{G}_{22}\hat{G}_{31}} \right).$$

The phase shift for each input is calculated from:

$$\hat{\phi}_1 = \tan^{-1}\left(-\frac{imag(\hat{H}_1)}{real(\hat{H}_1)} \right),$$

$$\hat{\phi}_2 = \tan^{-1}\left(-\frac{imag(\hat{H}_2)}{real(\hat{H}_2)} \right), \text{ and}$$

$$\hat{\phi}_3 = \tan^{-1}\left(-\frac{imag(\hat{H}_3)}{real(\hat{H}_3)} \right).$$

2.2.1.8.2.2 Three Input Multiple Coherence

The determinant $\hat{G}_{xxx}$ takes the size (qxq), the determinant $\hat{G}_{y123}$ takes the size $(q+1xq+1)$, and $\hat{G}_{yy}$ is the auto-spectrum of the output. The three input multiple coherence is determined from:

$$\hat{G}_{xxx} = \begin{bmatrix} \hat{G}_{11}\hat{G}_{12}\hat{G}_{13} \\ \hat{G}_{21}\hat{G}_{22}\hat{G}_{23} \\ \hat{G}_{31}\hat{G}_{32}\hat{G}_{33} \end{bmatrix}, \hat{G}_{y123} = \begin{bmatrix} \hat{G}_{yy}\hat{G}_{y1}\hat{G}_{y2}\hat{G}_{y3} \\ \hat{G}_{1y}\hat{G}_{11}\hat{G}_{12}\hat{G}_{13} \\ \hat{G}_{2y}\hat{G}_{21}\hat{G}_{22}\hat{G}_{23} \\ \hat{G}_{3y}\hat{G}_{31}\hat{G}_{32}\hat{G}_{33} \end{bmatrix},$$

$$\hat{\gamma}^2_{y:x} = 1 - \left(\frac{\left|\hat{G}_{y123}\right|}{\hat{G}_{yy}\left|\hat{G}_{xxx}\right|} \right),$$

where $\hat{G}_{xxx}$ and $\hat{G}_{y123}$ are determinants and $\hat{\gamma}^2_{y:x}$ is the multiple coherence between all the inputs and the output.

2.2.1.8.2.3 Three Input Conditioned Coherence

Three input conditioned coherence between $x_1(t)$ and $y(t)$ with linear contributions from $x_2(t)$ and $x_3(t)$ removed is $\hat{\gamma}^2_{1y\cdot 3,2} = \left(\frac{\left|\hat{G}_{1y\cdot 3,2}\right|^2}{\hat{G}_{11\cdot 3,2}\hat{G}_{yy\cdot 3,2}} \right)$,

where $\hat{G}_{1y\cdot 3,2} = \hat{G}_{1y}(1-\hat{\gamma}^2_{2y})(1-\hat{\gamma}^2_{3y\cdot 2})$,

$\hat{G}_{11\cdot 3,2} = \hat{G}_{11}(1-\hat{\gamma}^2_{2y})(1-\hat{\gamma}^2_{3y\cdot 2})$, and

$\hat{G}_{yy\cdot 3,2} = \hat{G}_{yy}(1-\hat{\gamma}^2_{2y})(1-\hat{\gamma}^2_{3y\cdot 2})$.

The coherence between $x_2(t)$ and $y(t)$ with linear contributions from $x_1(t)$ and $x_3(t)$ removed is $\hat{\gamma}^2_{2y\cdot 3,1} = \left(\frac{\left|\hat{G}_{2y\cdot 3,1}\right|^2}{\hat{G}_{22\cdot 3,1}\hat{G}_{yy\cdot 3,1}} \right)$,

where $\hat{G}_{2y\cdot 3,1} = \hat{G}_{2y}(1-\hat{\gamma}^2_{3y})(1-\hat{\gamma}^2_{1y\cdot 3})$,

$\hat{G}_{22\cdot 3,1} = \hat{G}_{22}(1-\hat{\gamma}^2_{3y})(1-\hat{\gamma}^2_{1y\cdot 3})$, and

$\hat{G}_{yy\cdot 3,1} = \hat{G}_{yy}(1-\hat{\gamma}^2_{3y})(1-\hat{\gamma}^2_{1y\cdot 3})$.

The coherence between $x_3(t)$ and $y(t)$ with linear contributions of $x_1(t)$ and $x_2(t)$ removed is

$$\hat{\gamma}^2_{3y\cdot 2,1} = \left(\frac{\left|\hat{G}_{3y\cdot 2,1}\right|^2}{\hat{G}_{33\cdot 2,1}\hat{G}_{yy\cdot 2,1}} \right),$$

where $\hat{G}_{3y\cdot 2,1} = \hat{G}_{3y}(1-\hat{\gamma}^2_{1y})(1-\hat{\gamma}^2_{2y\cdot 1})$,

$G_{33\cdot 2,1} = G_{33}(1-\gamma^2_{1y})(1-\gamma^2_{2y\cdot 1})$, and

$\hat{G}_{yy\cdot 2,1} = \hat{G}_{yy}(1-\hat{\gamma}^2_{1y})(1-\hat{\gamma}^2_{2y\cdot 1})$.

2.2.1.8.3 Error Estimations for Multiple Input Analysis

In multiple input analysis, the DOF are a function of both n and q, where $DOF=(n-q)$ and $SDOF=2(n-q)$. Error estimation for the frequency response factor and phase in a system with multiple inputs is calculated using joint confidence intervals similar to those presented for single input methods described in section 2.2.1.7.3.3. Assuming time series $x_i(t)$ is of interest, the multiple input FRF uncertainty $\hat{r}_i(f)$ is found using

$$\hat{r}_i(f)=\sqrt{\frac{1}{SDOF}F_{n1,n2;\alpha}\frac{\left[1-\hat{\gamma}^2_{y:x}(f)\right]}{\left[1-\hat{\gamma}^2_{x_i:x\cdot x_i}(f)\right]}\frac{\hat{G}_{yy}(f)}{\hat{G}_{x_ix_i}(f)}},$$

where $n1=2q$, $n2$ is $SDOF$, and $\gamma^2_{y:x}$ is the multiple coherence between all inputs and the output. The term $\gamma^2_{x_i:x\cdot x_i}$ is the multiple coherence between the input x_i and the other inputs excluding x_i, $\hat{G}_{x_ix_i}$ is the auto-spectrum of the input, and $\hat{G}_{yy}$ is the auto-spectrum of the output. Coherence confidence intervals and significance levels are calculated with the same methods as above with the appropriate n and q.

3 Results and Discussion

3.1 Tidal Influence

Tides in the ocean are caused by the gravitational attraction of the sun and moon on the ocean. Tides, at all timescales, are one of the few variables in the ocean that can be predicted with confidence. Tides are cyclic, with the main cycles occurring on the time scales of: annual, semi-annual (half-annual), monthly, fortnightly (two-weekly), diurnal (daily), and semi-diurnal (twice -daily). The annual and semi-annual tidal cycles will not be discussed further. Compound tides (harmonic constituents) result from nonlinear interactions in shallow water areas and may vary regionally based on local bathymetry and the amplitudes of the diurnal and semi-diurnal tides. All tides with periods less than 2 days are compound tides. In this section, I simply highlight the tidal influence on SSL and do not undertake a detailed tidal analysis.

Tides are the dominant and highest frequency (>1 cpd) component of coastal GOA sea level, and they account for more than 97 % of the sea level variance at Seward, Yakutat and Sitka. Tidal ranges in sea level vary from 1 to 5 m daily (Figure 8 and Figure 9). Figure 4 shows the SSL tidal energy spectrum with a fundamental period (time length of data record) of one year. This tidal spectrum is similar to that for Yakutat and Sitka.

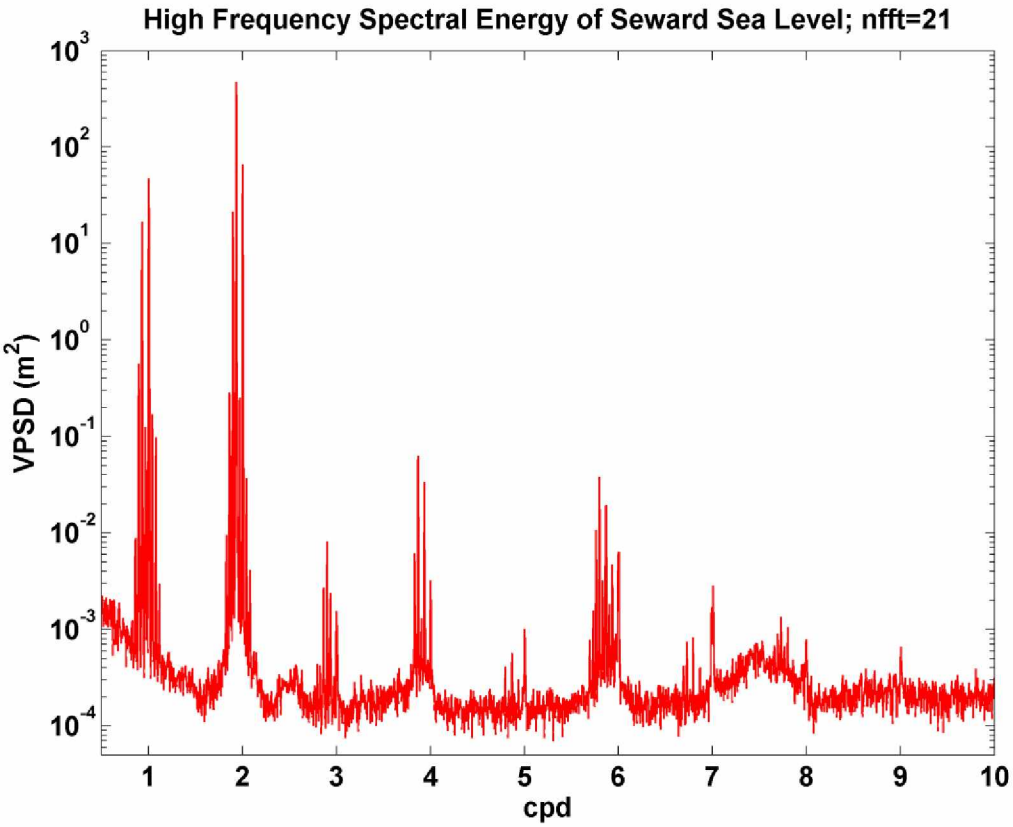

Figure 4. Power spectral energy of SSL tidal constituents for frequencies greater than ~ 1cpd.

Several tidal signals are apparent near each integer value of the number of cycles per day (cpd), up to 9 cpd. To highlight this I show the diurnal and semi-diurnal band in greater detail. The tidal analysis software t_tide (Pawlowicz, 2002) was utilized in examining these high frequency tidal signals. For the diurnal band (Figure 5), the three largest constituents are the K_1, O_1 and P_1; of the semi-diurnal band (Figure 6), the three largest constituents are the M_2, S_2 and N_2. GOA tides are of the mixed type with the dominant constituent of M_2 (12.42 hour period) and second dominant K_1 (23.93 hour period). Note that only one year of data was used for the identification of the diurnal and semi-diurnal tidal constituents using t_tide in Figure 5 and Figure 6 (blue and red lines), while the tidal signal itself (black line) was generated using a fundamental period of four years.

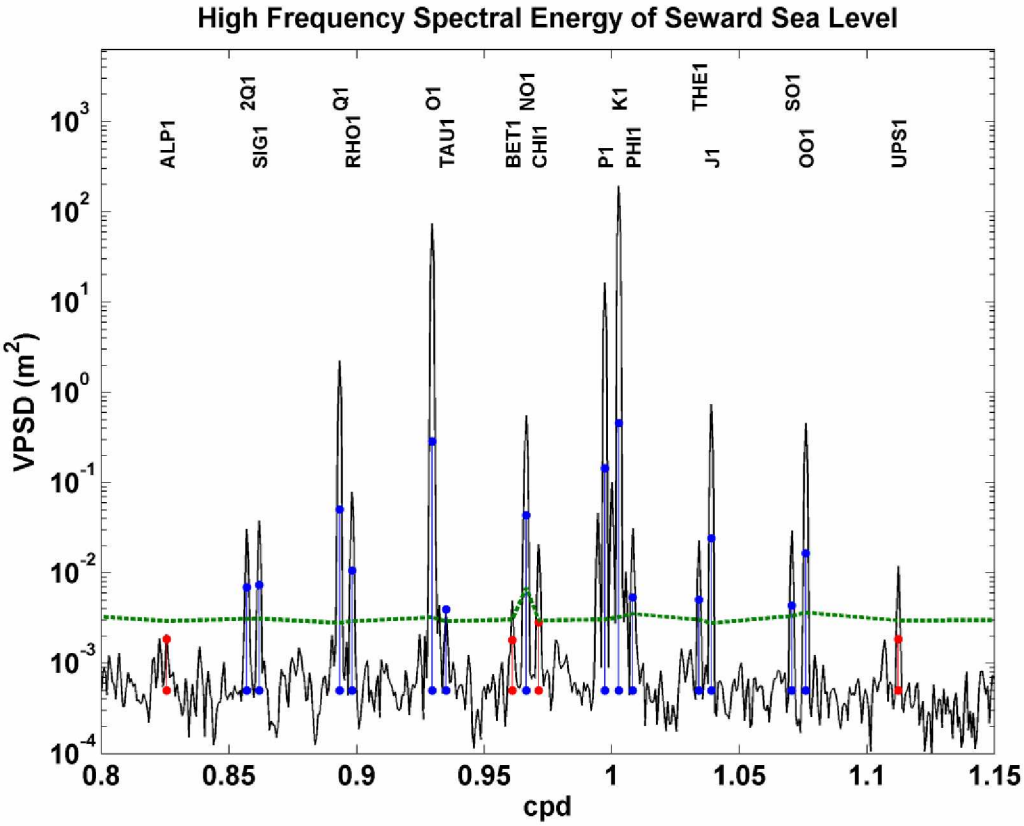

Figure 5. Tidal constituents at the diurnal band. Blue (red) lines indicate tidal constituents that exceed (do not exceed) 95 % confidence. The green line represents 95 % significance level.

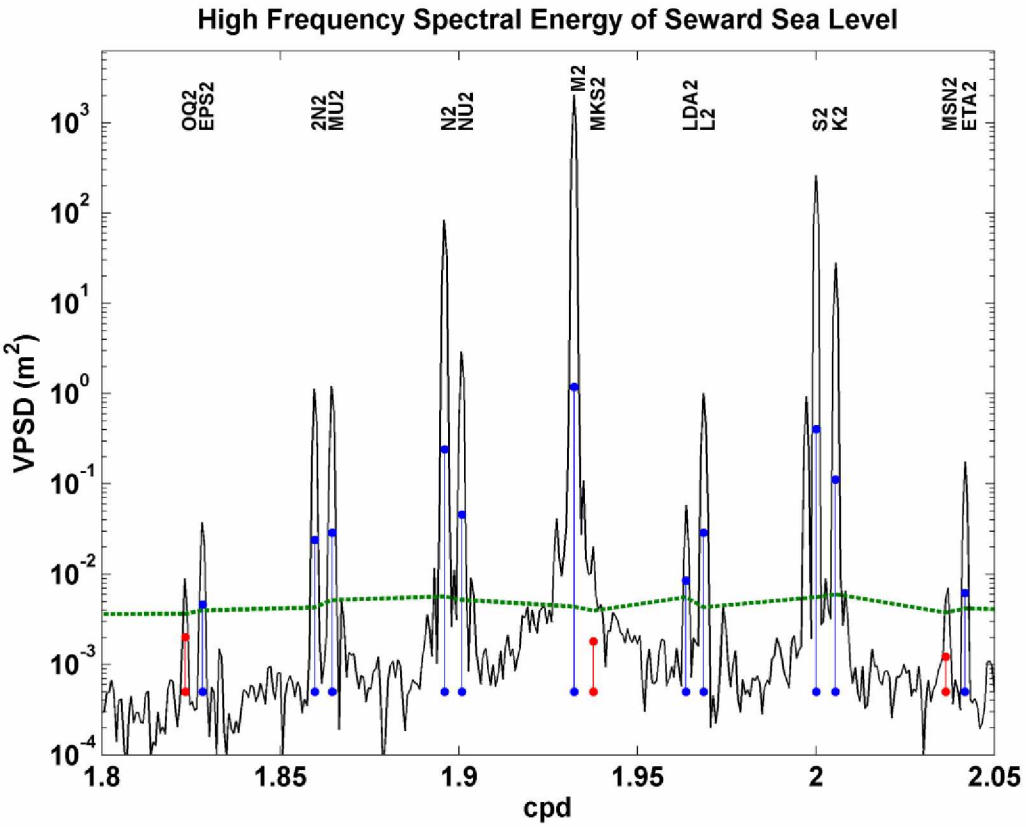

Figure 6. Tidal constituents at the semi-diurnal band. Blue (red) lines indicate tidal constituents that exceed (do not exceed) 95 % confidence. The green line represents 95 % significance level.

I first attempted to remove the high frequency tidal components of SSL by using t_tide, but this method has several limitations. First, it does not sufficiently remove high frequency signals (> 1cpd). Second, it can only examine data in yearly intervals; therefore, long record lengths require extra computation time and programming. Third, it was unable to remove the fortnightly, or one month lunar tide as the signal to noise ratios for these constituents were too low to be removed with statistical reliability. Ultimately, I removed the high frequency tides with a 38 hr 8^{th} order Butterworth filter. This cutoff period was chosen in order to completely eliminate the diurnal tide while not affecting the signal at periods > 2 days, because my interest is in sub-tidal sea level variations.

The fortnightly (or monthly) constituent was not removed from the sea level data; however, the fortnightly constituent proved to be highly useful as a spectral reference. On the other hand, the inability to remove the fortnightly tide results in the coherences between SSL and other parameters being low in the neighborhood of the fortnightly period (13.66 days), while high with sea level at other locations.

3.2 The Influence of Sea Level Pressure

SLP is highly variable in the GOA due to the continual passage of atmospheric pressure systems across the region. Variations in SLP create variations in sea level because of the inverse barometer effect. This influence varies seasonally. SLP is at its annual maximum in the summer (specifically, June and July), which is also when SLP variance is minimal. SLP is at its minimum in the winter (specifically, December and January) when the SLP variance is highest. Spectral analysis indicates that the majority of SLP energy lies between the 3 and 60 day periods and maximum SLP energy occurs at the ~18 day period. In winter (summer) peak spectral SLP energy is in the 20-30 (10-20) day period range, and winter months contain 4.7 times more spectral energy than summer months (Figure 7). The reason the spectral peaks occur at different periods seasonally is most likely because of the persistence of the AL in the winter months. Because low pressure is most common in the winter, high pressure less frequently interrupts the low pressure compared to the summer months when low pressure systems interrupt high pressure systems more frequently. This would lead to the maximum in variance to be at longer (shorter) periods in the winter (summer). In June and July, the correlation between monthly averages of SLP and SSL is r^2 ~0.6, while in the other months r^2 is ~0.7 - 0.8.

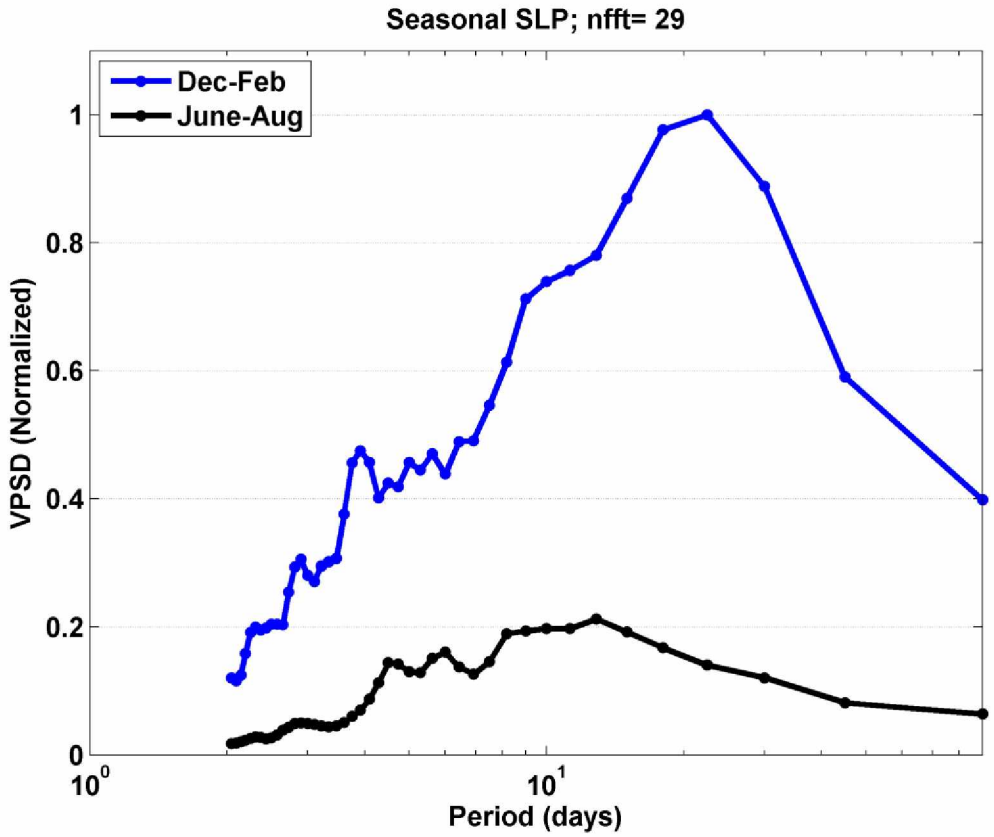

Figure 7. A seasonal view of power spectral energy of sea level pressure at Middleton Island, AK.

The coherence between SLP and low pass filtered SSL is consistently $\geq$ 0.7, although for periods of 2 to 10 days the coherence is $\geq$ 0.8. Coherence is also high (~0.8) for periods of up to two year periods. Consequently, the SLP influence on sea level is broadband.

The inverted barometer effect produces changes in local sea level because of local atmospheric pressure changes. The barometric factor (b.f.) of -1.01 cm mb^{-1} is generally accepted as the response of sea level due to SLP, although it can often deviate from this. Trupin and Wahr (1990) examined various global locations to find a range in b.f. from -0.97 to -1.6 cm mb^{-1}. I examined the b.f. using spectral methods described by Hamon (1966). The b.f. was consistently less than ~-1.10 cm mb^{-1}, with an average value of ~-1.19 cm mb^{-1} and less than ~-1.30 cm mb^{-1} for periods greater than 50 days. I found no seasonal difference in the b.f.

After correcting for the inverted barometer effect using ~-1.007cm mb^{-1}, computed from the methods below, there was still small but significant coherence between SLP and SSL. This may be due to underestimating the influence of SLP on sea level, although Wunsch (1991) notes that wind and SLP are often strongly correlated. Hence, the correlation between SLP and sea level may simply reflect the sea level response to wind, which coincides with a real but misleading correlation between SLP and sea level. The inverted barometer-corrected (IBC) sea level $SL_{IBC}(t)$ is given by:

$$SL_{IBC}(t) = SL(t) + \nabla\eta(t)$$

where $SL(t)$ is observed sea level. The term $\nabla\eta(t)$ is the local sea level change due to SLP and is calculated by $\nabla\eta(t) = \frac{SLP(t) - \overline{SLP}}{\rho g}$, where $SLP(t)$ is observed SLP, $\overline{SLP}$ is the mean local SLP, ρ the average water column density (1028 kg m^{-3}) , and g is gravity. SLP accounts for around 2 % of the total variance of raw SSL, which is small compared to the tidal contribution to sea level variance. Indeed, the influence of SLP on sea level is only apparent when viewing the time series after the tidal signal has been removed.

3.3 GOA Sea Level Temporal Variability

The influence of high frequency tides and the inverse barometer dominate GOA sea level variability. This is evident by examining plots of the raw, detided, and IBC sea level. Figure 8 (upper panel) is a two month segment of raw SSL. Figure 8 (bottom panel) is the inverse barometer response to detided SSL. Figure 9 shows a 2-year time series segment of raw, detided, and IBC SSL.

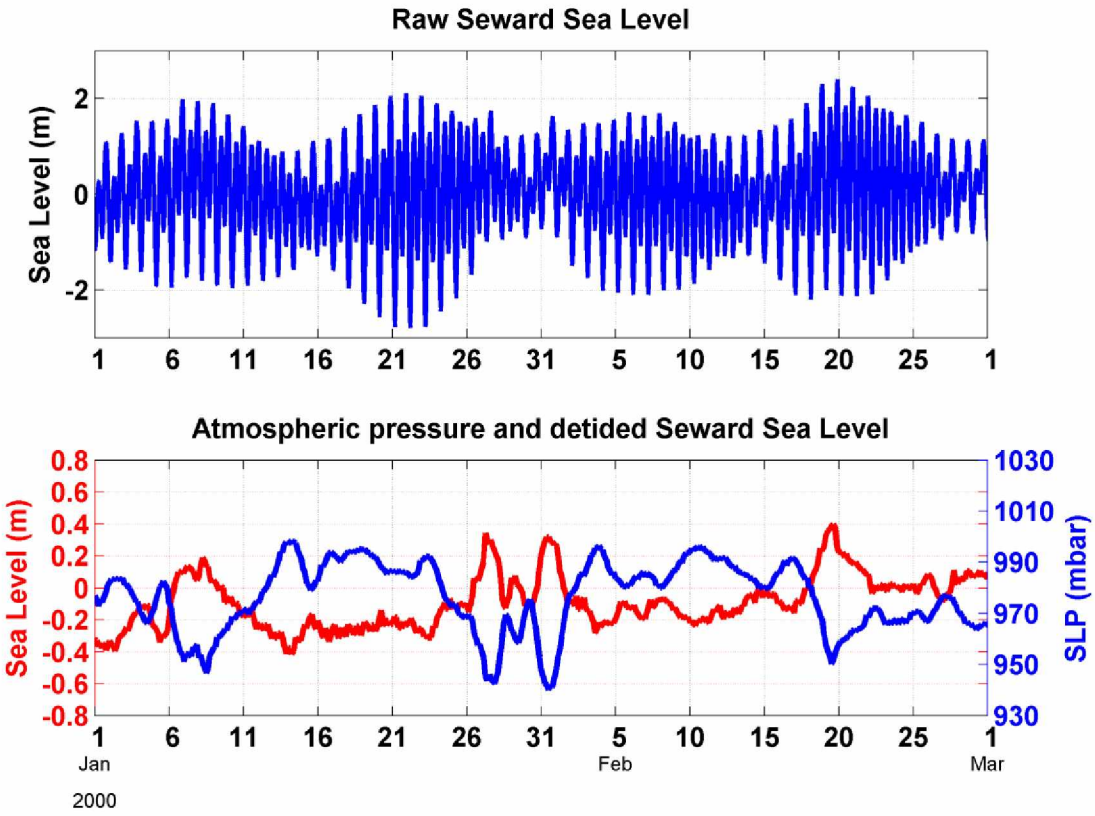

Figure 8. A two month segment of SSL. Upper panel: raw SSL; lower panel: the inverse response of SSL to sea level pressure (SLP) after tides have been filtered from the time series.

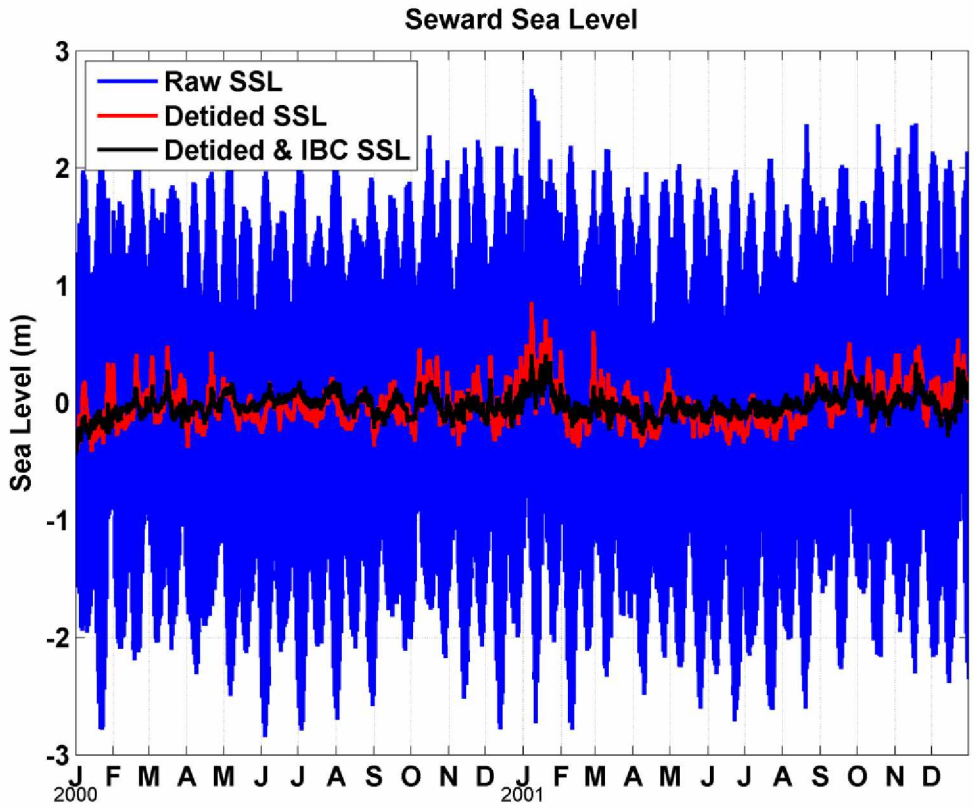

Figure 9. SSL shown before and after tidal and inverse barometer correction.

After removing the tides and applying the IBC, SSL variance has been reduced by ~99 %, hence the subtidal, IBC sea level of interest in the remainder of this thesis accounts for only 1 % of the total sea level variance. Hereafter, and unless otherwise noted, all sea level records have been low pass filtered with the IBC applied.

The remaining variability in the GOA sea level record is due to low frequency tides, winds, shelf waves, hydrographic influences, freshwater discharge, and climatic variations. Though each of these signals is embedded in the sea level record, some are more obvious than others. This is evident in normalized (VSPD) spectral energy of SitSL (Figure 10) normalized to the maximum value of the fortnightly tidal signal. I used SitSL as it had the longest continuous sea level record (1980-2011) available. However, the spectral energy distribution of both Seward and Yakutat is

similar to that of Sitka sea level. In Figure 10, the low frequency fortnightly and monthly tides are at ~13 and 28 days, respectively. These tides have been widely studied and are not examined further here. The influence of wind on sea level spans periods from a few days to the annual.

As a result of the passing of low pressure systems, and their associated winds, shelf waves are likely generated at a multitude of timescales. One possible shelf wave candidate is evident in the spectral signal at ~9 days. This signal is clearly present in the Sitka (Figure 10) and Yakutat sea level power spectra, but it is not well defined in the SSL spectra. This could be due to the fact that the propagation velocity of these waves is highly dependent upon shelf width and wave energy scattering due to coastline features. For example, the shelf width at Yakutat and Sitka is narrower than the width west of Yakutat. Coherence analysis suggests high coherence in GOA sea level at periods of 9-11 days; however, this is not proof in and of itself since GOA sea levels are coherent across a broad range of periods.

The annual cycle is also evident in the power spectra. There also are influences at longer time scales, but the fundamental period in Figure 10 is 5 years, which is not long enough to resolve climatic influences such as ENSO or decadal variations. These time scales are examined later using other methods. All of the spectral signals discussed above are examined in the remainder of this thesis.

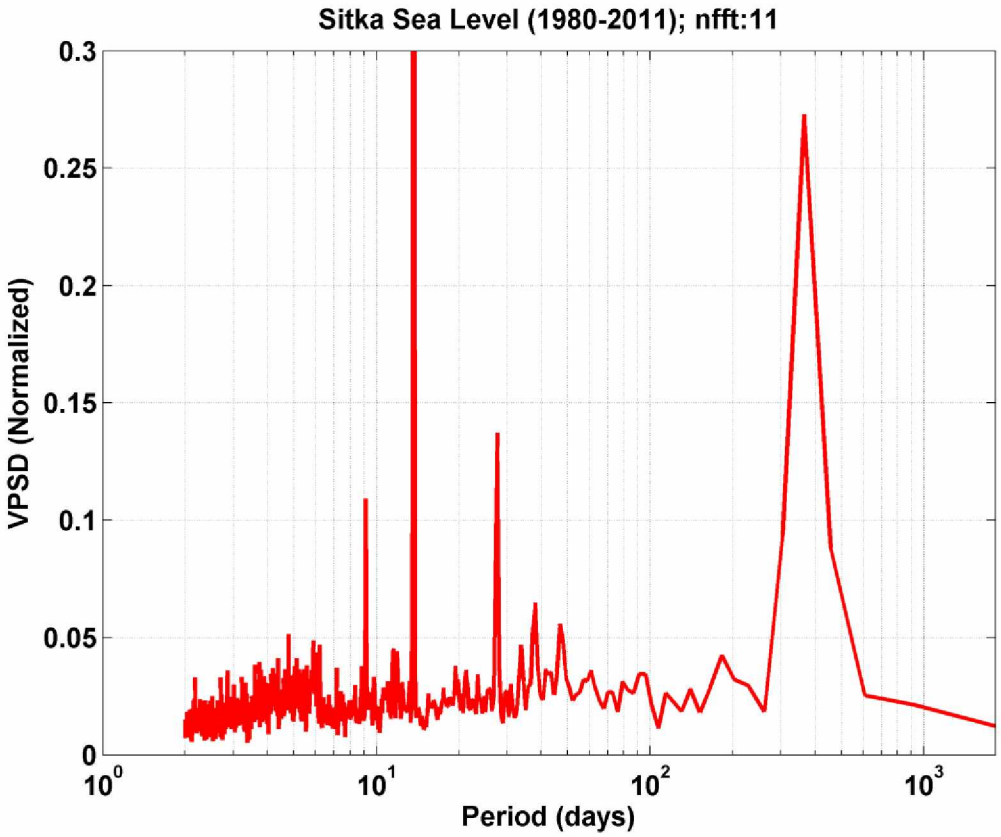

Figure 10. Spectral energy of Sitka sea level for the time period of 1980-2010. Values are normalized (to 1) to the maximum of the signal at the fortnightly period. Here the fundamental period is 5 years.

Sea level fluctuations are seasonally variable (Figure 11). For example, in the 2-90 day period range, the winter season contains 4.3 times more energy than summer. In the next section I examine the role of wind on SSL.

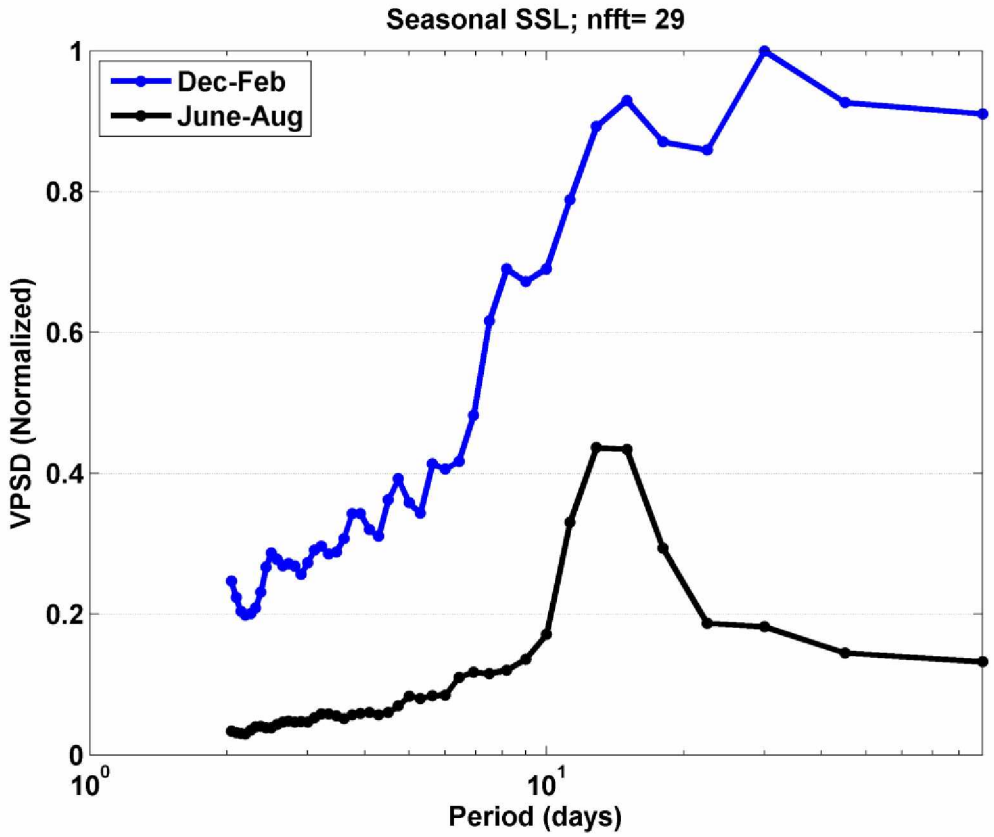

Figure 11. Seasonal spectral power of Seward sea level; winter contains 4.3 times more energy than summer.

3.4 The Role of Wind Stress

A knowledge of the nature of the wind stress field is essential to the understanding of oceanic and shelf circulation. This is especially true in GOA where ocean circulation is strongly coupled to the winds (Livingstone and Royer, 1980; Royer, 2005). This shelf is subject to predominantly downwelling winds associated the cyclonic motion of the Aleutian Low, which, based on the alongshore (U) -wind component at Middleton Island, has an integral time scale of 4-5 days. The observed winds from Middleton Island indicate that the alongshore winds are mainly westward, or downwelling favorable, while the cross-shore (V) wind component is mostly northward. ASWS and CSWS have the same pattern for Yakutat and Sitka.

In addition to the regional wind field, coastal waters are subject to intensified local wind fields, including barrier jets and gap winds (Macklin et al., 1988). These arise from interactions between the coastal mountains and atmospheric pressure gradients that steer winds to produce these mesoscale wind phenomena. Data from wind models, such as the NARR model used here, do not fully capture the spatial or temporal variability of these wind events, which may play a substantial role in influencing local sea level variations. I nevertheless, assume that the general circulation of the re-analyzed wind is representative of the regional wind field.

3.4.1 Periods less than the Annual Cycle

I examined the relationship (1970-2010) of SSL to winds at various NCEP locations that lie east of Seward (described in the data section). This relationship was explored through time-domain correlation analyses using daily U and V wind anomalies, lagged from 0-4 days, at several locations with SSL. These analyses, not presented here, generally yielded low ($r^2 < 0.2$) correlations that were largely insignificant. In general, time domain comparisons of wind and SSL did not yield insights on the response of sea level to wind forcing.

Frequency domain analyses, such as spectral and coherence analysis, were more powerful tools for examining the role of wind stress on SSL. My spectral analytical approach was similar to those used by Schwing (1989), Sokolova et al. (1992), Park and Watts (2005), and Ryan and Noble (2006).

I examined the coherence of SSL with the rotated ASWS and CSWS at Seward, Middleton Island, Yakutat and Sitka. Wind stress at those locations is represented by: τ_{Sew} , τ_{MI} , τ_{Yak} and τ_{Sit} . However, τ_{Sew} yielded lower coherence than winds from Middleton Island, and so the results using τ_{Sew} are not presented. Of interest is that τ_{MI}^{a} (where the superscript "a" ("c") indicates the along-shore (cross-shore) wind stress component) has the largest overall coherence with SSL (Figure 12). The strength of this relationship may be because the NARR re-analyzed winds assimilate Middleton Island observations, and thus, may be the most accurate representations of the shelf wind field. For example, using 3-hourly data from 1997, the NARR grid location

chosen to represent winds from Middleton explains 81 % of the variance in the observed Middleton Island winds.

At periods longer than ~ 30 days, CSWS from Sitka has higher coherence with SSL than cross-shore winds from Seward or Yakutat. However cross-shore winds at Yakutat have higher coherence with SSL, at all periods, than cross-shore winds at Seward. Unless noted otherwise, τ^a_{MI} and τ^c_{MI} (ASWS and CSWS) will be solely utilized in the following spectral and coherence analyses.

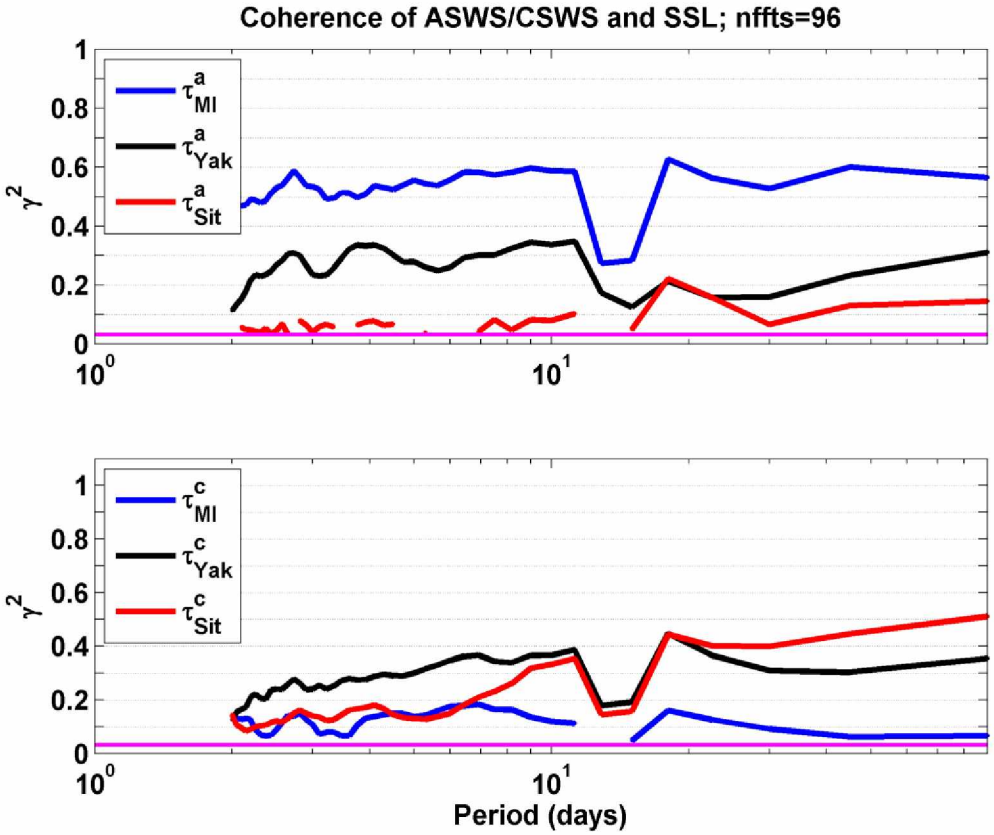

Figure 12. Top panel: the coherence between along-shore wind stress at (τ^a_{MI}) at Middleton Island, Yakutat (τ^a_{Yak}), and (τ^a_{Sit}) and SSL. Bottom panel: the coherence between cross-shore winds (τ^c) at these locations with SSL. The magenta line represents the 5 % significance level on each plot.

Wind stress spectra show that the majority of wind energy occurs for periods less than 20 days. On average, τ_{MI}^{a} contains ~4 times more energy than τ_{MI}^{c} and both components have spectral peaks in the 2-5 day period (Figure 13). Winter τ_{MI}^{a} contains 8.3 times more energy than summer τ_{MI}^{a}; the spectral peak in winter τ_{MI}^{a} occurs around the 2-6 day period, while summer energy is more broadly distributed across the 2-12 day period band (Figure 14).

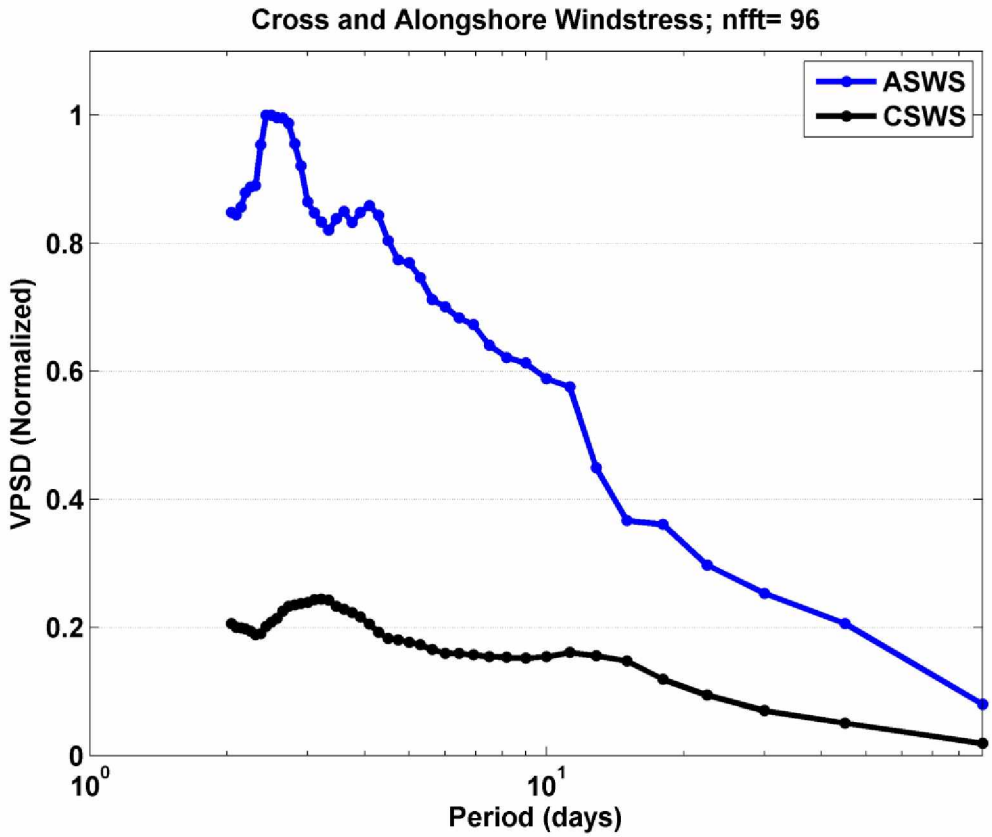

Figure 13. Spectral energy of along-shore (τ_{MI}^{a}) and cross-shore (τ_{MI}^{c}) wind stress at Middleton Is., AK.

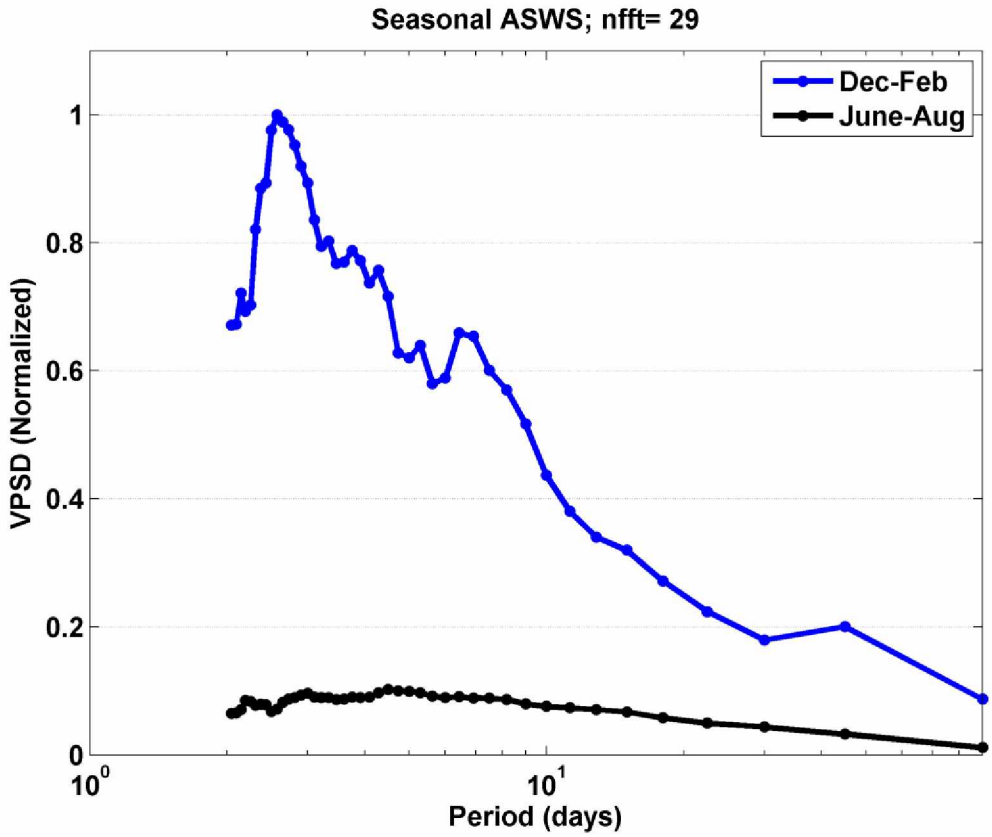

Figure 14. Power spectral energy of seasonal τ_{MI}^{a} .

Csanady (1981) showed that alongshore wind has greater influence than cross-shore winds in forcing sea level variations. I expect this to hold for the GOA based on dynamic considerations (Ekman transport from along-shore winds due to the Coriolis force) and especially because ASWS has more energy than CSWS. To examine this further, I use two-input multiple and conditioned coherence, with τ_{MI}^{a} and τ_{MI}^{c} as inputs and SSL as output (Figure 15). On average, the multiple coherence of wind with SSL ranges between 0.5 and 0.65. As expected, the partial coherence reveals that τ_{MI}^{c} has a weaker relationship with SSL than τ_{MI}^{a} . The partial coherence of τ_{MI}^{c} and SSL are only significant for periods of ~2-40 days, and the partial coherence coefficient ranges between 0.1 to 0.2 for those time scales that are significant. The partial coherence of τ_{MI}^{a} and SSL has a relatively constant value of 0.5 across the spectrum, except for

longer periods (> 40 days) where it is 0.6. The efficiency of onshore Ekman transport originating from along-shore winds, and the dominant energy of those winds, both contribute to the high coherence between τ^{a}_{MI} and SSL. Negative phase indicates that SSL lags wind stress.

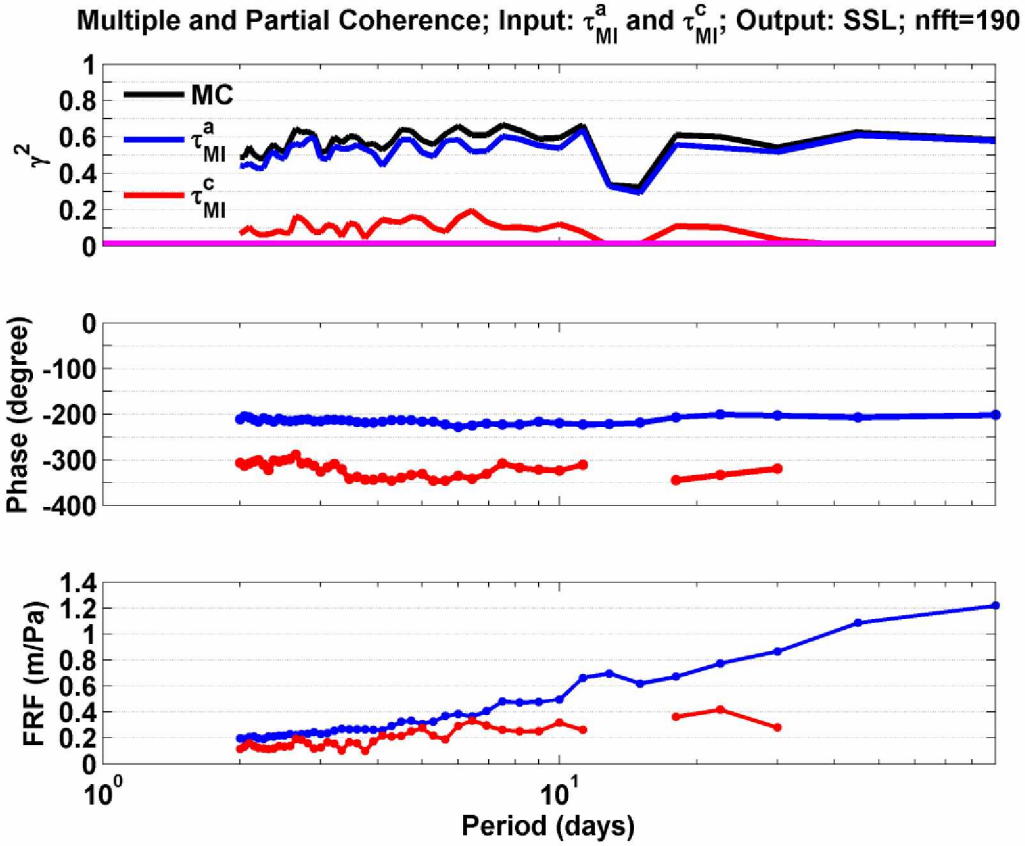

Figure 15. Top panel: multiple (MC; black) and partial coherence with inputs of τ^{a}_{MI} (blue) and τ^{c}_{MI} (red) and SSL as output. Middle panel: Phase relationship between SSL and the wind stresses. Negative phase indicates that SSL lags wind stress. Bottom panel: FRF between SSL and the wind stresses. The magenta line represents the 5 % significance level.

Even though most of the wind energy lies in periods ≤ 30 days, wind forcing at longer periods is also very important. This is because the response of sea level response to wind stress increases with increasing period, and is largest at the longest periods. This is seen in the conditioned

frequency response functions (FRF) shown in Figure 15 and Figure 16. In Figure 16, the conditioned FRF is plotted against the log of the period (in days), which illustrates the linearity between these variables. As easily seen in Figure 15, the FRF values of τ_{MI}^{a} and SSL increase six-fold from periods of 2 to 90 days, with the FRF at 2 (90) days being ~0.2 (1.2) m Pa^{-1}. The maximum FRF values between τ_{MI}^{c} and SSL occurs in the 20-30 day period range, but these values are half that of the FRF between τ_{MI}^{a} and SSL over the same period band.

The linear correlation between the conditioned FRF (of τ_{MI}^{a} and SSL) and log(period) is $r^2 = 0.96$, whereas the linear correlation between the conditioned FRF (of τ_{MI}^{c} and SSL) and log of the log(period) is $r^2 = 0.74$ (Figure 16). The slope of the conditioned FRF vs. log(period) is different for each wind component. I estimate the ASWS slope to be 0.61 m $(Pa\ day)^{-1}$, and the CSWS slope to be 0.23 m $(Pa\ day)^{-1}$. For the FRF of τ_{MI}^{a} and SSL the slope is relatively flat in the 2 - 4 day period range, but increases and is constant for periods of > 5 days. The slope of the FRF of τ_{MI}^{c} and SSL is relatively uniform across the spectrum. The slope of the FRF of τ_{MI}^{a} and SSL is ~ 3 times greater than the slope of the FRF of τ_{MI}^{c} and SSL.

Ryan and Noble (2006) examined the FRF relationship between wind and sea level at three locations along the Pacific coast (Neah Bay, WA, San Francisco, CA, and Los Angeles, CA) for periods between 3-60 days for Neah Bay and San Francisco and 6-60 days at Los Angeles; each location had a different FRF and associated slope. The slope was estimated using least squares analysis. At the 60 day period, they found the FRF to be ~0.96, 0.67 and 0.89 m Pa^{-1} (respectively). Within the GOA, I found the FRF value (between τ_{MI}^{a} and SSL) to be ~1.13 m Pa^{-1} at the same period and greater than those along the west coast of the US. Ryan and Noble (2006) estimated the slope to be ~0.72, 0.4, and 0.86 m $(Pa\ day)^{-1}$, but did not analyze CSWS. It is not clear why the FRF increases with increasing period, although one explanation could be that other sea level forcing mechanisms decrease in importance with increasing period.

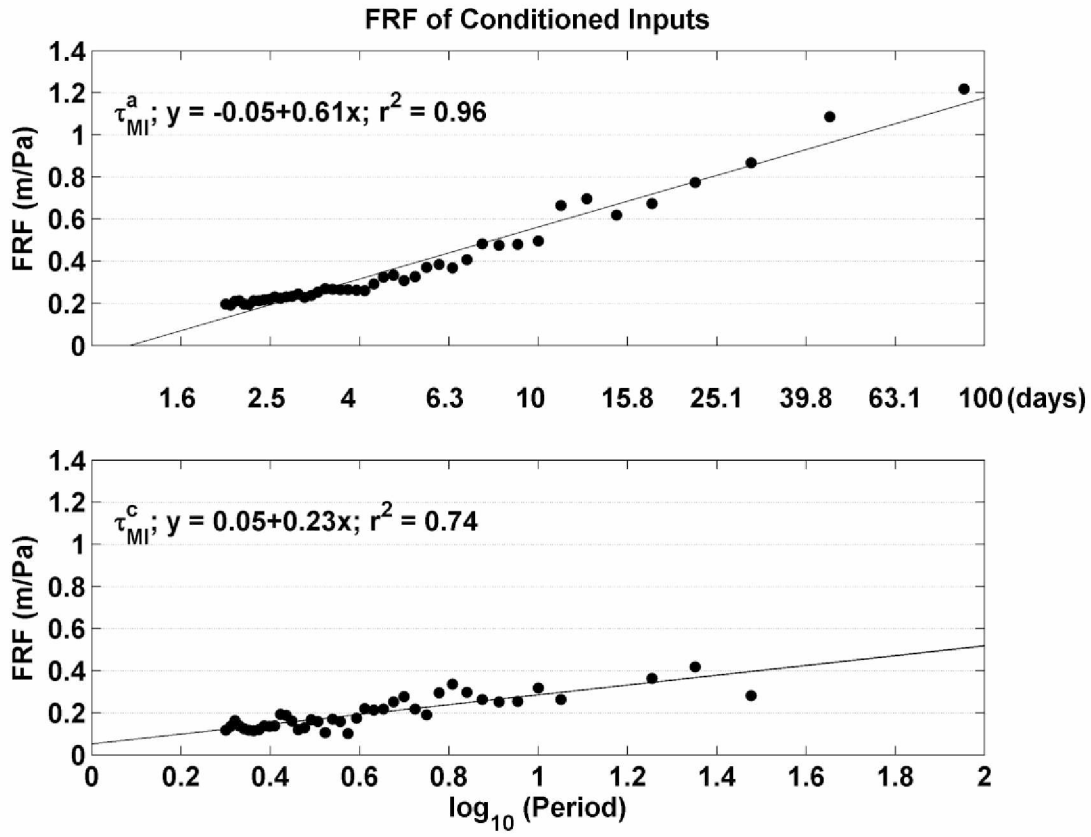

Figure 16. Linear regression results between the FRF of τ^a_{MI} and τ^c_{MI} and $\log_{10}$(period). The fundamental period is 90 days.

It is useful to contrast the seasonal difference of wind forcing on SSL by examining the two-input multiple coherence, with τ^a_{MI} and τ^c_{MI} as inputs and SSL as the output (Figure 17). Coherence in winter is greater than in summer, especially for periods less than 20 days. The multiple coherence of winds and SSL in the winter season exceeds 0.7 for periods between 2 and 3 days and is consistently $\geq$ 0.6 for periods greater than 3 days. In summer, the 2 day period multiple coherence is $\leq$ 0.2, increases to a maximum of ~0.6 by the 20 day period, and then decreases to 0.4 by the 90 day period.

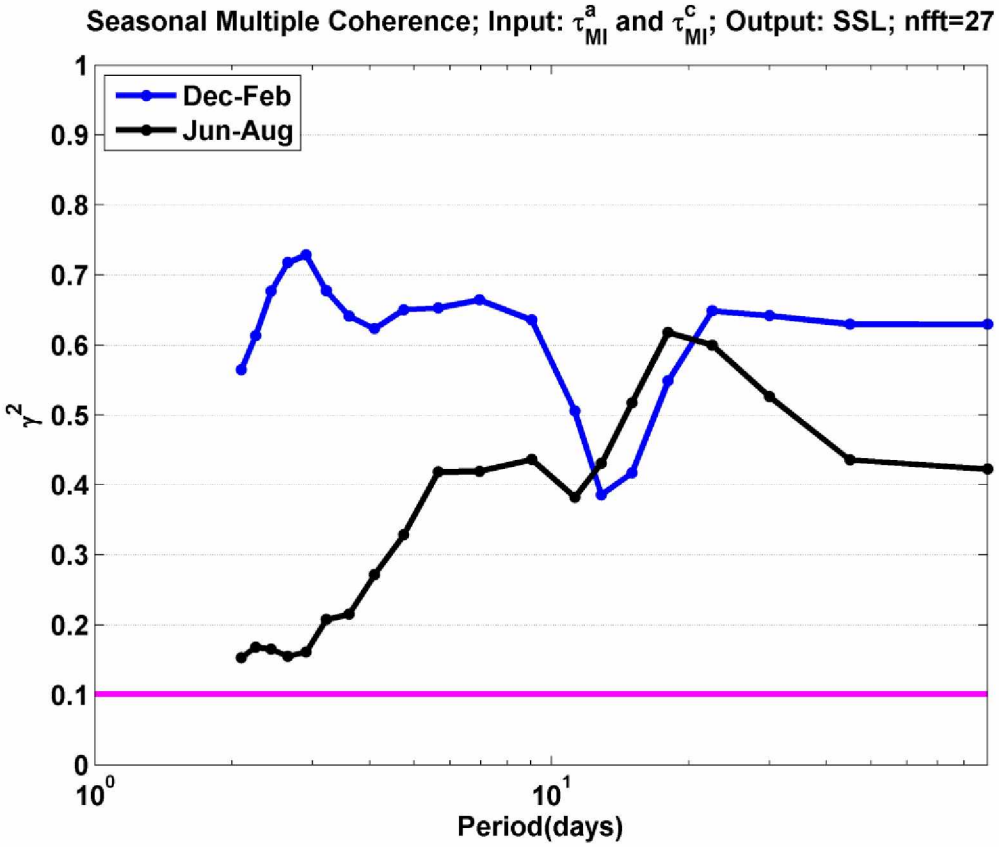

Figure 17. Seasonal multiple coherence with inputs of τ^a_{MI} and τ^c_{MI} and SSL as output. Winter (summer) shown in blue (black). The magenta line represents the 5 % significance level.

To emphasize the overall importance of atmospheric forcing on raw sea level, I used three input multiple coherence analysis with the input variables of SLP, τ^a_{MI} and τ^c_{MI}, and the output variable being detided non-IBC SSL. There is high coherence in both seasons. Atmospheric forcing in the winter is highly coherent with SSL for periods greater than 2 days where the multiple coherence ranges between 0.9 and 0.95. Multiple coherence in the summer is high also; for periods 2 to 4 days the coherence ranges from 0.6-0.8, while for periods greater than 4 days it is consistently above 0.8 across the spectrum (Figure 18).

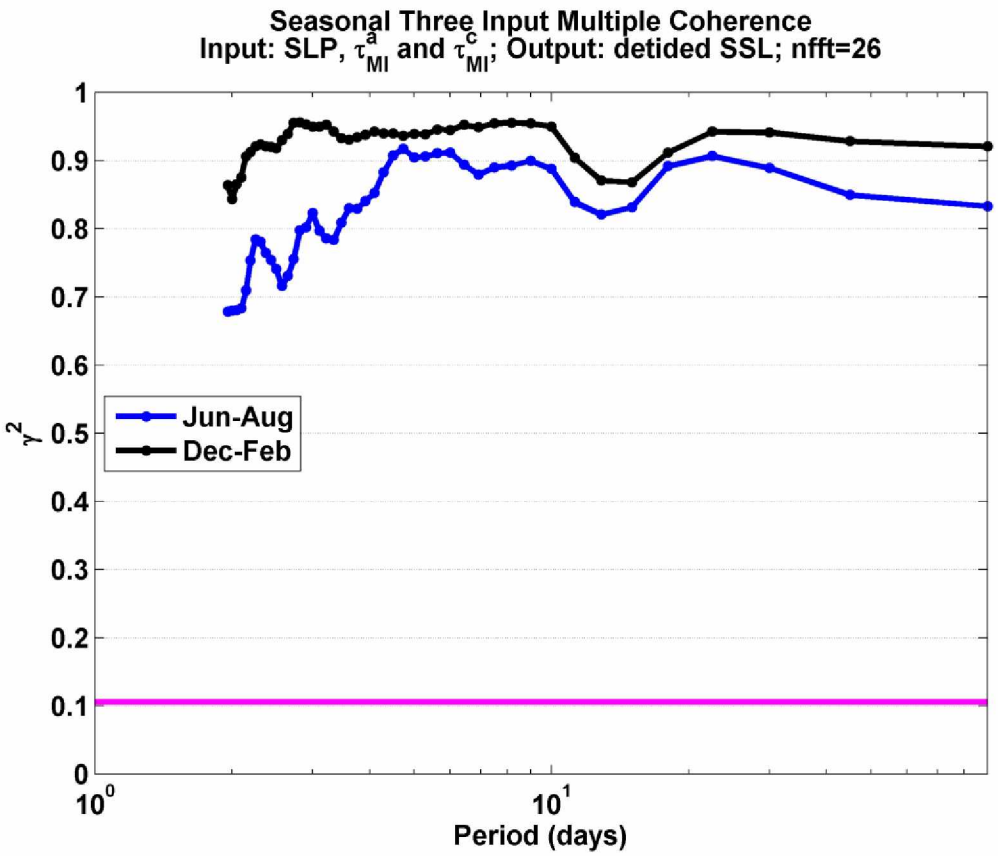

Figure 18. Seasonal three input multiple coherence with inputs of SLP, τ^a_{MI} and τ^c_{MI} and detided non-IBC SSL as output. The magenta line represents the 5 % significance level.

3.4.2 Inter-Annual Variability and the Annual Cycle

The timing and variance of the annual cycle of τ^a_{MI} corresponds to that of SLP; the weakest and least variable winds occur in summer and the strongest and most variable winds occur in winter as seen by the monthly averages of τ^a_{MI} (Figure 19) for the 1980-2011 period. This climatological depiction indicates a well-defined annual cycle in ASWS, with maximum (downwelling) stress in December-January and minimum stress in June-August. However, ASWS has high inter-annual variability, and a well-defined annual cycle is not reflected in any particular year. This is most likely because of random temporal and spatial variability in cyclogenesis, storm-track trajectory and velocity, and the strength of the AL.

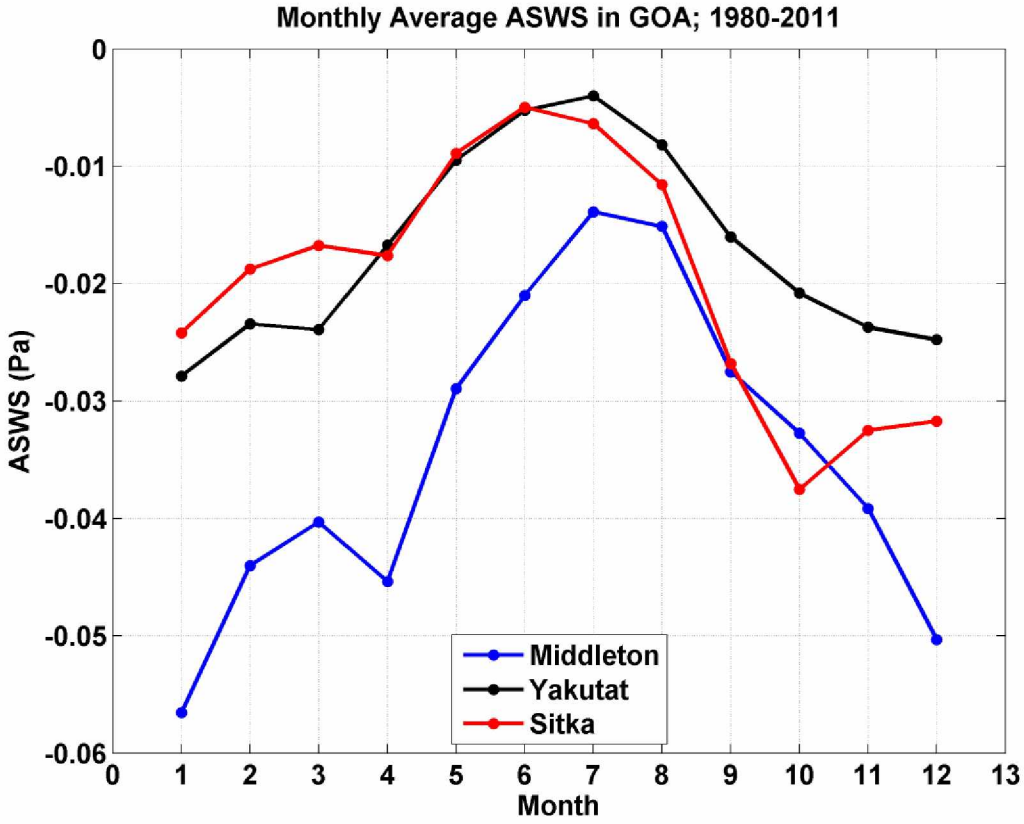

Figure 19. Monthly average of τ^{a}_{MI} (along-shore wind stress - ASWS) near Seward, Yakutat and Sitka from 1980-2011.

To examine the inter-annual variability of the annual cycle of ASWS, I performed sinusoidal least squares fits at the annual period of year-long time series segments. These regressions were performed with data corresponding to the years when mooring data are available, and as shown later (section 3.6.4.), < 3 % of the ASWS variance can be explained by fitting to an annual cycle in any given year. Hence, a statistically significant annual cycle evident in the climatological ASWS is not present in any particular year.

To examine the annual cycle of wind in a climatological sense (at Middleton Island), daily averages of CSWS and ASWS were computed for the period of 1980-2010. The general trend of the daily averages of τ_{MI}^{c} suggests there is little seasonal change in magnitude, and that wind blows mostly on-shore, rather than off-shore (figure not shown). However, τ_{MI}^{a} undergoes large seasonal changes in magnitude, with summer values being smaller than winter. An annual sinusoidal fit to the daily averages of τ_{MI}^{a} explains 40 % of the variance with the maximum downwelling wind stress occurring ~January 22nd. The daily averages (smoothed by 45 days) of τ_{MI}^{a} are shown in Figure 32.

3.5 Along-shore Coherence in Sea Level in the GOA

In order to understand the coherence of sea level in GOA, I computed the coherence between Seward (SSL) and Yakutat (YakSL), and Seward and Sitka (SitSL), where Seward is the output variable in each case. Yakutat is located ~550 km east of Seward, and Sitka and Yakutat are separated by ~400 km, so that the along shore distance between Seward and Sitka is ~950 km. The coherence results are shown in Figure 20.

Sea level coherence is small, but significant, at periods <6 days and this is likely due to local variations in wind and hydrographic forcing. At periods >10 days the coherence is >0.5 and is ~0.8 at the annual period. Sea level coherence between Yakutat and Seward is higher than Sitka and Seward, although the differences are not large.

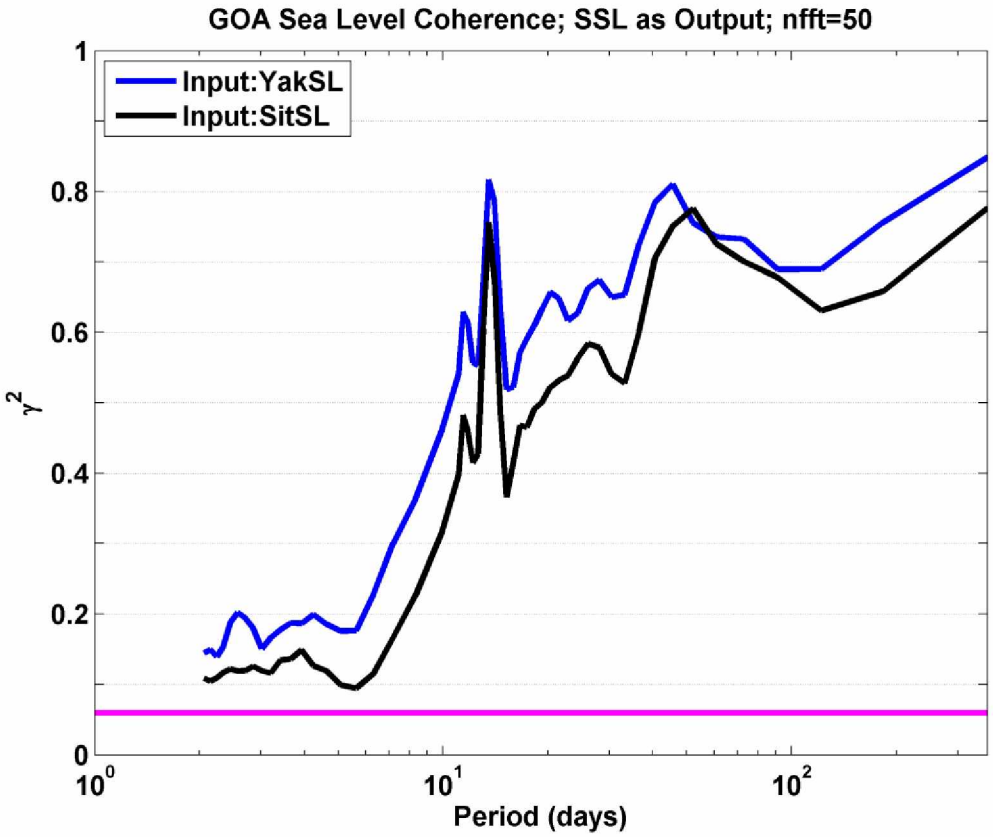

Figure 20. Coherence between Seward and Yakutat, and Seward and Sitka with Seward as the output in both cases; the fundamental period is 365 days. The magenta line represents the 5 % significance level.

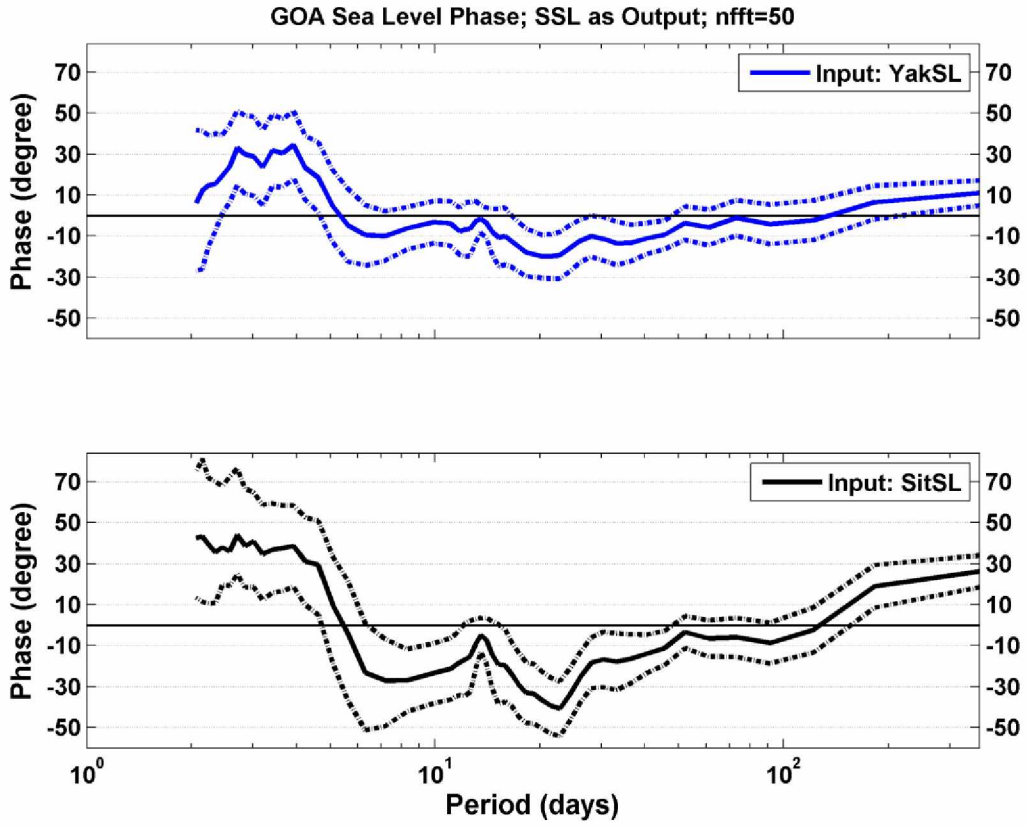

Figure 21. Negative phase indicates that the phase of SSL lags. Frequency averaging was used to smooth the signal at short periods. The blue (black) lines are the phase between SSL and Yakutat (Sitka). The fundamental period is 365 days. Dashed lines are 95 % confidence intervals.

The phase information indicates that signal propagation around the coastal GOA is frequency dependent (Figure 21). Negative (positive) phase indicates SSL lags (leads), which can be interpreted as a counterclockwise (clockwise) propagation of signal around the GOA coast. In general, the phase lag between Sitka and Seward is more often significantly different from zero due to its distance from Seward, than the phase difference between Yakutat and Seward.

There are three distinct regions, or cases, corresponding to different temporal forcing mechanisms. The first covers $\leq$ ~5-6 days, the second is for periods from ~6 -110 days, and the third is at the annual cycle. I will use the word "tend" to describe the phase estimate itself, which does not include where the error bars lie. However, in each case, the phase estimate is significantly different from zero in each distinct spectral region.

In the first case, the phase result indicates that the signal tends to propagate clockwise. This most likely represents a direct forced response of sea level to storms as they initially travel eastward across the GOA. This effectively results in Seward feeling the storm earlier than either Yakutat or Sitka. Storms typically propagate across the GOA at 12 m s^{-1} (Mesquita et al., 2010) and thus take ~8 hours to transit from Seward and Yakutat. The phase difference in sea level between these two locations is about 30 degrees at the 3-day period implying that the SSL response leads the YakSL response by ~6 hours.

In the second case, the phase spectrum indicates a counterclockwise propagation of the signal. I hypothesize this is a sea level response arising from forcing from winds (and storms) that generate continental and coastally trapped waves that propagate counterclockwise with the coast on the right, traveling from the east to the west. Chelton and Davis (1982) note that wind stress is one to two orders of magnitude more important at generating these types of shelf waves than SLP alone.

At the annual cycle, the phase information suggests that sea level propagates clockwise, or that SSL reaches its maximum sooner than the other locations. The phase spectra suggest that SSL reaches its annual maximum ~11 days before Yakutat and ~27 days before Sitka. This finding is discussed further in the next section.

3.5.1 Sea Level at the Annual Cycle

At the annual cycle, sea level is nearly in-phase around the GOA as apparent in Figure 22, which shows the mean monthly sea level at each station computed from 1970 to 2010. In general,

month-to-month sea level changes coincide, although there are noticeable differences in late summer and fall. For example, while all stations have minimum sea level in May, SSL rapidly increases thereafter and attains its annual maximum in October. In contrast, Yakutat and Sitka appear to reach their annual maximum in November or December. Note also that sea level increases nearly linearly with time at a rate of ~0.02 - 0.03 m month^{-1} between May and October at both Seward and Yakutat. However, the rate of increase at Sitka is initially much slower (~0.01 m month^{-1}). These differences could be due to differences in the along-shore wind regime around the GOA. In general, the frequency of occurrence and strength of downwelling-favorable winds is greater during the summer months at Seward and Yakutat than at Sitka. In particular, upwelling events are more common along southeast Alaska in summer than over the northern GOA shelf (Weingartner et al., 2008).

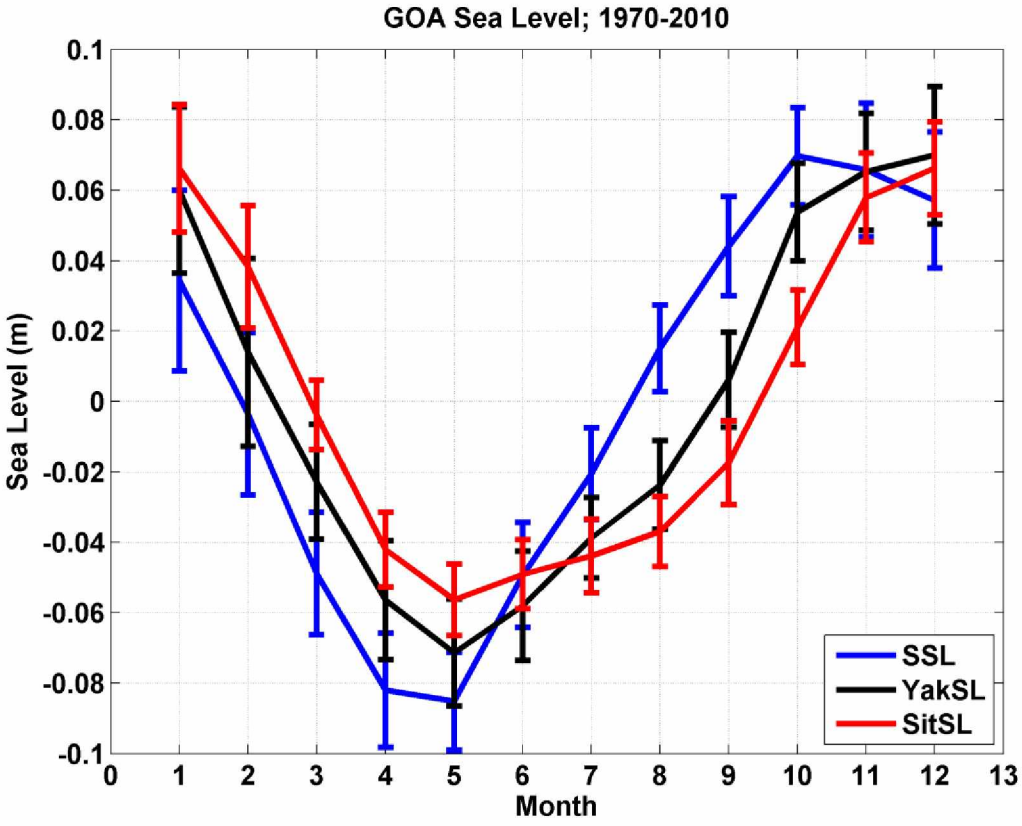

Figure 22. GOA sea level monthly average from 1970-2010.

Statistically, SSL is different than SitSL for 7 out of 12 months, while SSL is different from YakSL for 2 out of 12 months, and YakSL is different from SitSL in only 1 month. For SSL the maximum occurs between October-November, for Yakutat it occurs between November-December, and for SitSL it occurs around December-January. All locations reach their minimum in May after a similar rate of decrease from January to April. As sea level begins to rise from its minimum, after May, SSL experiences the highest rate of increase, SitSL has the lowest rate, and the rate of YakSL rise is between that of the other stations. Reed and Schumacher (1981) also examined sea level at these same locations, and surprisingly, made similar conclusions about the timing of the annual cycle, though with much less statistical confidence. They hypothesized this to be due to a difference in baroclinic and barotropic forcing, where the latter mostly controls Yakutat and Sitka.

3.6 GAK1 Hydrography and its relation to GOA parameters

The local water column responds to forcing from tides, winds, freshwater discharge and changes in hydrography, with each of these affecting it at different time scales. In this section I explore the relation of each of these parameters at various time scales. Without local water column data from Yakutat and Sitka, I cannot make definitive conclusions regarding the influence of hydrography in those areas; however, I will assume that the basic seasonal hydrographic cycle at these locations is similar to that at GAK1. I begin this section by examining the hydrography based on the GAK1 mooring at periods shorter than the annual cycle.

3.6.1 Periods less than the Annual Cycle

High frequency tides are detectable in the raw GH200 time series but they were removed using the same low pass filter as described earlier. I examined the longer period tides and found that the fortnightly (two week period) is not distinguishable while the one month lunar tide is the dominant signal in the spectra (besides the annual cycle).

I also examined the coherence of τ_{MI}^{a} and GAK1 hydrography, which includes temperature, salinity, and GH (at various depths of integration). Coherence is insignificant between τ_{MI}^{a} and temperature (at depths of 25, 100 and 200 m). The coherence between τ_{MI}^{a} and salinity is low. However, the vertical salinity variations are not generally coherent; for example, salinity at 25 m is not coherent with salinity at 100 or 200 m, and the coherence between salinity at 100 and 200 m is low. Of the hydrographic variables, I find the highest coherence between τ_{MI}^{a} and GH; with coherence increasing with increasing depth of the integration. ASWS is most coherent with GH200. I therefore examine GH200 in further detail.

To understand how the water column (GH200) is affected by τ_{MI}^{a} , and how the water column and sea level are related, I computed the coherence between each of these variables. Coherence levels are generally similar between SSL and GH200, and between τ_{MI}^{a} and GH200 (Figure 23). In both cases the coherence ranges between ~0.2 and ~0.4 for periods of 4-30 days. This similarity in coherence arises because SSL and GH200 are mutually coherent with ASWS, as will be shown below. The phase indicates that GH200 leads SSL and that GH200 lags τ_{MI}^{a} .

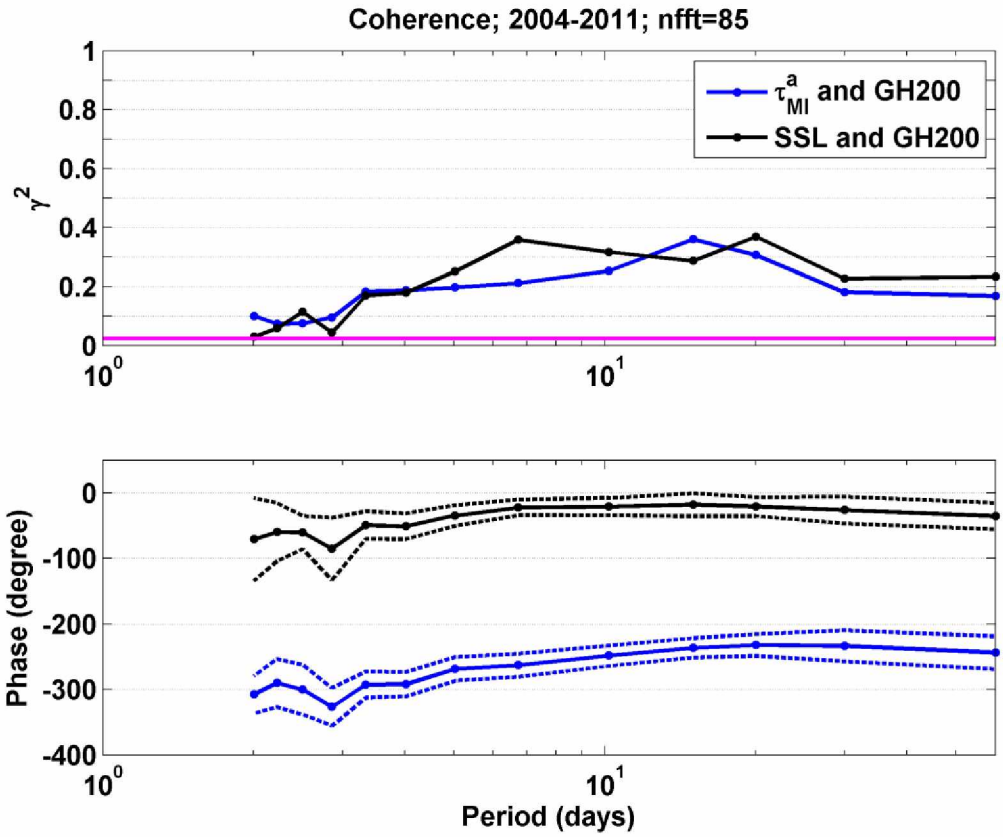

Figure 23. Single input coherence between the variables SSL, τ^a_{MI}, and GH200; GH200 is the output variable in both cases. Negative phase indicates that GH200 lags SSL and τ^a_{MI}. The magenta line represents the 5 % significance level. Dashed line indicates 95 % confidence.

What is not clear at this point is how SSL and GH200 respond differently to wind. For a better understanding of the interaction of these variables, it may be helpful to plot the phase (and coherence) between τ^a_{MI} and GH200 and between τ^a_{MI} and SSL (Figure 24). For periods from 8-40 days their phases are statistically indistinguishable; however, for periods less than 8 days, as well as for periods of 50-60 days, the phases are significantly different from one another. Note that the phase of τ^a_{MI} and GH200 lags the phase of τ^a_{MI} and SSL. This is because SSL reflects both a barotropic and baroclinic response to the along-shelf winds, whereas the slower response of GH200 is primarily due to baroclinic re-organization of the shelf. The baroclinic response is

always slower than the barotropic response. In aggregate, Figure 23 and Figure 24 suggest a subtly complicated interaction among these variables.

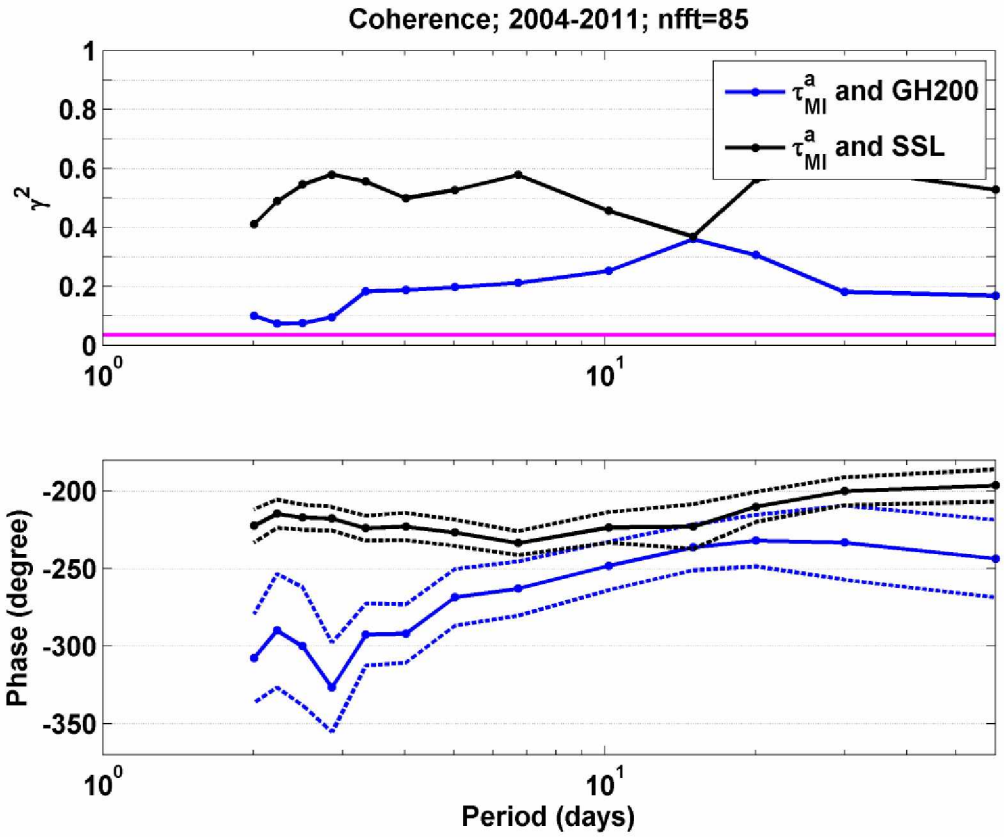

Figure 24. Single input coherence and phase between τ^a_{MI} and GH200 and between τ^a_{MI} and SSL. Negative phase indicates τ^a_{MI} leads GH200 and SSL. The magenta line represents the 5 % significance level. Dashed line indicates 95 % confidence.

I used two input coherence analysis with inputs of τ^a_{MI} and GH200 and SSL as the output (Figure 25) to separate the influence of each of these inputs on SSL and to compare these results to the single input analysis presented in Figure 23 and Figure 24. Multiple coherence is ~0.6 for periods $\geq$ 3 days. The partial coherence between τ^a_{MI} and SSL ranges between 0.4 and 0.5, whereas the partial coherence of GH200 and SSL is zero for periods $\leq$ 3 days, and a

maximum of ~0.15 for periods of 6-20 days. The low partial coherence over the 10-20 period day range is most likely due to the fortnightly tide in the SSL record.

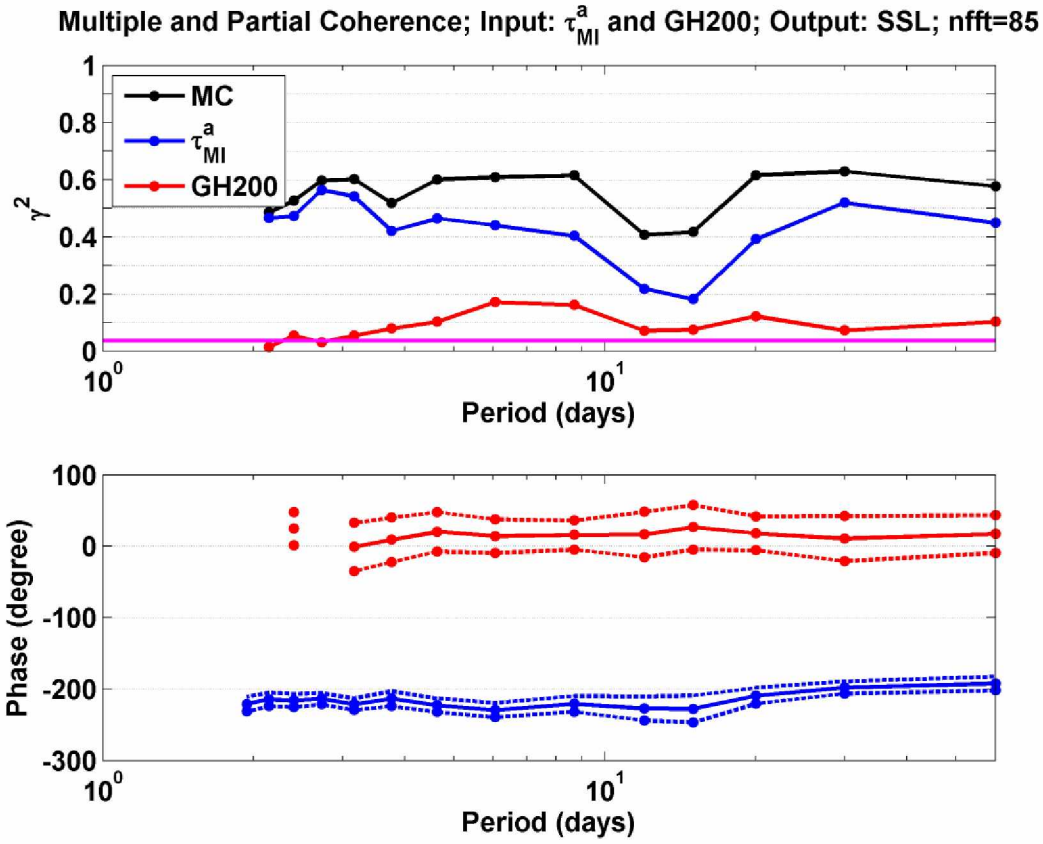

Figure 25. Multiple (MC) and partial coherence (upper) and phase (lower) with inputs of τ^x_{MI} and GH200, and SSL as output. The magenta line represents the 5 % significance level. Dashed line indicates 95 % confidence.

These calculations indicate that GH200 and SSL are in phase and that τ^a_{MI} leads SSL (Figure 25, bottom). This phase information highlights that SSL reflects both a barotropic and baroclinic response originating from along-shelf winds. The barotropic response of SSL arises from cross-shelf Ekman transport resulting in the accumulation of water along the coast. The baroclinic response of sea level arises as the salinity (density) distribution of the water column is reorganized by cross- and along-shelf transports. The dominance of the barotropic response is

evident from the small difference between the multiple and partial coherence of ASWS and SSL. The small partial coherence between GH and SSL indicates that the baroclinic influence at these time scales is small.

To better understand how the vertical salinity distribution of the water column is affected by winds I examined the seasonal response of GH200 to ASWS. On a seasonal basis, differences in wind energy, runoff, and air sea heat fluxes will govern the seasonality of GH. In winter the ocean is cooling and runoff is low, while the frequency of storms and the wind stress are high. In summer surface heating and runoff increase, while the storm frequency and intensity weakens. Ultimately, strong winter winds have a greater effect on changing GH through vertical advection compared to the summer months when buoyant surface water is abundant and the water column is heavily stratified (Figure 26). The coherence between τ^{a}_{MI} and GH200 in the winter is higher compared with summer at shorter periods (e.g. < 5 days), while at longer periods the coherence is similar between summer and winter. The phases are not statistically different between seasons (figure not shown). The FRF's for each season are significantly different for periods < 10 days. Because of greater wind energy in winter, the FRF in winter is ~7 to 2 times greater that of summer for periods 3-60 days.

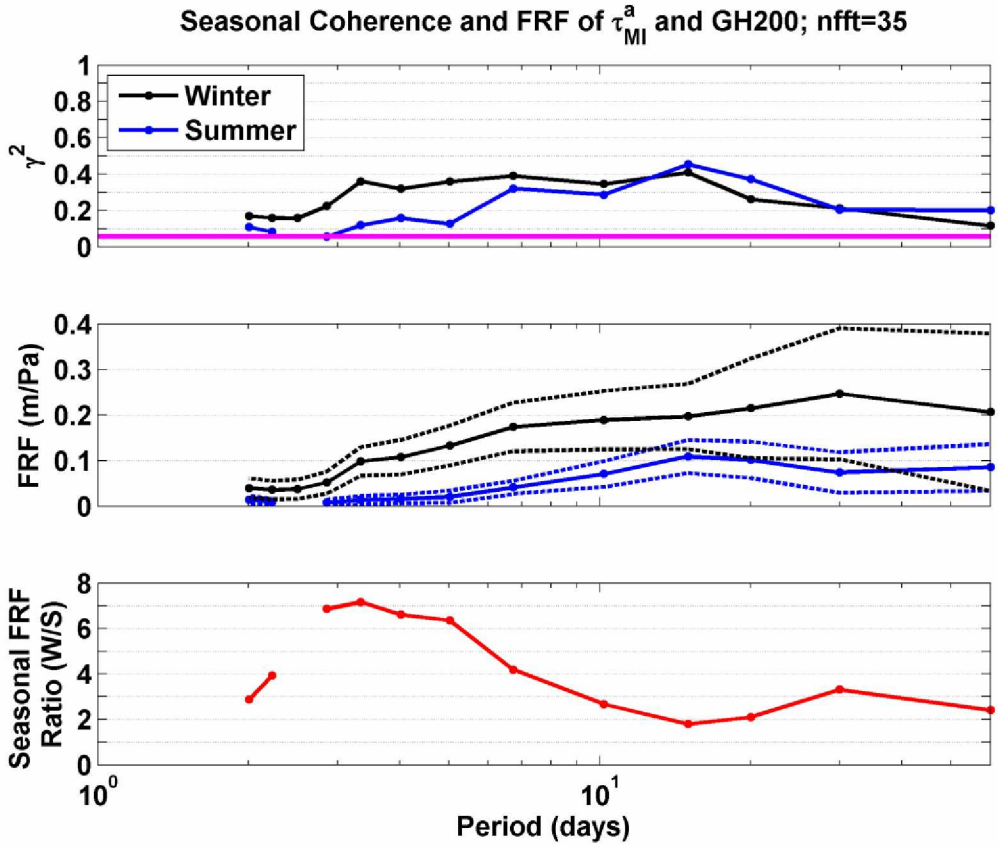

Figure 26. Top panel: Seasonal coherence between τ^a_{MI} and GH200, winter (summer) shown in black (blue). The magenta line represents the 5 % significance level. Middle panel: The seasonal frequency response function (FRF). Dashed line indicates 95 % confidence. Bottom panel: Seasonal FRF ratio of winter/summer shown in red.

3.6.2 Hydrography at the Annual Cycle

Using monthly averages I examined the annual relationship between SSL and GH. The correlation of these variables depends upon depth of integration from which GH is computed. To understand this relationship, I used both historic data (1980-2010) and more recent cast data (1997-2011) for computing GH. Historic GAK1 data are organized into standard depths of 0, 10, 20, 30, 50, 75, 100, 150, 200 and 250 m, and the recent casts data were subsampled into 5 m intervals from surface to bottom. There is effectively no difference in these methods, the strongest correlation (r^2 ~ 90 %) occurs when GH is referenced to between 200 and 250 m (Figure 27). This result supports the choice of using GH200 for comparisons with SSL at the annual cycle.

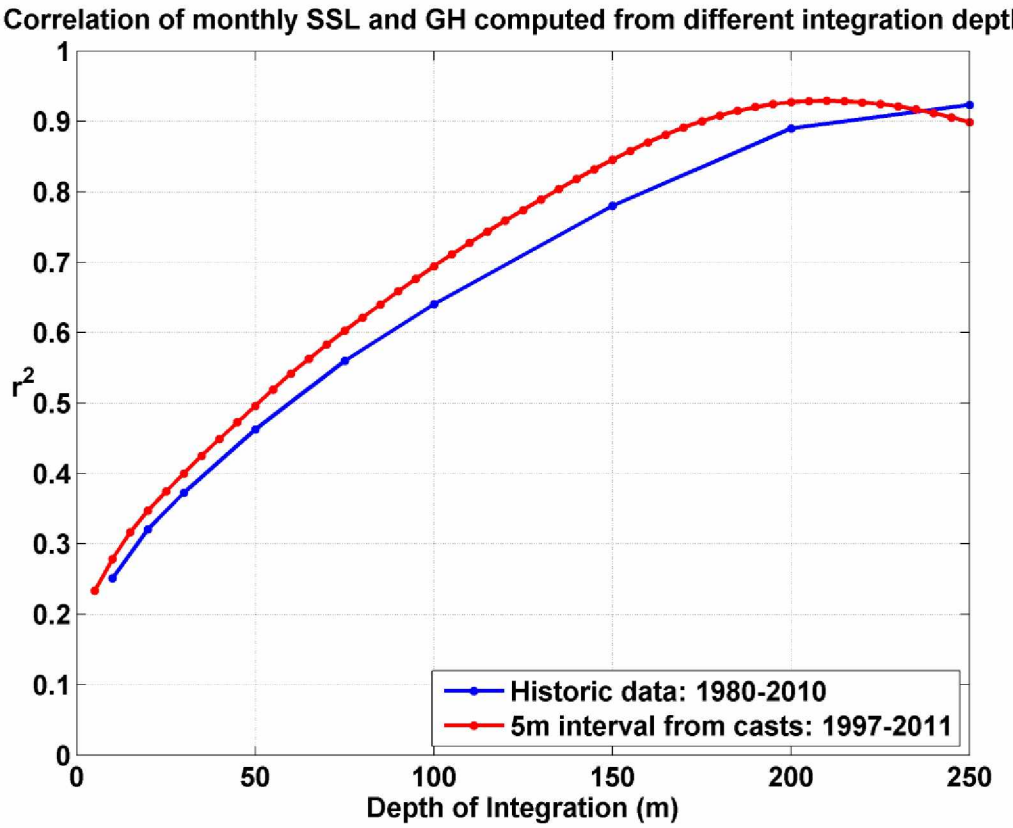

Figure 27. Monthly averages of SSL and GH shown at various depths of integration.

Daily averages of SSL and GH200 are calculated for the period of 1980-2010. The annual fit to these daily averages explains 93 and 72 % of the variance for SSL and GH200, respectively. The fit to GH200 may be diminished given the relative paucity of the data as there were only ~450 total values available for the fit. However, when the daily averages of GH200 were smoothed by 31 days, the percent variance explained by annual cycle rose to 97 %. The amplitude of the fit for SSL (GH200 - smoothed 31 days) is 7.5 (6.7) cm; a difference of ~0.8 cm. The phase (the maximum value) of GH200 occurs on day 295 (October 22nd) and for SSL occurs on day 307 (November 3rd), a difference of ~12 days. The annual fit of discharge explains ~85 % of variance

(of monthly averages); the amplitude is 14400 $m^3 s^{-1}$ and the maximum occurs on day 292 (October 19th).

There are differences, however, in the seasonal changes in these variables. This is evident in Figure 28, which contains the daily averages of SSL and GH200 smoothed with a 45 day running mean. Both variables are minimum in late April and maximum in early October. GH200 decreases from its October maximum steadily into late March, whereas SSL remains at its maximum from October through December and then begins to decrease in January. Note also that while the rates of increase in both variables are similar from April through October, SSL decreases at nearly twice the rate of GH200 from January through April.

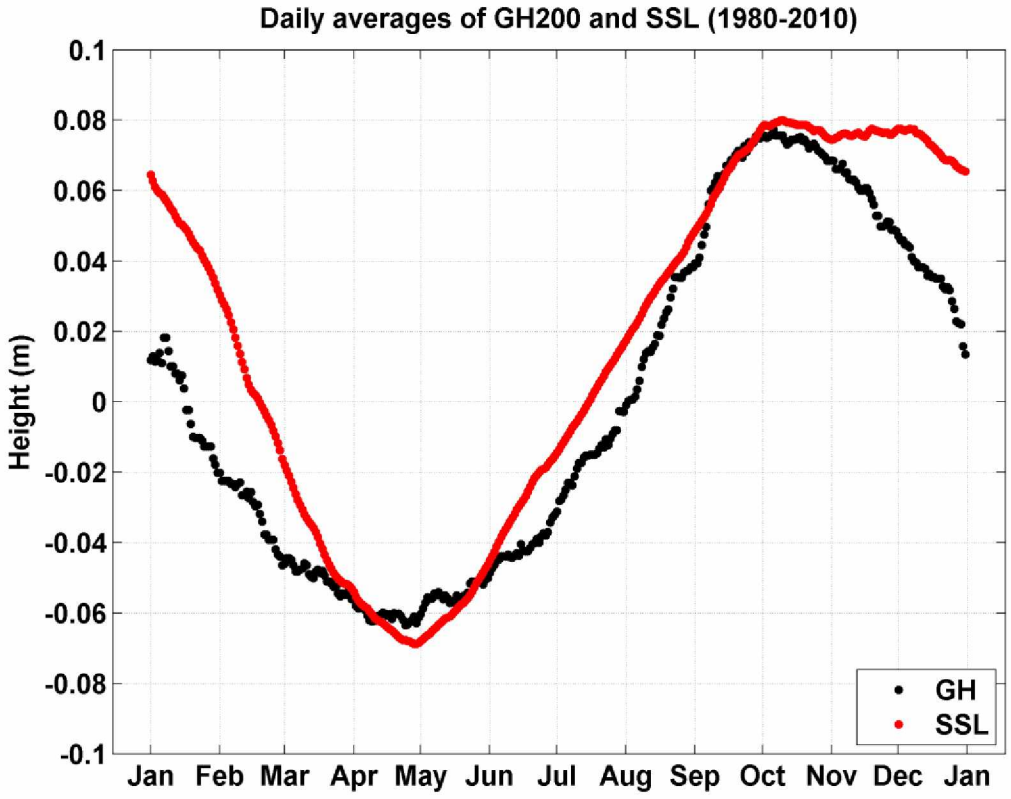

Figure 28. Daily average of SSL and GH200 from 1980-2010 smoothed by 45 days.

I next consider the hydrographic properties at GAK1 using monthly averages to construct climatology. Annually, surface water temperatures vary ~10 ^{o}C, ranging from ~14 ^{o}C in August to ~4 ^{o}C in March; bottom temperatures vary ~< 1 ^{o}C (Figure 29). Annually, surface salinity ranges from ~25 in August to ~31 in April, while bottom salinity varies ~< 1 (Figure 30). The surface water properties are out of phase with the bottom properties. The surface temperature is maximum and surface salinity is minimum in August. The bottom temperature maximum occurs in January and lags the surface temperature maximum by about 5 months. The bottom salinity minimum occurs in March and lags the surface salinity minimum by about 7 months. A surface temperature inversion (surface temperature lower than bottom temperature) begins in December and lasts until April. Salinities, which control water column density (Figure 31), do not undergo an inversion. Summer stratification is strongest from July-October (Figure 31). The least dense surface water occurs in August and is ~1018 kgm^{-3}, and coincides with the densest bottom waters ~1026 kgm^{-3}. The water column is most homogeneous in the months of February to April.

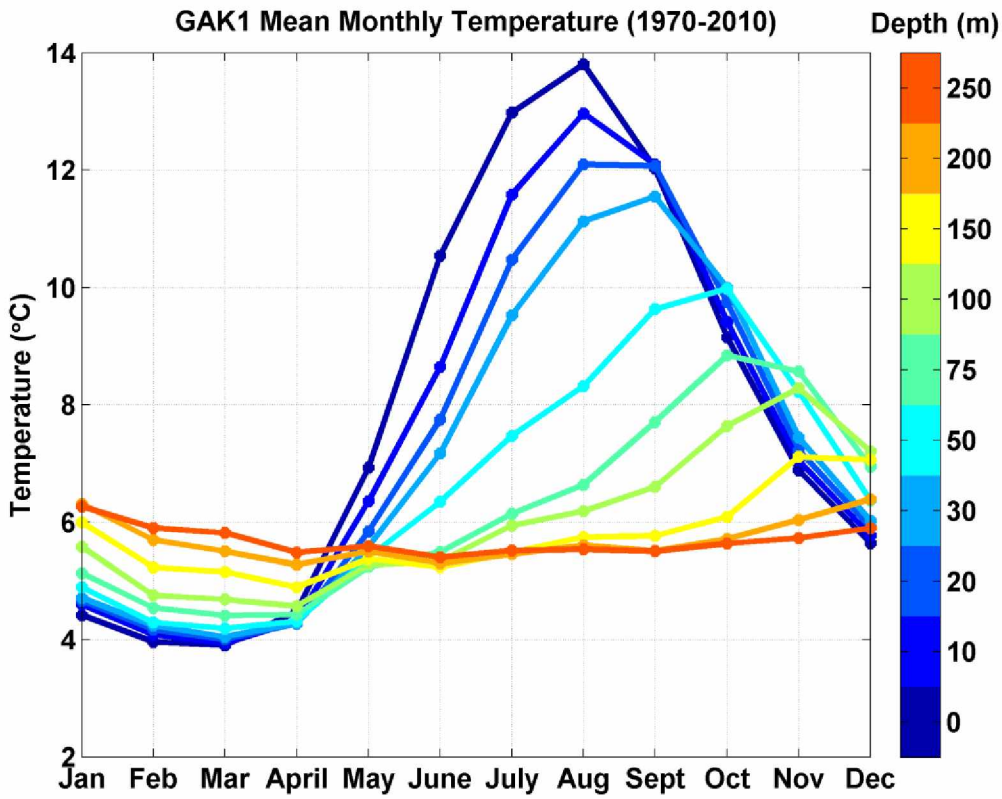

Figure 29. Monthly average temperature at standard depths observed at GAK1.

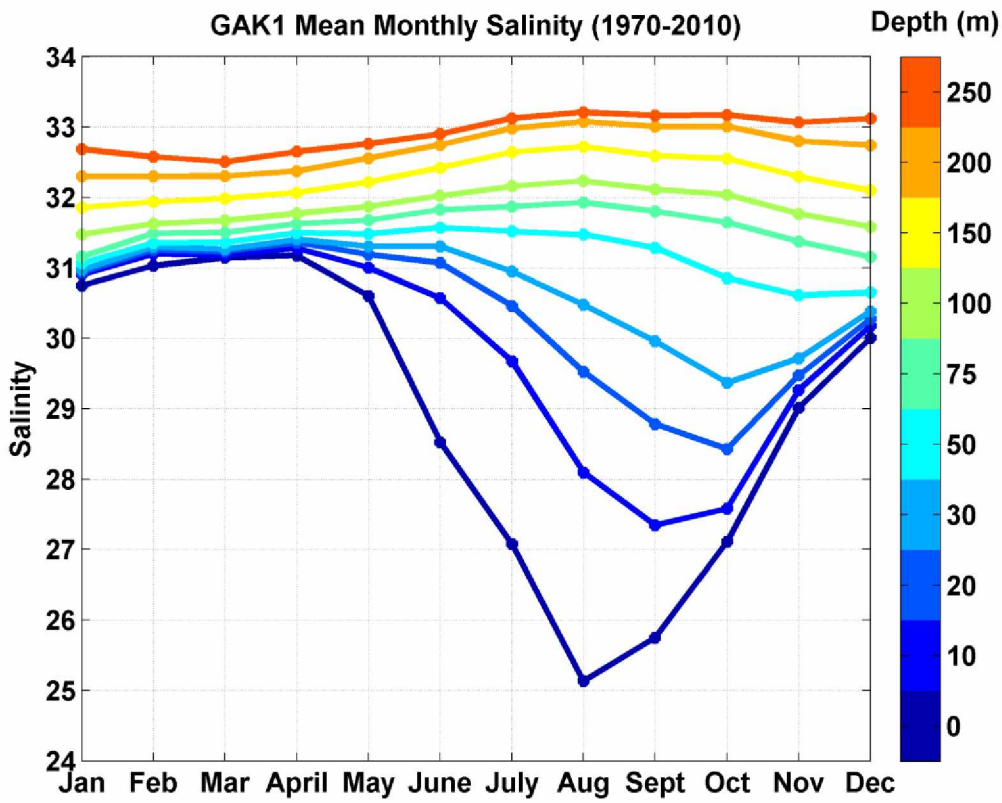

Figure 30. Monthly average salinity at standard depths observed at GAK1.

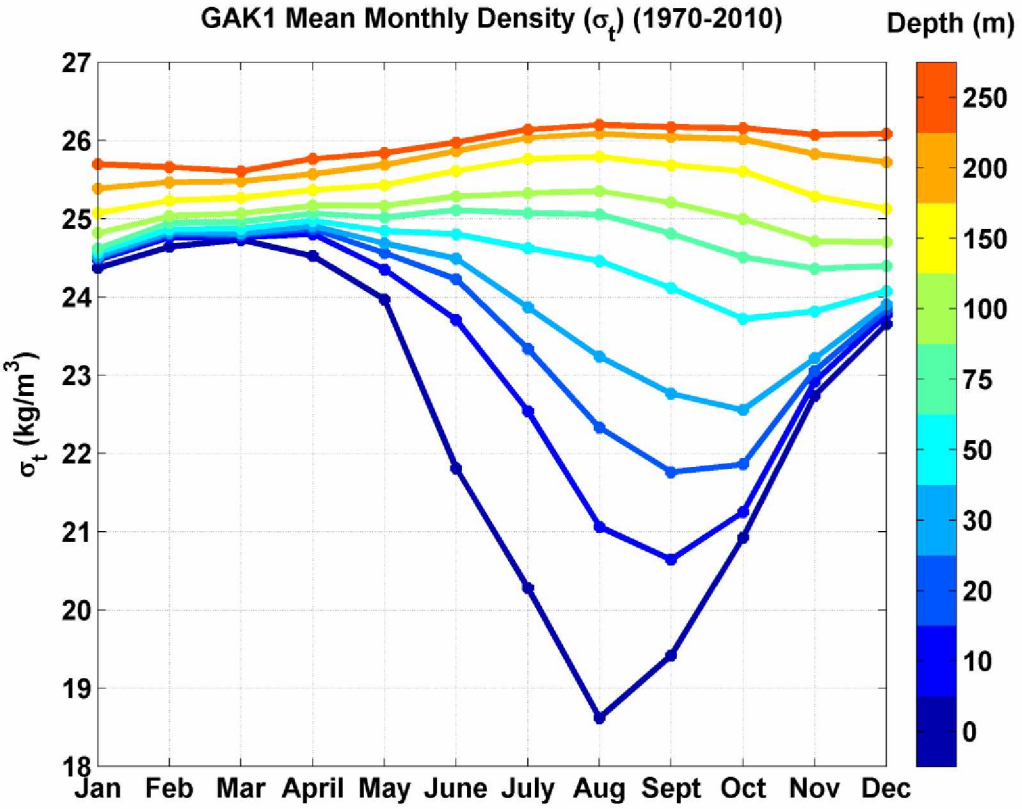

Figure 31. Monthly average density at standard depths observed at GAK1.

The climatology ignores inter-annual variations, which can be substantial and is explored in section 3.6.4. In the following section I consider possible mechanisms that affect the timing and progression of SSL throughout the year by examining residual sea level.

3.6.3 Residual Sea Level

To examine how the hydrography and wind stress control the timing and progression of the annual cycle of SSL during the period 1980 to 2010, I computed the residual SSL by subtracting the daily average (smoothed by 45 days) of GH200 from the daily average of SSL (smoothed by

45 days); i.e., the time series in Figure 28 were subtracted from one another. Residual sea level were then smoothed by 45 days and compared to the daily average of ASWS also smoothed by 45 days (Figure 32).

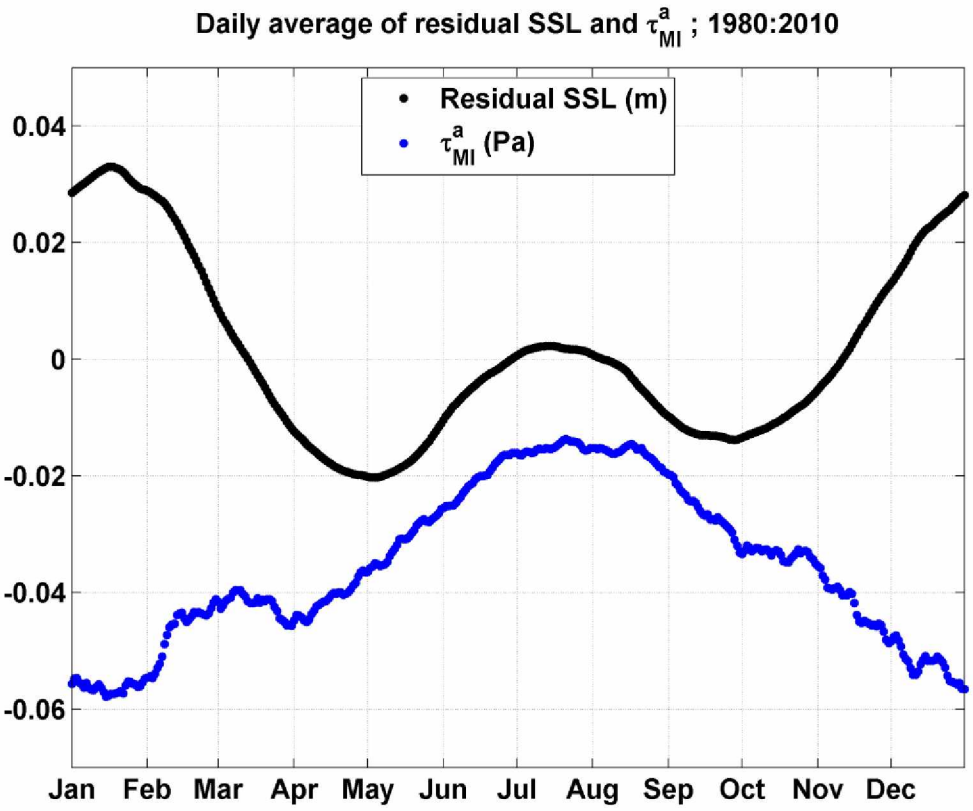

Figure 32. Daily average of residual Seward sea level and τ^a_{MI} .

The residual signal seems to be explained by two mechanisms, 1) wind in the winter months, and 2) differences in the annual cycle of GH200 and SSL in the summer months. Maximum τ^a_{MI} occurs in the winter (mid-January) when downwelling winds tend to elevate SSL. This is consistent with the residual SSL signal, which is greatest in mid-January. The difference between GH200 and SSL can be seen in the months from May to October. I speculate there are

two reasons for this difference. One originates from the physical distance from where the signals are measured (the head and mouth of Resurrection Bay). High rates of runoff that accumulate at the head of Resurrection Bay may contribute a steric influence not captured at GAK1. The second factor is that the upper and lower parts of the water column are out of phase and progress differently throughout the year.

The upper and lower parts of the water column are out of phase and only partially connected. This can be seen by plotting the range of the annual cycle of GH computed at different depths of integration (Figure 33). If the upper and lower layers were always in phase, the maximum range in the annual cycle would occur at the maximum depth, which would correspond to GH250. Instead, the maximum range occurs in the upper 100 m of the water column (GH100). For integration depths greater than 100m, the range of GH decreases. This occurs because the deeper depths reach their maximum values in salinity (density) while the shallower depths are approaching their minimum values.

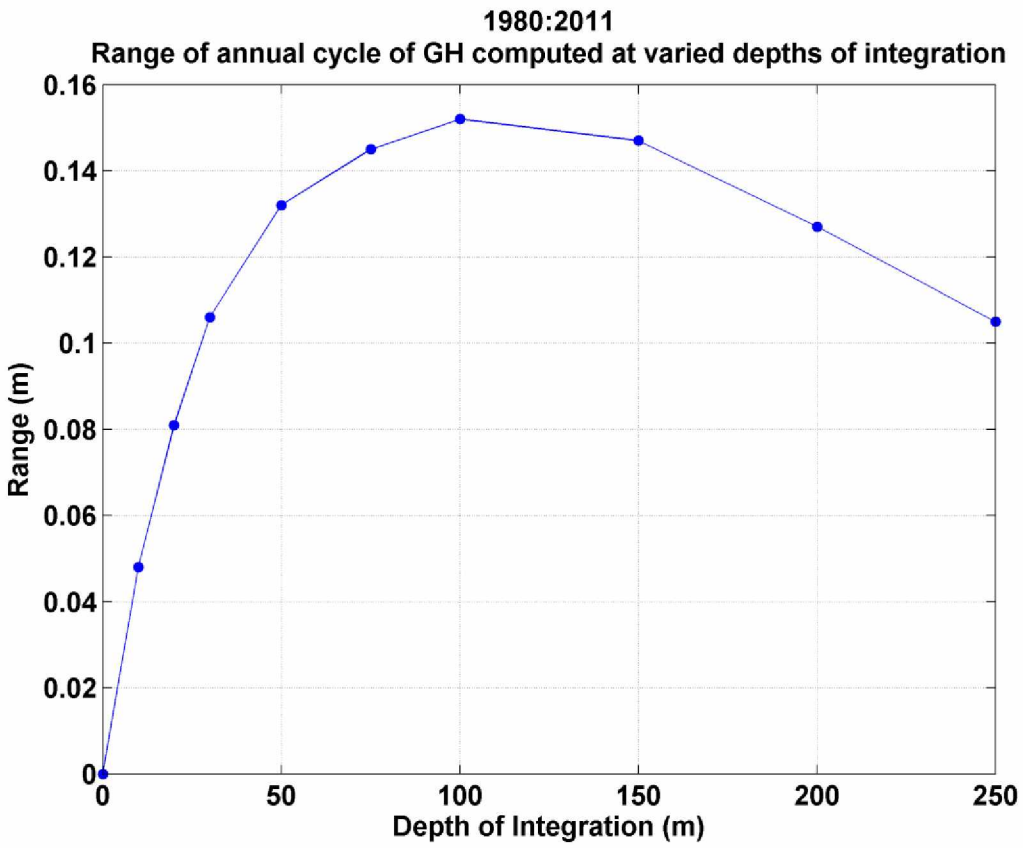

Figure 33. The range of the annual cycle of GH computed at various depths of integration.

SSL and GH200 are only coherent at 6 month and 1 year periods, and aside from the monthly lunar tide, the only identifiable periodicity in GH200 was at the annual cycle. Coherence at the 6 month period was noted by Royer et al. (2001) who ascribed it to spring melt and increased precipitation in the autumn. The results of the two input coherence analysis (input variables of τ_{MI}^{a} and GH200, and the output variable of SSL; Figure 25) indicate that τ_{MI}^{a} has the largest partial coherence with SSL for period less than 60 days. I extended the analysis so that the fundamental period was 365 days. Upon doing so, I find negligible partial coherence at the annual cycle between τ_{MI}^{a} and SSL, while the partial coherence between GH200 and SSL at the annual cycle is ~0.8.

3.6.4 Inter-Annual Variation

To this point I have addressed variations in SSL for periods < 1 yr and the average annual cycle. There are, however, large inter-annual variations in SSL, as well in the other GOA parameters: GH200, discharge, and τ_{MI}^{a}. In this section I examine the inter-annual variability of these variables by computing the amplitude and phase obtained from sinusoidal fits to the annual cycle. Discharge data are monthly, although the phase is reported in days. This analysis is limited to years when mooring data are available. In order to maximize the number of yearly intervals in this time period, I overlapped three of the ten annual fits, with the overlaps ranging from 3 to 6 months (Figure 34). Figure 35, Figure 36 and Figure 37 show the time series of SSL and GH200, discharge, and τ_{MI}^{a}, respectively, during the 2000-2011 period. The variance explained by the annual fits is given in Figure 38, and ranges from 18% in 2004 to 58% in 2009 for SSL. For GH200 the range is 48% in 2004 to 93% in 2007. For discharge the range is 36% in 2010 to 92% in 2009. Finally, the comparable values for τ_{MI}^{a} are 1% (2008) to 6% (2000).

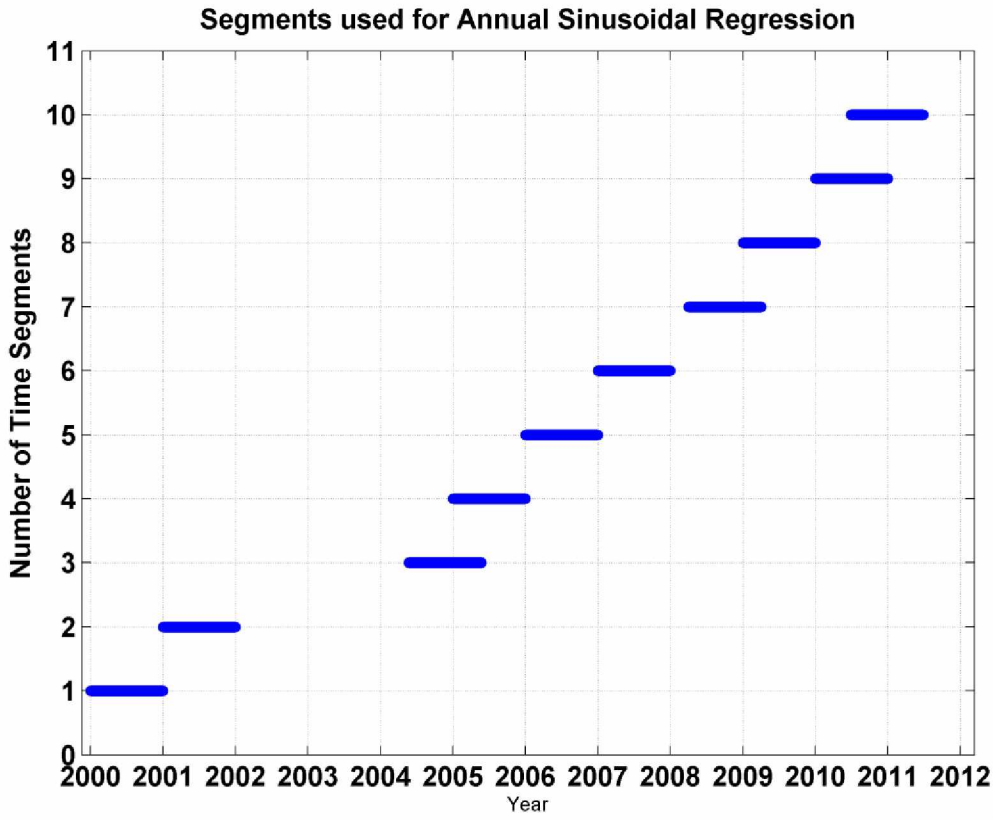

Figure 34. The time segments used for annual cycle regressions that correspond to GAK1 mooring data availability.

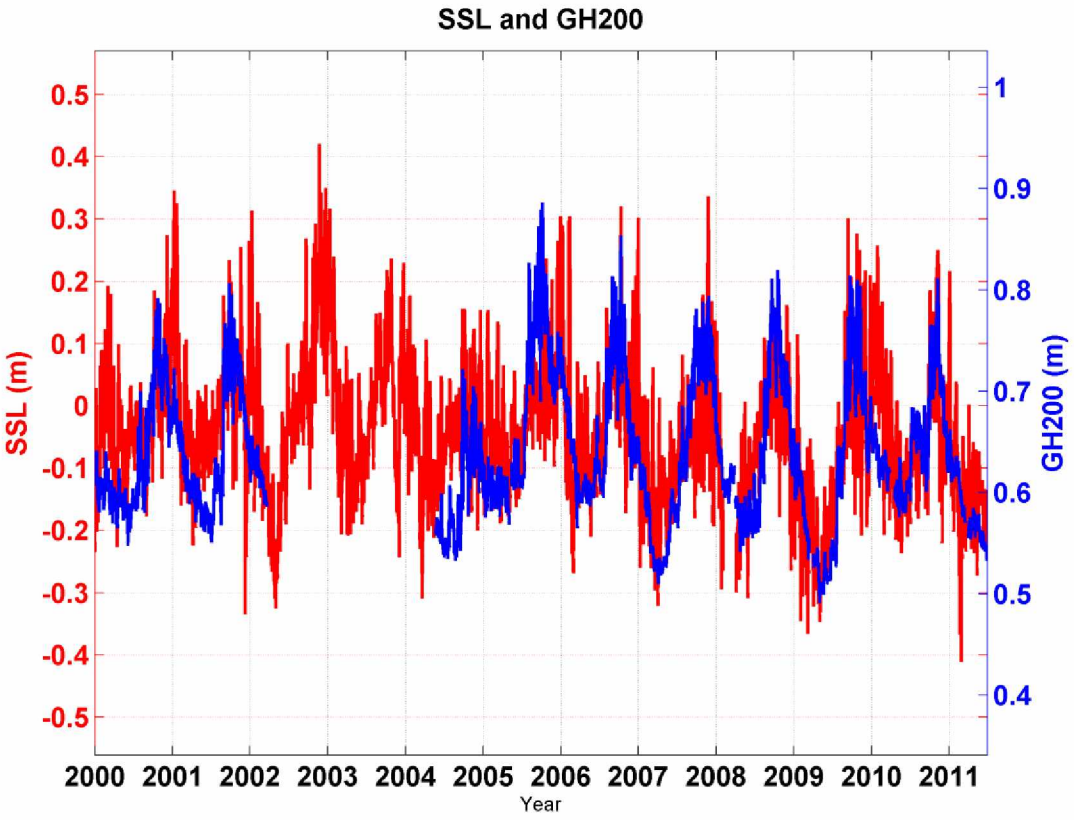

Figure 35. Time series of SSL and GH200 derived from mooring data.

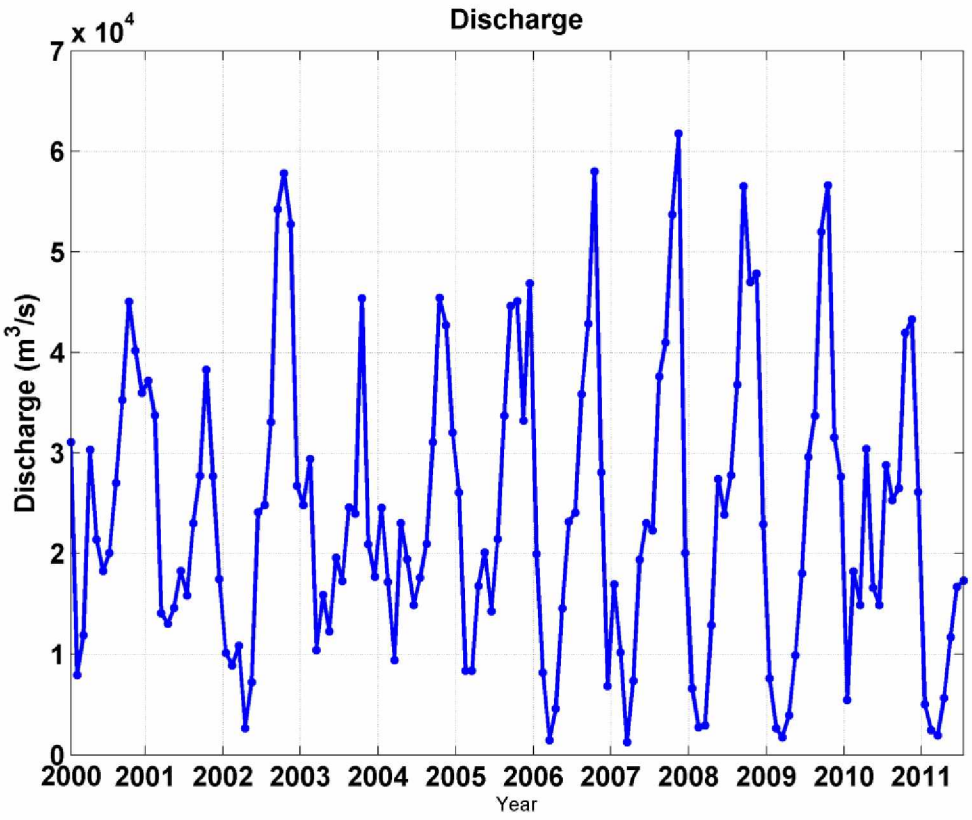

Figure 36. Time series of discharge.

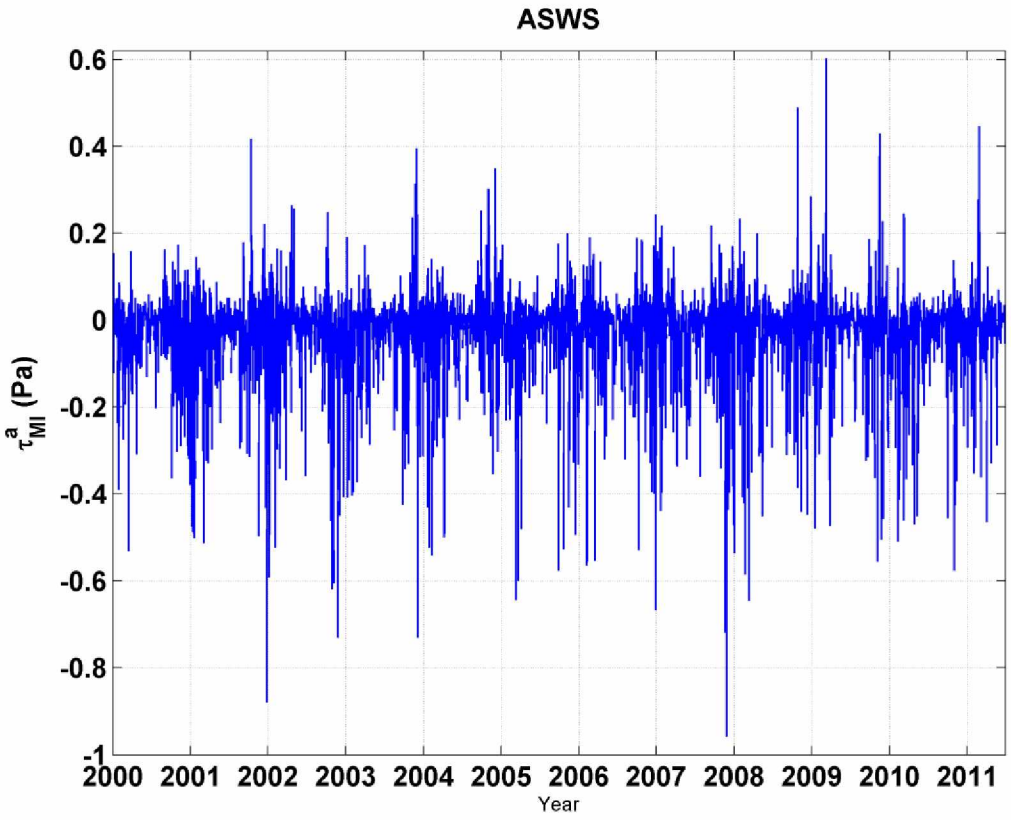

Figure 37. Time series of along-shore wind stress (ASWS) at Middleton Island.

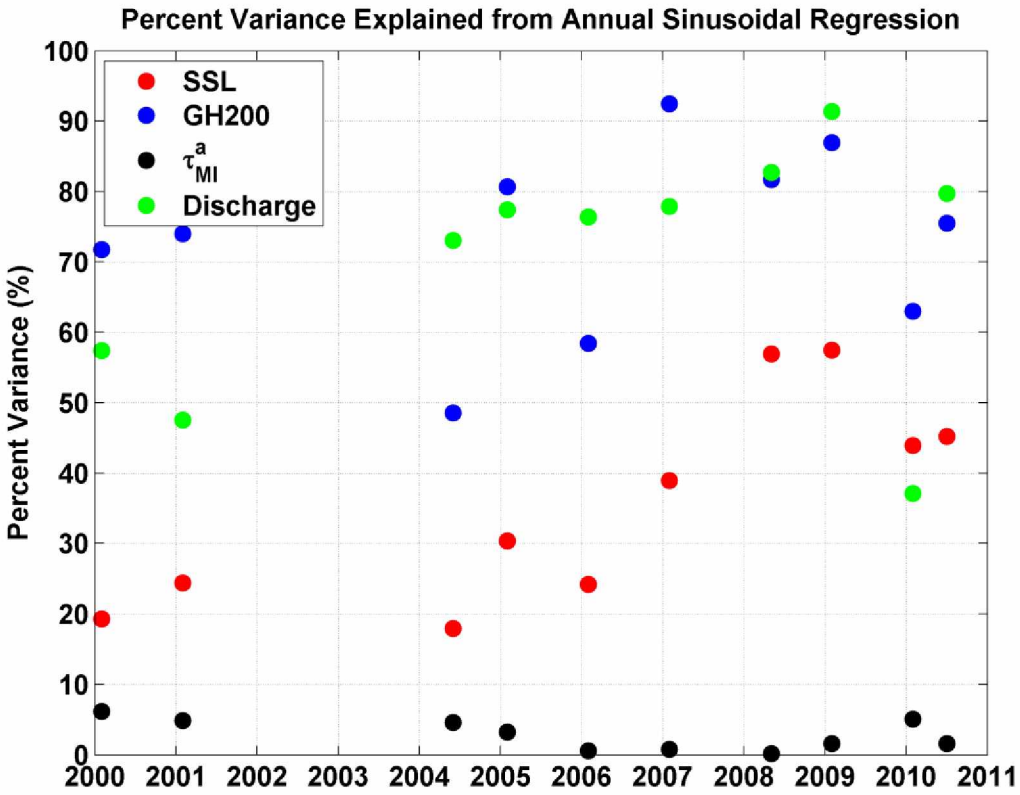

Figure 38. The percent variance explained by annual sinusoidal regression of GOA physical parameters.

By visually examining these annual data plotted with the annual fits (not shown), it appears the phase estimate is more representative than the amplitude estimate. The phase of the annual fits appears to coincide with the phase of the data, while the amplitude (or range) is generally underestimated. For example, over this time period, the average range (the difference between the minimum and maximum) found from the sinusoidal fits of GH200 is ~16 cm, the minimum range is 8cm, and the maximum is 22 cm. These estimates are about 10 cm shy of the actual range from the observed data, for which the average range is 27 cm, the minimum range is 19 cm, and the maximum range is 32 cm. There is no pattern, between SSL and GH200 of which, has larger or smaller amplitude, which is also shown with annual fits to the data from 1980-2010. The average amplitude for discharge from the annual fit is about 1.8×10^4 $m^3 s^{-1}$. Figure 39 shows the amplitude of τ^a_{MI}, discharge, GH200 and SSL found from the sinusoidal fit.

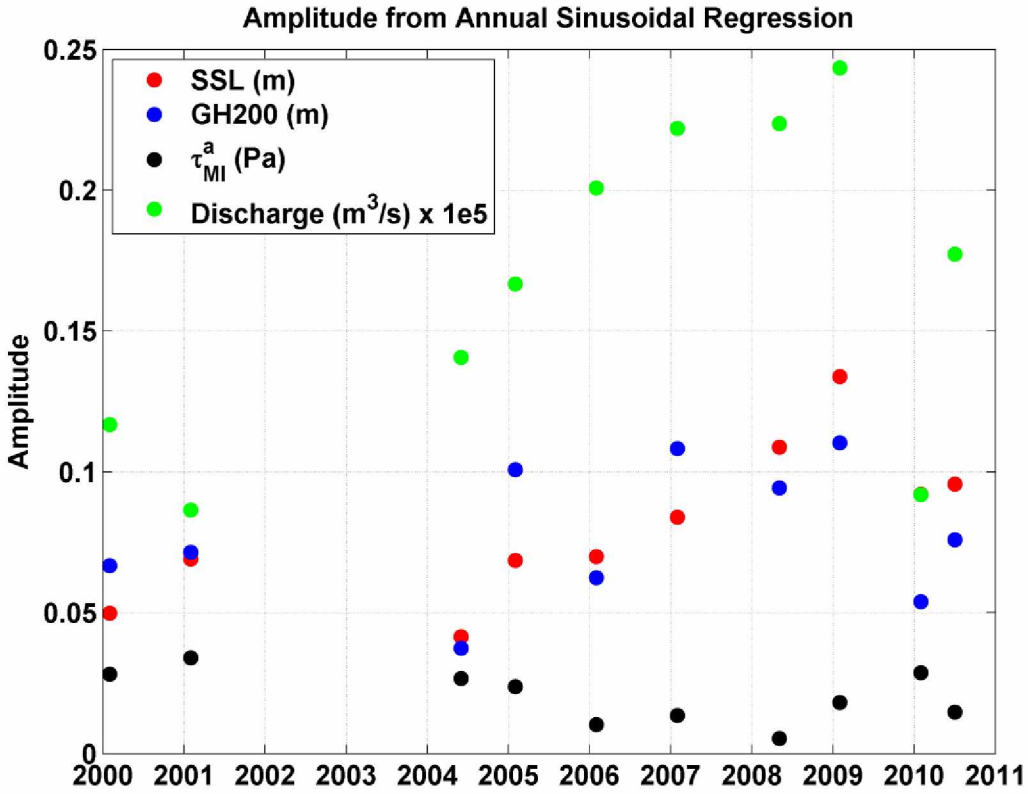

Figure 39. Amplitude of annual sinusoidal regression of GOA physical parameters.

The phase of the annual fits (referenced to January 1st) is shown in Figure 40. For discharge the phase ranges between days 258-325, with the average occurring on day 282 (October 9th). The phase of GH200 (SSL) ranges between day 276-351 (262-351) with the average occurring on day 304 (305) or October 31st and November 1st, respectively. Although these variables are nearly in-phase over this time interval, the range in phase difference between SSL and GH200 is 2 and 50 days (Figure 41). It must be noted that discharge data are monthly so that the phase estimates expressed in days are likely crude. Nevertheless, these results are physically consistent in that discharge precedes GH200, and both of these variables precede SSL. The inter-annual variation in phase of ASWS is large due to the large variability in the temporal

occurrence and strength of storms. The phase of ASWS reaches its maximum in the months between November and March.

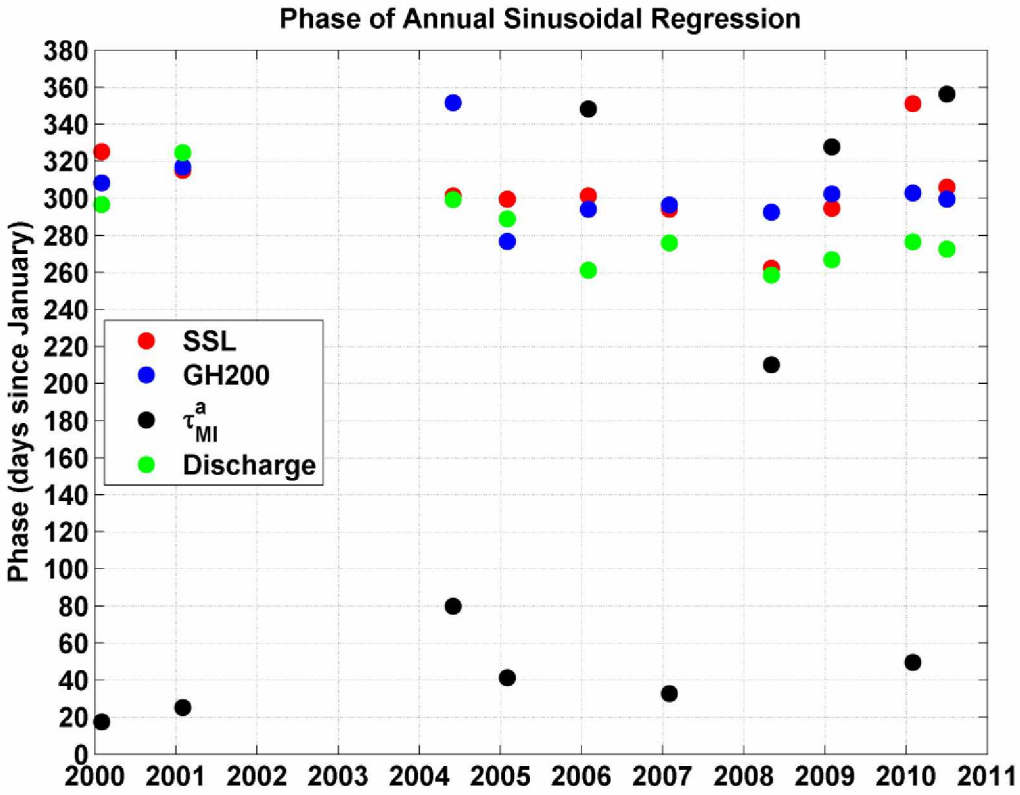

Figure 40. The phase of each of the GOA parameters examined.

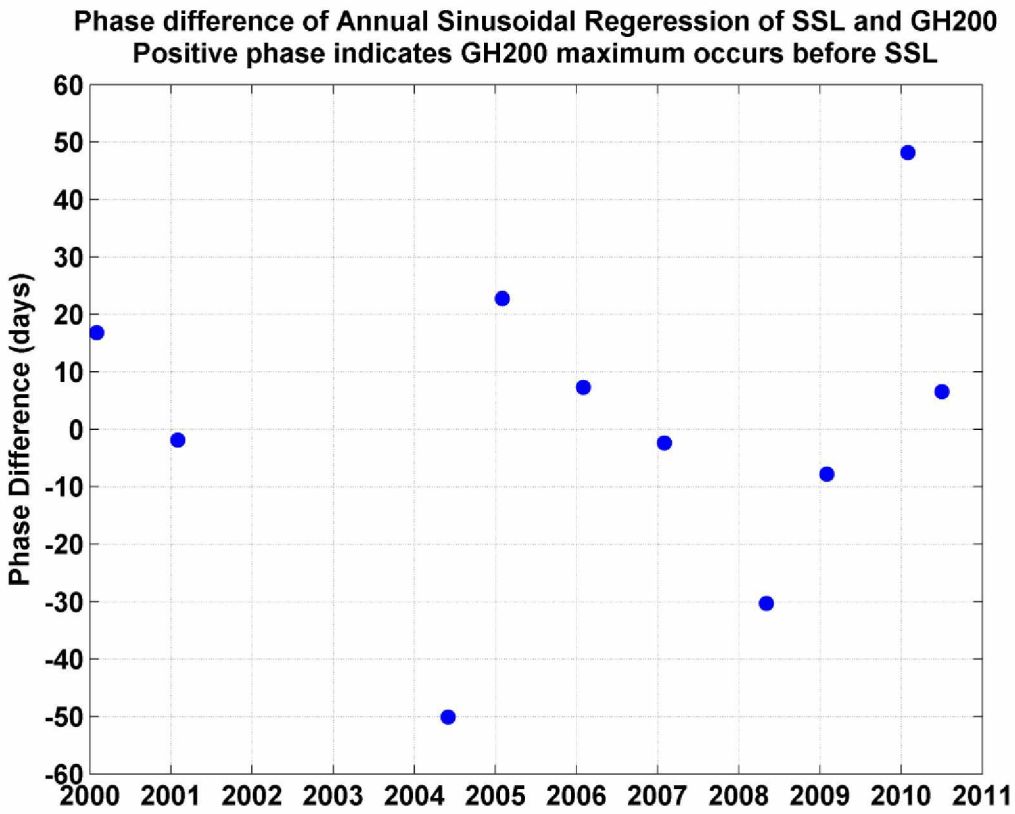

Figure 41. The phase difference between SSL and GH200 determined from annual sinusoidal regression.

3.7 Long term trends of Hydrography and Discharge

Royer (2005) examined trends in the monthly anomalies of GAK1 temperature and salinity at the surface, and the upper and lower layers for the period 1970 to 2000. In this section, I update his analysis by using his approach to consider linear trends from 1970 to 2010 in GAK1 hydrography and discharge. The upper layer is taken to be the average of data obtained at depths of 0, 10, 20, 30, 50, 75 and 100 m, and the lower layer is taken to be the average at the depths of 100, 150, 200 and 250 m. At the surface (at 0 m), temperature and salinity have warmed and freshened over the past 40 years. Surface temperature (T0) has increased more than one degree and surface salinity (S0) has decreased about 0.4. Upper (lower) layer temperatures rose by nearly +0.9 (+0.67) ^{0}C. Upper layer salinity has decreased by -0.14 and lower layer salinity has increased by +0.06. As shown in Table 1, Royer's (2005) trends (1970-

2000) were generally higher than the 1970 to 2010 trends, except for lower and upper layer salinity, which were slightly higher in my estimates. However, the signs of the trends in both Royer's (2005) and my analyses are all of the same direction. A positive trend in discharge is also evident (Table 1). Discharge has increased by ~3900 $m^3 s^{-1}$ over the past 40 years. Recall that because stratification is primarily a function of salinity, the opposing trends in upper and lower layer salinities imply that the shelf is becoming more stratified with time. In general, low salinity water is associated with low nutrients while higher salinities have higher nutrient concentrations (Childers et al., 2005) and iron (Wu et al., 2009).

Global sea level is a function of: 1) increased discharge into the ocean from increasing precipitation and melting glaciers, 2) volume increase by a warming ocean, and 3) tectonic rebound. This analysis, so far, suggests that the first two are occurring in the GOA, as volume expansion was gauged in this study by examining the long term trend of GH200. It was found to have increased nearly 1.7 cm over the past 40 years.

Table 1. Decadal term trends (1970-2010) of hydrographic data at GAK1 and Seward discharge, n is the number of months when data were available over this time interval. Royer's (2005) trends from 1970-2000 are in brackets for comparison.

Parameter	**n**	**Slope** (per decade)	**Total 40yr change**	**Significance %**
T0	285	+0.26 ^{0}C [+0.33]	+1.07 ^{0}C	>99
S0	285	-0.10 [-0.11]	-0.40	>92
Upper layer T	285	+0.22 ^{0}C [+0.32]	+0.89 ^{0}C	>99
Lower layer T	284	+0.16 ^{0}C [+0.26]	+0.67 ^{0}C	>99
Upper layer S	285	-0.034 [-0.022]	-0.14	>92
Lower layer S	284	+0.016 [+0.013]	+0.06	>90
GH200	281	+0.41 cm	+1.67 cm	>95
Discharge	492	+960 m^3s^{-1} [+1820]	+3920 m^3s^{-1}	>99

3.8 Long term trends of GOA sea level

Continental rebound (or uplift) can raise the earth relative to the ocean, which makes sea level appear to decrease. This mechanism can create large localized deviations in the sea level record, but it does not occur in all parts of the ocean. Sea level has decreased at each of the locations examined in the GOA. Using simple linear regression analysis from 1970- 2010, I found that over the past 40 years the total uplift equates to a sea level change of -43 cm at Yakutat, -10 cm at Seward, and -7 cm at Sitka (Table 2). Over this period, I found uplift rates at Seward to be -2.5 mm yr^{-1}, -10.54 mm yr^{-1} at Yakutat, and -1.75 mm yr^{-1} at Sitka. Though I report the rates of the 40 year trend, Larsen et al. (2003) report the trend rates for the year 2000. In comparison to my results, in their more in-depth analysis, Larsen et al. (2003) concluded uplift rates to be -10.4 mm yr^{-1} at Seward, -13.7 mm yr^{-1} at Yakutat, and -3 mm yr^{-1} at Sitka.

Table 2. Long term trends (1970-2010) of GOA sea level.

Location	n	Slope	Total 40yr change	Significance %
Seward	437	-2.5 mm yr^{-1}	- 10.2 cm	>99
Yakutat	475	-10.54 mm yr^{-1}	- 43.2 cm	>99
Sitka	492	-1.75 mm yr^{-1}	- 7.2 cm	>99

Larsen et al. (2003) examined uplift rates using 15 tide gauge stations around the GOA, and sea level decreased at all locations. Their data records spanned from roughly 1940 to 2000. They found that rates of rebound were spatially and temporally dependent; uplift rate varied spatially with the change of localized glacial loads. Stations near subduction zones often have non-linear trends while those near strike-slip zones have linear trends (i.e., Sitka). Yakutat is affected by both subductive and strike-slip interactions. Rebound rates are also affected by earthquakes; for example, sea level stations near-field of earthquakes can exhibit non-linear or oscillatory uplift (e.g., Seward). Tide gauges within earthquake near-fields can be severely displaced, making the utilization of these records more difficult.

Continental uplift in the GOA is driven by various complicated tectonic interactions, and determining uplift rates requires more sophisticated analysis than that conducted herein. However, my results conclude that uplift is the dominant mechanism for long term sea level change in GOA.

3.9 Climatic Signals in GOA

On decadal and sub-decadal time scales, ocean temperature and sea level can be strongly influenced by large scale climatic patterns. Coastal locations are subject to additional episodic or quasi-episodic climatic events. Climatic patterns and events are known to have significant relationships with various GOA parameters (Royer, 2005). In this section I extend Royer's (2005)

work on GOA climate signals by including an additional 10 years of data. The GOA parameters investigated are: salinity (0 m), salinity (0-50 m), salinity (50-250 m), sum of temperature anomalies (STA) from 50-250 m, GH200, discharge, and GOA sea level; I examine the relationship between these GOA parameters to several climate indices: PDO, NPGO and SOI for the 1970-2010 period. All relevant time series were first smoothed with a 13-month running average before comparisons.

Distinguishing the influence of individual climatic forcing mechanisms on these variables is difficult because they can force interactively, and thus either cancel or accentuate their effects (Papineau, 2014). As mentioned by Mantua et al. (1997), PDO and SOI are themselves correlated, and their correlation increases as the degree of smoothing increases. Regardless of the relationship between these variables, they yield different correlations with the GOA variables of interest. I examine these relationships using cross correlations expressed by the coefficient of determination (r^2) between data at various time lags (given in months).

Di Lorenzo et al., (2008) found NPGO to be significantly related to sea surface salinity and ASWS collected from oceanic stations along southern California. They suggested that winds created appropriate up- or downwelling conditions that modify the vertical salinity distributions. I make similar correlations within my study region; however, these correlations are insignificant at both the long-term and seasonal time scales. As a consequence of these results, I focus on the PDO and SOI in the following analysis. I continue this section first with results from ENSO then with PDO.

3.9.1 ENSO

ENSO is a global phenomenon that originates along the equatorial Pacific. The ENSO signal propagates poleward and has both an atmospheric and oceanic component (Subbotina et al., 2001). The ability to distinguish the signal decreases with latitude, likely because other forcing mechanisms mask its presence (Melsom et al., 2003). The general consensus is that the atmosphere around the GOA basin, during times corresponding to ENSO events, responds with

a strengthening of the AL and weakening of the NPH (Subbotina et al., 2001; Melsom et al., 2003; Schneider and Cornuelle, 2005). However, coastal GOA winds do not seem to be affected by these events (Stabeno et al., 2004), and evidence for the atmospherically forced ENSO signal in GAK1 hydrography is lacking (Royer, 2005). Because coastal winds are not sensitive to ENSO, changes in transport of the ACC are not expected (Stabeno et al., 2004).

The oceanic component of ENSO is expressed in sea level and hydrography. As an El Nino develops at the equator (corresponding to a negative SOI), the signal propagates poleward along the eastern boundaries of the Pacific Ocean and raises sea level and water temperature. The sea level component is a barotropic response, and the hydrography component is a baroclinic response.

I correlate the GOA variables of interest to SOI, and in all cases the GOA variables lag SOI (Table 3). Discharge and ASWS are uncorrelated with SOI. Surface salinity is not correlated to SOI, while salinity correlations at (0-50 m and 50-250 m) are small (r^2~0.1) with a lag of 6-7 months. STA and GH200 are correlated with SOI with an r^2~0.2 at lags of 7-9 months. GOA sea levels show the largest correlations with the SOI with r^2~0.33 and a lag of 1-5 months. Although the precise location of the origin of the ocean wave signals associated with an ENSO event is not known, I use 10,000km as the distance from the equator to GAK1. With a time lag of 7-9 months, I find the baroclinic propagation velocity to be around 48-37 km day^{-1} (0.55-0.43 m s^{-1}).

The most significant correlation with SOI and temperature was for depths between 75-150 m (Royer, 2005), at which depths he found the maximum correlation to be r^2~0. 14 at a time lag of 7-10 months. This corresponds to a propagation speed from the equator of ~47-35 km day^{-1} (0.54-0.41 m s^{-1}). Royer and Weingartner (1999) identified the baroclinic component of ENSO by recognizing that temporal temperature changes (at GAK1) were coherent with depth at times corresponding to ENSO events. They suggest that local forcing was not responsible for the creation of the baroclinic signal, but rather, the signals were advected into the region. It is uncertain as to whether the baroclinic signal propagates only in the subsurface layer, or

whether it propagates through the entire water column while being masked by other forcing in the upper layers. For example, Royer (2005) found GAK1 water temperature above 20m to be least correlated with SOI. For GOA sea levels, I use a lag time of 2-4 months to find a barotropic propagation velocity to be ~166-83 km day^{-1} (1.9-0.96 m s^{-1}). Thus the barotropic (sea level) propagation velocity is at least twice as rapid as the baroclinic signal as reflected in hydrography.

My estimates fall within the range of other estimates. Melsom et al. (2003) examined the ENSO signal at Sitka using both a model and observed data (from Sitka). When the ENSO signal reached Sitka the modeled signal had greater amplitude and occurred slightly sooner than the observed signal. They estimated the arrival of the observed signal to be around 1.5-2 months with a velocity of ~216 km day^{-1} (2.5 m s^{-1}); this is at the higher end of the velocity estimates found in the literature. Enfield and Allen (1980) used two methods to calculate the propagation velocity of sea level and they found the range to be 75-180 km day^{-1} (0.86-2 m s^{-1}), which using 10,000 km, yields 1.8-4.4 months. Chelton and Davis (1982) found lower propagation speeds, which more closely correspond to the baroclinic speeds that I computed. They estimated the sea level signal to travel with a velocity of 35 km day^{-1} (0.4 m s^{-1}), which corresponds to 9.5 months using 10000 km as the distance.

Chelton and Davis (1982) examined sea level along western North America and examined the difference in transit time of El Nino-associated, sea surface, and sea level signals. They suggest that the hydrographic component leads the sea level component, though they did not present a propagation velocity of ocean temperature. Their results are opposite to mine, which suggests that the sea level signal propagates faster than the hydrographic signal.

As a final note, there is variability in the amplitude and timing of an ENSO event. For example, the two largest ENSO events considered here occurred in 1982-83 and 1997-98. The 1997-98 event generated higher monthly mean sea level and developed at a different time of year. The 1982-83 event developed late summer and ended in early spring, whereas the 1997-98 event

developed in spring and ended in late winter (Subbotina et al., 2001). The variability in propagation time and speed of a passing wave may result from variability in the amplitude and timing of the ENSO event near the equator as well as wave dispersion along the coastal path due to temporal differences in stratification, due to water depth and shelf width (Subbotina et al., 2001).

3.9.2 PDO

PDO is a decadal measure of sea surface temperature and SLP in the North Pacific Ocean. It is not a dynamic mode but rather it arises from the superposition of the forcing of El Nino, AL, and the Kuroshio-Oyashio extension, and the contribution from each of these forcing mechanisms acts on various timescales (Schneider and Cornuelle, 2005). In this section I present correlation results between the PDO index and the GOA variables of interest. In all cases, the GOA variables of interest lagged the PDO. PDO was positively (negatively) correlated to discharge, temperature, GH200, and sea level (salinity). The largest correlations and the corresponding lags are shown in Table 3.

Maximum correlations between salinity (discharge) and PDO were r^2~0.14 at 2-3 (0) months. Maximum correlations between STA (and GH200) and PDO were r^2~0.38 at 3 months. Maximum correlations for PDO and GOA sea level occurred at zero lag, for SSL with r^2 ~ 0.50, for YakSL with r^2 ~ 0.66, and for SitSL with r^2 ~ 0.36. Seasonal comparisons with PDO and GOA variables yielded no notable difference compared to non-seasonal comparisons. Royer (2005) found the correlation between temperature of the water column and PDO to be r^2=0.23 at ~3 month lag.

The PDO accounts for $\geq$ 50 % of the variance of SSL and YakSL, which is substantially larger than for the other variables considered. Perhaps this result is not so surprising given that the PDO is a measure of both the state of the atmosphere and the ocean, which both affect sea level. The entire water column at GAK1 responds to the PDO pattern, which reflects not only SST variability but the heat content of the upper water column in northern GOA (Royer, 2005).

More attention has been paid to the PDO to describe the decadal variability in winter than in summer because the PDO pattern is more pronounced in winter; the PDO is positively correlated with wintertime precipitation along the coast of the central GOA. When PDO is in a positive state (as it is presently) the GOA tends to experience an enhanced cyclonic flow of warm moist air, which is consistent with heavier than normal precipitation (Mantua et al., 1997). Coastal weather in GOA does not appear to be tightly coupled with PDO, though wind forcing in the central portion of GOA basin might be (Stabeno et al., 2004). Correlations between τ^{a}_{MI} and PDO were insignificant.

Table 3. The correlation (r^2) and its associated lag noted in parenthesis between climatic indices and GOA variables, n is the number of months used in each analysis. In all cases the GOA parameters lags the climatic indices.

Parameter	n	PDO	SOI
S0m	280	0.14 (2-3)	NA
S0-50m	280	0.16 (2)	0.09 (6-7)
S50-250m	280	0.14 (2)	0.10 (6)
STA	280	0.38 (3)	0.18 (8-9)
GH200	280	0.38 (3)	0.22 (7-8)
Discharge	480	0.13 (0)	NA
SSL	425	0.50 (0)	0.34 (4-5)
YakSL	465	0.66 (0)	0.34 (1)
SitSL	480	0.36 (0)	0.32 (2-3)

4 Conclusions

In this study I examined sea level at Seward (SSL), Yakutat (YakSL) and Sitka (SitSL), and hydrography at oceanographic station GAK1. I used various time and frequency domain methods of analysis to examine the forcing from tides, sea level pressure (SLP), wind, the seasonal cycle, and climate variations. I also determined long term trends for sea level and hydrography. High frequency tides (periods $\leq$ 1day) are responsible for ~97 % of SSL variance. Atmospheric energy is greatest (least) in winter (summer). Winter SLP contains ~5 times more energy than summer SLP (Figure 7). SLP, operating through the inverted barometer effect, accounts for ~2% of SSL variance. Together, the influence of tides and SLP account for ~99 % of the total SSL variance. These variables were then removed from sea level records and the remaining ~1 % of total SSL variance, e.g., the inverse-barometer corrected, subtidal SSL, was examined.

After the removal of tides and SLP, the influence of wind on sea level becomes evident. Along-shore wind stress (ASWS) contains ~4 times more energy (variance) than cross-shore wind stress (CSWS) (Figure 13). Winter ASWS contains ~8 times more energy than summer ASWS (Figure 14). Winter SSL contains ~4 times more energy than summer SSL (Figure 11). Winds over the GOA shelf are downwelling favorable and highly coherent with GOA sea level, with the coherence greatest in the winter (Figure 17). Along- and cross-shore winds account for ~60% of SSL variance for periods of 2-90 days (Figure 15). SSL has a barotropic and baroclinic response to ASWS. The barotropic response is seen when downwelling winds accumulate water along the coast. The baroclinic response is seen as an increase in sea level from downwelling winds that modify the vertical salinity (and density) distribution of the water column through along- and cross-shore advection of waters (Figure 25). These changes alter sea level by increasing or decreasing the steric height of the water column. To a lesser extent, wind also affects the annual cycle of SSL as shown by comparing the daily averages of ASWS to residual SSL. High residual sea level in the winter is coincident with high wind stress, with each of these variables attaining their maximum in January (Figure 32).

Along-shore sea level coherence in GOA was computed using sea level from Seward, Yakutat and Sitka. Coherence is lowest (<0.2) at short periods (5-6 days), and greatest at the annual cycle (~0.8) (Figure 20). The phase information provided insight into the direction of coastal sea level propagation at 3 distinct time scales, in which the phase is significantly different than zero (Figure 21). For periods < 6 days, sea level fluctuations propagate clockwise, most likely due to a forced response from the west to east passage of storms across the GOA. For periods of ~6-100 days, sea level fluctuations propagate counterclockwise. This signal is probably associated with shelf waves that travel with the coast on the right and other disturbances. Shelf waves arise primarily from wind forcing. At the annual cycle sea level propagates clockwise, though the reason for this is not clear.

The assessment of shelf waves is complicated due to bathymetric and shelf-width variability. Numerical models would be the most useful tool for assessing these subtidal waves, especially given the complex bathymetry and coastline, the large variations (spatially and temporally) in stratification, and the seasonally-varying strength of the ACC and outer shelf currents. These complications suggest that shelf wave signatures are broadband in nature and imply that distinct sea level signals cannot be easily ascribed to particular wave modes. I have shown with multiple input coherence analysis that regional along- and cross-shore winds account for ~60 % of sea level variance for periods of 2-90 days. This result implies that ~40 % of the variance within this time scale remains unexplained. Presumably, much of this unexplained variance is associated with shelf waves. Some of the unaccounted variance may also originate from non-locally generated waves from south of the GOA, but the degree to which this occurs has not been explored.

I showed using two methods that SSL is most correlated to GH referenced to 200m (GH200), rather than any other integration depth. On short timescales (period less than 60 days) SSL and GH200 are in phase (Figure 25). However, in a climatological sense (1980 to 2010), the annual cycles are slightly out of phase, which was shown by applying sinusoidal least squares fits to daily averages of the GOA variables of interest. The annual cycle (from the annual fit) accounts

for 93, 97, 85 and 40 % of the variance of the daily averages of SSL, GH200, discharge (monthly averages), and τ_{MI}^{a} , respectively. I found that SSL and GH200 (smoothed by 31 days) have similar amplitudes (< 1 cm difference), while the phase (the maximum value) of GH200 occurs on day 295 (October 22nd) and of SSL occur on day 307 (November 3rd); a difference of ~12 days (Figure 28). The discharge maximum occurs on day 292 (October 19th), and maximum τ_{MI}^{a} occurs on ~January 22nd. Consequently, the annual cycle of SSL seems to be driven by GH200 variations, as suggested by the strong similarity in their phases and amplitudes. Annual variations in GH are driven by freshwater discharge, which is also an important dynamical driver of the Alaska Coastal Current (ACC). Discharge is greatest in late summer-early fall and least in winter.

The inter-annual variability in amplitude and phase of discharge, GH200, SSL, and ASWS is also large. These were assessed by sinusoidal fits to ten 1-yr-long data segments, over the time period of roughly 2000-2011 (when mooring data were available at GAK1). The variance explained by the annual fits range from 36 % in 2010 to 92 % in 2009 for discharge. For SSL the range is 18 % in 2004 to 58 % in 2009 while for GH200 the range is 48 % in 2004 to 93 % in 2007. The comparable values for τ_{MI}^{a} are 1 % (2008) to 6 % (2000) (Figure 38). Discharge phase range between days 258-325, with the average of those estimates occurring on day 282 (October 9th). The phase of GH200 (SSL) ranges between day 276-351 (262-351) with the average occurring on day 304 (305) or October 31st and November 1st, respectively. Over this time period, the phase difference between SSL and GH200 varied from 2 to 50 days (Figure 41).

High rates of glacial melt in GOA are probably responsible for much of the long term changes in discharge and hydrography (Table 1). From 1970-2010, discharge has increased ~3920 $m^3 s^{-1}$. This discharge trend coincides with a steric height increase of ~+1.7 cm over the same time period. The upper layer is taken to be the average of data obtained at depths of 0, 10, 20, 30, 50, 75 and 100 m, and the lower layer is taken to be the average at the depths of 100, 150, 200 and 250 m. Surface temperatures have increased ~+1.1 ^{o}C, upper (lower) layer temperature has

increased ~+0.9 ^{o}C (+0.7). Surface salinity has decreased ~-0.4, upper (lower) layer salinity has changed ~-0.14 (+0.06).

The opposing trends of increased temperature and decreased surface salinity lead to an increase in stratification on the shelf, as does the increased coastal discharge. This has potential effects on marine production worth considering. On one hand, we expect production to decrease due to enhanced stratification and subsequent decrease in nitrate concentrations in the euphotic zone. On the other hand, increased runoff implies enhanced iron concentrations. If mixing could bring lower layer nutrients to the euphotic zone, then we may expect enhanced production. Trends suggest that lower layer salinity has increased, which will correspond to an increase in nutrients. From this, we may expect an even greater enhancement of production if mixing were to bring these nutrients into the euphotic zone.

Sea level has increased through increased volume of the water column; overall however, over the past 40 years, GOA sea level has fallen due to continental rebound from melting glaciers. Rates of rebound are spatially and temporally dependent; uplift rate varies spatially with the change of localized glacial loads. Of the locations examined, sea level at Seward, Yakutat and, Sitka, has fallen -10 cm, -43 cm and -7 cm, respectively (Table 2).

On time scales longer than the annual cycle, sea level variation is driven by large-scale climate variations. I examined anomalies of GOA variables and climatic indices believed to be relevant to GOA (Table 3). These indices include the Pacific Decadal Oscillation (PDO), the North Pacific Gyre Oscillation (NPGO), and the El Nino Southern Oscillation index (SOI). I found no significant relationship with NPGO and GOA variables. PDO is a decadal measure of sea surface temperature and SLP in the North Pacific Ocean. It is not a dynamic mode but rather it arises from the superposition of the forcing of El Nino (ENSO), AL, and the Kuroshio-Oyashio extension, and the contribution from each of these forcing mechanisms is a function of varying timescales. El Nino is an equatorial phenomenon whose signal propagates northward, primarily

as a Kelvin along the west coast of the United States. This wave signal has baroclinic and barotropic components reflected in both the hydrography and sea level.

PDO is more strongly correlated to the GOA variables than SOI, although the response of GOA variables to both climate signals is similarly signed. Salinity and discharge anomalies have the lowest correlations (PDO: r^2~0.14; SOI: r^2~0.1), whereas temperature anomalies and GH200 are moderately correlated (PDO: r^2~0.38; SOI: r^2~0.2), and GOA sea level has the largest correlation (PDO: r^2~0.5; SOI: r^2~0.33). Surface salinity and discharge are uncorrelated to SOI. The highest correlation found is between PDO sea level at Yakutat, where r^2~66 %. For ENSO, I found the barotropic propagation velocity to be at least twice as fast as the baroclinic, where the barotropic signal takes ~2-4 months to travel from the equator to GOA, and the baroclinic takes ~7-9 months.

Future work would include similar analyses of newly available hydrography data at GAK1; this would increase statistical confidence and improve the understanding of seasonal differences in hydrography. An examination of Resurrection Bay hydrography data may also shed light on understanding the connection between the inter-annual variability of GH200 and SSL. Acquiring time series of velocity and transport data from within the ACC would be highly beneficial when analyzed in conjunction with wind, hydrography and sea level data. This could lead to simple and perhaps quasi-realtime estimates of ACC transport, which in conjunction with the GAK1 hydrographic data, would yield estimates of freshwater and heat transports within this current.

5 References

Allen, J., 1977. Short Term Spectral Analysis, Synthesis, and Modification by Discrete Fourier Transform. Acoustics, Speech, and Signal Processing. 25, 235-238.

Allen, J., Rabiner, L., 1977. A Unified Approach to Short-Time Fourier Analysis and Synthesis. Proceedings of the IEEE. 65, 1558-1564.

Arendt, A.A., Echelmeyer, K.A., Harrison, W.D., Lingle, C.S., Valentine, V. B., 2002. Rapid Wastage of Alaska Glaciers and Their Contribution to Rising Sea Level. Science. 297, 382-385.

Bendat, J.S., Piersol, A.G., 1970. Random Data: Analysis and Measurement Procedures, first ed. Wiley-Interscience, New York.

Bendat, J.S., Piersol, A.G., 1980. Engineering Applications of Correlation and Spectral Analysis, first ed. John Wiley and Sons, New York.

Bendat, J.S., Piersol, A.G., 2000. Random Data: Analysis and Measurement Procedures, third ed. Wiley-Interscience, New York.

Biltoft, C., Pardyjak, E., 2009. Spectral Coherence and the Statistical Significance of Turbulent Flux Comparisons. American Meteorological Society. 26, 403-410.

Bingham, C., Godfrey, D., Tukey, J., 1967. Modern Techniques of Power Spectrum Estimation. IEEE Transactions on Audio and Electroacoustics. 15, 56-66.

Brillinger, D., 1975. Time Series: Data Analysis and Theory. First ed. Holt Rinehart and Winston, New York.

Carmack, E.C., 2007. The Alpha/Beta Ocean Distinction: A Perspective on Freshwater Fluxes, Convection, Nutrients and Productivity in High Latitude Seas. Deep-Sea Research II. 54, 2578-2598.

Carter, C., 1987. Coherence and Time Delay Estimation. Proceedings of the IEEE. 75,236-255.

Chelton, D.B., Davis, R.E., 1982. Monthly Mean Sea Level Variability along the West Coast of North America. Journal of Physical Oceanography. 12, 757-784.

Childers, A.R., Whitledge, T.E., Stockwell, D.A., 2005. Seasonal and Interannual Variability in the distribution of Nutrients and Chlorophyll a Across the Gulf of Alaska Shelf: 1998-2000. Deep-Sea Research II. 52, 193-216.

Cooley, J., Tukey, J., 1965. An Algorithm of the Machine Calculation of Complex Fourier Series. Mathematics of Computation. 19, 297-301.

Csanady ,G.T., 1981. Shelf Circulation Cells. Philosophical Transactions of the Royal Society of London, Series A, Mathematical and Physical Sciences. 302, 515-529.

Di Lorenzo, E., Schneider, N., Cobb, K.M., Franks, P.J.S., Chhak, K., Miller, A.J., McWilliams, J.C., Bograd, S.J., Arango, H., Curchitser, E., Powell, T.M., Riviere, P., 2008. North Pacific Gyre Oscillation Links Ocean Climate and Ecosystem Change. Geophysical Research Letters. 35, L08607.

Durack, P.J., Wijffels, S.E., Matear, R.J., 2012. Ocean Salinities Reveal Strong Global Water Cycle Intensification During 1950 to 2000. Science. 336, 455-458.

Eberhart-Phillips, D., Christensen, D.H., Brocher, T.M., Hansen, R., Ruppert, N.A., Haeussler, P.J., Abers, G.A., 2006. Imaging the Transition from Aleutian Subduction to Yakutat Collision in Central Alaska, with Local Earthquakes and Active Source Date. Journal of Geophysical Research. 111, B11303.

Emery, W.J., Thompson, R.E., 2000. Data Analysis Methods in Physical Oceanography, second ed. Elsevier, Amsterdam.

Enfield, D.B, Allen, J.S., 1980. On the Structure and Dynamics of Monthly Mean Sea Level Anomalies Along the Pacific Coast of North and South America. American Meteorological Society. 10, 557-578.

Freymueller, J.T., Woodard, H., Cohen, S.C., Cross, R., Elliot, J., Larsen, C., Hreinsdottir, S., Zweck., C., 2007. Active Deformation Processes in Alaska, Based on 15 Years of GPs Measurements. In: Active Tectonics and Seismic Potential of Alaska. Eds. Freymueller, J.T., Haeussler, P.J., Wesson, R.L., Ekstrom, G. AGU

Gardner, A.S., Moholdt, G., Cogley, G.J., Wouters, B., Arendt, A.A., Wahr, J., Berthier, E., Hock, R., Pfeffer, T.W., Kaser, G., Ligtenberg, S.R.M., Bolch, T., Sharp, M.J., Hagen, J.O., Van Den Broeke, M.R., Paul, F., 2013. A Reconciled Estimate of Glacier Contributions to Sea Level Rise: 2003 to 2009. Science. 340, 852-857.

Gulick, S., Lowe, L.A., Pavis, T.L., Gardner, J.V., Mayer, L.A., 2007. Geophysical Insights into the Transition Fault Debate: Propagating Strike Slip in Response to Stalling Yakutat Block Subduction in the Gulf of Alaska. Geology. 35, 763-766.

Hamon, B.V., 1966. Continental Shelf Waves and the Effects of Atmospheric Pressure and Wind Stress on Sea Level. Journal of Geophysical Research. 71, 2883-2893.

Hannan, E.J., 1970. Multiple Time Series, first ed. John Wiley and Sons, New York.

Harris Semiconductor, 1997. A Tutorial in Coherent and Windowed Sampling with A/D Converters. Harris Data Acquisition, App-note. No. AN9675.

IPCC, 2014. Climate Change 2014: Impacts, Adaptations, and Vulnerability. Fifth Assessment Report. http://www.ipcc.ch/

Julian, P., 1975. Comments on the Determination of Significance Levels of the Coherence Statistic. Journal of the Atmospheric Sciences. 32, 836-837.

Koopmans, L.H., 1974. The Spectral Analysis of Time Series, first ed. Academic Press, New York.

Large, W.G., Pond, S., 1981. Open Ocean Momentum Flux Measurements in Moderate to Strong Winds. Journal of Physical Oceanography. 11, 324-336.

Larsen, C.F., Echelmeyer, K.A., Freymueller, J.T., Motyka, R.J., 2003. Tide Gauge Records of Uplift along the Northern Pacific-North American Plate Boundary, 1937 to 2001. Journal of Geophysical Research. 108(24), 2216.

Lisitzin, E., Pattullo, J.G., 1961. The Principal Factors Influencing the Seasonal Oscillation of Sea Level. Journal of Geophysical Research. 66, 845-852.

Livingstone, D., Royer, T.C., 1980. Observed Surface Winds at Middleton Island, Gulf of Alaska and their Influence on the Ocean Circulation. American Meteorological Society. 10, 753-764.

Macklin, S.A., Lackmann, G.M., Gray, J., 1988. Offshore-Directed Winds in the Vicinity of Prince William Sound, Alaska. Monthly Weather Review. 116, 1289-1301.

Mantua, N.J., Hare, S.R., Zhang, Y., Wallace, J.M., Francis, R.C., 1997. A Pacific Interdecadal Climate Oscillation with Impacts on Salmon Production. Bulletin of the American Meteorological Society. 78, 1069-1079.

Mantua, N., Hare, S., 2002. The Pacific Decadal Oscillation. Journal of Oceanography. 58, 35-44.

McCullough, B., 1995. A Spectral Analysis of Transactions Stock Market Data. The Financial Review. 30, 823-842.

Melsom, A., Metzger, J.E., Hurlburt, H.E., 2003. Impact of Remote Oceanic Forcing on Gulf of Alaska Sea Levels and Mesoscale Circulation. Journal of Geophysical Research. 108. C11.

Mesquita, M.D.S., Atkinson, D.E., Hodges, K.I., 2010. Characteristics and Variability of Storm Tracks in the North Pacific, Bering Sea, and Alaska. Journal of Climate. 23, 294-311.

Miller, W., Sigvardt, K., 1998. Spectral Analysis of Oscillatory Neural Circuits. Journal of Neuroscience Methods. 80, 113-128.

Neal, E.G., Hood, E., Smikrud, K., 2010. Contribution of Glacial Runoff to Freshwater Discharge into the Gulf of Alaska. Geophysical Research Letters. 37, L06404.

Nuttall, A., 1971. Spectral Estimation of Means of Overlapped FFT Processing of Windowed Data. Naval Underwater Systems Center, New London, CT, Rep. 4169, and suppl. TR4169S.

Otnes, R.K., Enochson, L., 1978. Applied Time Series Analysis Volume One, first ed., John Wiley and Sons, New York.

Panofsky, H.A., Brier, G.W., 1958. Some Applications of Statistics to Meteorology, first ed. The Pennsylvania State University, University Park.

Papineau, J., 2014. Understanding Alaska's Climate Variation. http://pafc.arh.noaa.gov/climvar/climate-paper.html

Park, J., Watts, R., 2005. Response of the Southern Japan/East Sea at Atmospheric Pressure. Deep-Sea Research II. 52, 1671-1683.

Pattullo, J., Munk, W., Revelle, R., Strong, E., 1955. The Seasonal Oscillation in Sea Level. Journal of Marine Research. 14, 88-113.

Pawlowicz, R., Beardsley, B., Lentz, S., 2002. Classical Tidal Harmonic Analysis including Error Estimates in MATLAB using T_Tide. Computers & Geosciences. 28, 929-937.

Piersol, A., 1967. Power Spectra Measurements for Spacecraft Vibration Data. Journal of Spacecraft and Rockets. 4, 1613-1617.

Pond, S., Pickard, G.L., 1983. Introductory Dynamical Oceanography. Second Ed. Pergamon Press, New York.

Priestley, M., 1981. Spectral Analysis and Time Series. first ed. Academic Press, London.

Rabinovich, A., Stephenson, F., 2004. Longwave Measurements for the Coast of British Columbia and Improvements to the Tsunami Warming Capability. Natural Hazards. 32, 313-343.

Reed, R.K., Schumacher, J.D., 1981. Sea Level Variations in Relations to Coastal Flow Around the Gulf of Alaska. Journal of Geophysical Research. 86, 6543-6546.

Reed, R.K., Schumacher, J.K., 1986. Physical Oceanography, in: The Gulf of Alaska: Physical Environmental and Biological Resources. Ed. Hood, D.W., Zimmerman, S.T., Chapter 2, 57-75. University of Washington Press, Seattle.

Reid, J.L., Mantyla, A.W., 1976. The Effect of the Geostrophic Flow Upon Coastal Sea Level Elevations in the Northern Pacific Ocean. Journal of Geophysical Research. 81, 3100-3110.

Roden, G.I., 1960. On the Nonseasonal Variations in Sea Level along the West Coast of North America. Journal of Geophysical Research. 65, 2809-2826.

Roden, G.I., 1966. Low Frequency Sea Level Oscillations Along the Pacific Coast of North America. Journal of Geophysical Research. 71, 4755-4776.

Rodionov, S.N., Bond, N.A., Overland, J.E., 2007. The Aleutian Low, Storm Tracks, and Winter Climate Variability in the Bering Sea. Deep-Sea Research II. 54, 2560-2577.

Rosenberg, J., Amjad, A., Breeze, P., Brillinger, D., Halliday, D., 1989. The Fourier Approach to the Identification of Functional Coupling Between Neuronal Spike Trains. Progress in Biophysics and Molecular Biology. 53, 1-31.

Royer, T.C., 1979. On the Effect of Precipitation and Runoff on Coastal Circulation in the Gulf of Alaska. American Meteorological Society. 9, 555-563.

Royer, T.C., 1981. Baroclinic Transport in the Gulf of Alaska, Part II. A Fresh Water Driven Coastal Current. Journal of Marine Research. 39, 251-265.

Royer, T.C., 1982. Coastal Fresh Water Discharge in the Northeast Pacific. Journal of Geophysical Research. 87, 2017-2021.

Royer, T.C., 2005. Hydrographic Responses at a Coastal Site in the Northern Gulf of Alaska to Seasonal and Interannual Forcing. Deep-Sea Research II. 52, 267-288.

Royer, T.C., Grosch, C.E., Mysak, L.A., 2001. Interdecadal variability of Northeast Pacific Coastal Freshwater and its Implications on Biological Productivity. Progress in Oceanography. 49, 95-111.

Royer, T.C., Weingartner, T., 1999. Coastal Hydrographic Responses in the Northern Gulf of Alaska to the 1997-98 ENSO Event. North Pacific Marine Science Organization-Pices. Report 10.

Ryan, H., Noble, M., 2006. Alongshore Wind Forcing of Coastal Sea Level as a Function of Frequency. Journal of Physical Oceanography. 36, 2173-2184.

Schneider, N., Cornuelle, B.D., 2005. The Forcing of the Pacific Decadal Oscillation. American Meteorological Society. 18, 4355-4373.

Schumacher, J.D., Reed, R.K., 1980. Coastal flow in the Northwest Gulf of Alaska: The Kenai Current. Journal of Geophysical Research. 85, 6680-6688.

Schuster, A., 1898. On the Investigation of Hidden Periodicities with Application to a Supposed 26 day Period of Meteorological Phenomena. Terrestrial Magnetism. 3, 13-41.

Schwing, F.B., 1989. Subtidal Response of the Scotian Shelf Bottom Pressure Field to Meteorological Forcing. Atmosphere-Ocean. 27, 157-180.

Sheaf, M.A., Serpa, L., Pavis, T., 2003. Exhumation Rates in St.Elias Mountains, Alaska. Technophysics. 367, 1-11.

Shin, K., Hammond, J., 2008. Fundamentals of Signal Processing for Sound and Vibration Engineering. first ed. John Wiley and Sons, West Sussex.

Sokolova, S.E., Rabinovich, A.B., Chu, K.S., 1992. On the Atmosphere Induced Sea Level Variations along the Western Coast of the Sea of Japan. La Mer. 30, 191-212.

Stabeno, P.J., Bond, N.A., Hermann, A.J., Kachel, N.B., Mordy, C.W., Overland, J.E., 2004. Meteorology and Oceanography of the Northern Gulf of Alaska. Continental Shelf Research. 24, 859-897.

Subbotina, M., Thomson, R., Rabinovich, A., 2001. Spectral Characteristics of Sea Level Variability Along the West Coast of North America During the 1982-83 and 1997-98 El Nino Events. Progress in Oceanography. 49, 353-372.

Thompson, R., 1979. Coherence Significance Levels. Journal of Atmospheric Sciences. 26, 2020-2021.

Townend, J., 2002. Practical Statistics for Environmental and Biological Scientists. first ed. Wiley, New York.

Trupin, A., Wahr, J., 1990. Spectroscopic Analysis of Global Tide Gauge Sea Level Data. Geophysical Journal International. 100, 441-453.

Uhlen, P., 2004. Spectral Analysis of Calcium Oscillations. Science STKE. 258, 1-12.

Von Storch, H., Zwiers, F.W., 1999. Statistical Analysis in Climate Research, first ed. Cambridge University Press, Cambridge.

Wang, J., Jin, M., Musgrave, D.L., Ikeda, M., 2004. A Hydrologic Digital Elevation Model for Freshwater Discharge into the Gulf of Alaska. Journal of Geophysical Research. 109, C07009.

Wang, S., Tang, M., 2004. Exact Confidence Intervals for Magnitude-Squared Coherence Estimates. IEEE Signal Processing Letters. 11, 326-329.

Weingartner, T.J., 2007. The Physical Environment of the Gulf of Alaska, in: Long-Term Ecological change in the Northern Gulf of Alaska. Ed. Spies, R.B., Chapter 2.2, 12-47. Elsevier, Amsterdam.

Weingartner, T.J., Danielson, S.L., Royer, T.C., 2005. Freshwater Variability and Predictability in the Alaska Coastal Current. Deep-Sea Research II. 52, 169-191.

Weingartner, T.J., Eisner, L., Eckert, G.L., Danielson, S., 2008. Southeast Alaska: Oceanographic Habitats and Linkages. Journal of Biogeography. Special Issue, 1-13.

Welch, P., 1967. The Use of Fast Fourier Transform for the Estimation of Power Spectra: A Method Based on Time Averaging over Short, Modified Periodograms. IEEE Transactions on Audio and Electroacoustics. AU-15, 70-73.

Wilson, J.G., Overland, J.E., 1986. Meteorology, in: The Gulf of Alaska: Physical Environmental and Biological Resources. Ed. Hood, D.W., Zimmerman, S.T., Chapter 2, 31-54. University of Washington Press, Seattle.

Woodgate, R.A., Aagaard, K., Weingartner, T.J., 2006. Interannual Changes in the Bering Strait fluxes of Volume, Heat and Freshwater between 1991 and 2004. Geophysical Research Letters. 33, L15609.

WRCC - Western Regional Climate Centers
http://www.wrcc.dri.edu/htmlfiles/westcomp.ovc.html

Wu, J., Aguilar-Islas, A., Rember, R., Weingartner, T., Danielson, S., Whitledge, T., 2009. Size-Fractionated Iron Distribution on the Northern Gulf of Alaska. Geophysical Research Letters. 36, L11606.

Wunsch, C., 1972. Bermuda Sea Level in Relation to Tides, Weather, and Baroclinic Fluctuations. Reviews of Geophysics and Space Physics. 10, 1-49.

Wunsch, C. 1991. Large Scale Response of the Ocean to Atmospheric Forcing at Low Frequencies. Journal of Geophysical Research. 96, 15,083-15,092.

Wyrtki, K., 1975. Fluctuations of the Dynamic Topography in the Pacific Ocean. Journal of Physical Oceanography. 5, 450-459.

Zoubir, A., 2005. On Confidence Intervals for the Coherence Function. International Conference on Acoustics, Speech, and Signal Processing. 4, 413-416.